

# Optical Characterization of Complex Mechanical and Thermal Transport Properties

by  
Jeremy A. Johnson

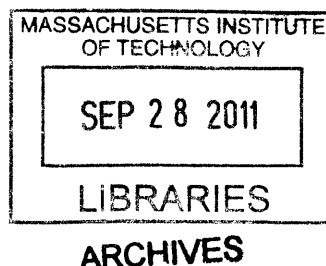
B.S. Chemistry, Brigham Young University (2006)

Submitted to the Department of Chemistry  
in partial fulfillment of the requirements for the degree of  
Doctor of Philosophy  
at the

MASSACHUSETTS INSTITUTE OF TECHNOLOGY

September 2011

© Massachusetts Institute of Technology 2011. All rights reserved.



Author.....

Department of Chemistry  
8 June, 2011

Certified by.....

Keith A. Nelson  
Thesis Supervisor, Professor of Chemistry

Accepted by.....

Robert W. Field  
Chairman, Department Committee on Graduate Students



This doctoral thesis has been examined by a committee of the  
Department of Chemistry as follows:

Professor Robert W. Field .....  
Committee Chair

Professor Keith A. Nelson .....  
Thesis Supervisor

Professor Jianshu Cao .....  
Committee Member





# **Optical Characterization of Complex Mechanical and Thermal Transport Properties**

by  
Jeremy A. Johnson

Submitted to the Department of Chemistry on 8 June, 2011,  
in partial fulfillment of the requirements for the degree of Doctor of Philosophy

## **Abstract**

Time-resolved impulsive stimulated light scattering (ISS), also known as transient grating spectroscopy, was used to investigate phonon mediated thermal transport in semiconductors and mechanical degrees of freedom linked to structural relaxation in supercooled liquids. In ISS measurements, short optical pulses are crossed to produce a periodic excitation profile in or at the surface of the sample. Light from a probe beam that diffracts off the periodic material response is monitored to observe the dynamics of interest.

A number of improvements were put into practice including the ability to separate so-called amplitude and phase grating signal contributions using heterodyne detection. This allowed the measurement of thermal transport in lead telluride and gallium arsenide-aluminum arsenide superlattices, and also provided the first direct observation of the initial crossover from diffusive to ballistic thermal transport in single crystal silicon and gallium arsenide at room temperature. Recent first-principles calculations of the thermal conductivity accumulation as a function of phonon mean free path allowed direct comparison to our measured results.

In an effort to test theoretical predictions of the prevailing first principles theory of the glass transition, the mode coupling theory (MCT), photoacoustic measurements throughout much of the MHz acoustic frequency range were conducted in supercooled liquids. Longitudinal and shear acoustic waves were generated and monitored in supercooled liquid triphenyl phosphite in order to compare the dynamics. An additional interferometric technique analogous to ISS was developed to probe longitudinal acoustic waves at lower frequencies than was typically accessible with ISS. Lower frequency acoustic data were collected in supercooled tetramethyl tetraphenyl trisiloxane in conjunction with piezo-transducer, ISS, and picosecond ultrasonics measurements to produce the first truly broadband mechanical spectra of a viscoelastic material covering frequencies continuously from mHz to hundreds of GHz. This allowed direct testing of the MCT predicted connection between fast and slow relaxation in supercooled liquids.

Measurements of the quasi-longitudinal speed of sound in the energetic material cyclotrimethylene trinitramine (RDX) were also performed with ISS and picosecond ultrasonics from 0.5 to 15 GHz in order to resolve discrepancies in published low and high frequency elastic constants.

Thesis Supervisor: Keith Adam Nelson  
Title: Professor of Chemistry

## **Acknowledgements**

My time at MIT has been impactful, formative, and an extraordinary experience that I'm certain I will remember with gratitude throughout my life. It would not have been such a singular experience were it not for the interactions with outstanding individuals to whom I must express my appreciation – typeset here as well as face to face. Keith Nelson has been all I could have hoped for in an advisor. Discussions always leave me impressed with his depth of knowledge and increase my desire to learn more. Keith has pushed me to work harder and think more deeply about the physical processes we've studied and needed words of encouragement have come at discouraging times. And important to me, he works incredibly hard, but has also been a good example that life is more than just science. Of the members of the Nelson group past and present, Darius Torchinsky and Alex Maznev have had the greatest impact on my research. As a new graduate student Darius tutored me in the ways of transient grating kung fu. Long, fun hours in the lab and great instruction recorded on countless sheets of scratch paper got me off to a promising start. Alex returned to the group at a time when fledgling efforts to study thermal transport were underway. His constant help, expertise, and wise suggestions helped the work take off and transform from a side-project into exciting novel results that comprise the bulk of this thesis.

The thermal transport studies were part of a collaborative effort funded by the DOE through the Energy Frontier Research Center (EFRC) program. Large thanks are in order for our EFRC (the Solid State Solar Thermal Energy Conversion center – S<sup>3</sup>TEC) partners, particularly Gang Chen and his students Austin Minnich, Maria Luckyanova and Kimberlee Collins. Also Mayank Bulsara and Adam Jandl in Eugene Fitzgerald's group.

Kit Werley, Johanna Wolfson, and Harold Hwang have been great friends and support back from our first year together here at MIT. I've had the privilege of working especially closely with Kara Manke and Christoph Klieber on photoacoustics work, and it's been good to also work with David Veysset and Gagan Saini. There are so many past and present members of the Nelson group, including Dylan Arias, Patrick Wen, Kathy Stone, Duffy Turner, Cassie Newell, Ka-Lo Yeh, Taeho Shin, Matthias Hoffman, Nate Brandt, Brad Perkins, Sharly Fliescher, Xibin Zhou, Zhao Chen, Vasily Temnov, and Stephanie Teo, as well as the new group of students Colby Steiner, Sam Teitelbaum, Yongbao Sun, and especially Jeff Eliason who will be continuing the transient grating work in the near future. I've also had the

wonderful opportunity to work in the Lambda Lab outreach lab with the late Gift Jaja. Cassie Newell and I got to work closely with Gift for a summer and later when students came in to the lab. I'll always remember Gift's positive personality and desire to help students learn, and consider it a blessing to have known her.

My thesis committee chair Bob Field and committee member Jianshu Cao have been remarkably supportive and helpful. Informal conversations with Bob are always pleasant and our annual meetings always left me feeling more motivated and happy for the opportunity to be in school here. Jianshu was a great teacher of statistical mechanics and has often been available for insightful discussions of light scattering and structural relaxation dynamics.

I also need to thank my family and friends outside of the MIT community. My cousins Cameron and Whitney Wheeler provided entertaining diversions and emotional support especially my first year in Boston and ever since. My parents Doris and Severin Johnson are amazing people that I love dearly. Words can't express the blessing and rock solid support they have been all my life. My siblings Janiece, Jessica, Jared, and Jackie are some of my best friends in the world. The family truly can be the greatest institution on earth. I also need to thank friends from the Arlington Congregation of the Church of Jesus Christ of Latter-day Saints. Their friendship, support, shared faith, and the teachings and opportunities to serve rejuvenate and inspire each week. For me, no list would be complete without thanking God, my Heavenly Father for His countless blessings and matchless gifts in my life, especially His Son Jesus Christ.

Finally, my greatest love and support is my wife Rochelle. If everyone could have a spouse like her during graduate school, so many more students would be happier and more productive. Rochelle is the greatest motivator to work hard and take advantage of time in the lab, while maintaining a healthy balance in life. I love that I can share my successes and failures with her in a way not possible with anyone else. And the opportunity to love, have fun with, and serve her is a wellspring of happiness.



*to my remarkable wife Rochelle*

## Table of Contents

Abstract	5
Acknowledgements	6
<b>1 Overview</b>	<b>13</b>
<b>2 Spectroscopic techniques to determine mechanical and thermal transport properties</b>	<b>17</b>
2.1 Crossing beams	18
2.2 The excitation process	19
2.2.a Impulsive stimulated thermal scattering	19
2.2.b Impulsive stimulated Brillouin scattering	20
2.3 The probing process	22
2.4 Heterodyne detection	24
2.5 The experimental setup	27
2.6 ISS wavevector range	29
2.7 Additional approaches for short grating periods	30
2.7.a Reflective setup	30
2.7.b Immersion imaging	31
2.8 Single beam excitation	32
2.9 Point source/point probe – interferometric detection	34
2.10 Summary	36
<b>3 Phonon mediated thermal transport</b>	<b>39</b>
3.1 Phonon dispersion	40
3.2 Phonon heat capacity	42
3.3 Phonon mean free paths	43
3.4 Diffusion equation	48
3.5 Manipulating thermal transport	49
3.5.a Interfaces	50
3.5.b Superlattices	51
3.6 Summary and experimental techniques	53
<b>4 Transient thermal grating measurements in the reflection geometry</b>	<b>57</b>
4.1 Introduction	57
4.2 Amplitude vs. phase grating signal	58
4.3 TG experiments on a PbTe thin film	60
4.4 Analysis of the thermal transport	66
4.5 Thermal diffusivity measurement of PbTe film	68
4.6 Modeling the phase grating signal	69
4.7 In- vs. Cross-plane thermal diffusivity of GaAs/AlAs superlattices	71
4.7.a SL samples	71
4.7.b TG In-plane and TTR Cross-plane measurements	72
4.7.c SL thermal transport results and discussion	74

4.8 TG Discussion and outlook	77
<b>5 From diffusive to ballistic thermal transport</b>	<b>81</b>
5.1 Introduction	81
5.2 Si membrane fabrication	82
5.3 Experiments on Si membranes	85
5.4 Transient thermal grating decay in the non-diffusive regime	88
5.5 Si membrane comparison to theory	91
5.6 Experiments on bulk GaAs	93
5.7 GaAs comparison to theory	95
5.8 Conclusions and discussion	96
<b>6 Supercooled Liquids</b>	<b>99</b>
6.1 Phenomenology of Supercooling	101
6.2 Mode Coupling Theory of the glass transition	108
6.2.a Introduction	108
6.2.b Mode Coupling Theory Equations	108
6.2.c Predictions of the Mode Coupling Theory	111
6.2.d The susceptibility spectrum	114
<b>7 Longitudinal &amp; shear acoustic waves in supercooled liquids using ISS</b>	<b>117</b>
7.1 ISS equations of motion	118
7.2 Longitudinal acoustic waves	119
7.3 Shear acoustic waves	122
7.4 Experimental study of triphenyl phosphite	125
7.5 TPP results and discussion	127
7.6 Summary	134
<b>8 Broadband longitudinal acoustic spectroscopy of DC704</b>	<b>137</b>
8.1 Nanosecond acoustic interferometry of DC704	138
8.2 Broadband spectra of DC704	142
8.3 Tests of MCT predictions	146
8.4 Conclusions	148
<b>9 Higher frequency speed of sound in RDX</b>	<b>151</b>
9.1 Background	151
9.2 Experimental Methods	153
9.2.a Sample preparation	153
9.2.b ISS technique	154
9.2.c PAI technique	155
9.3 Results and discussion	157
9.4 Conclusions	159
<b>Bibliography</b>	<b>163</b>

*I have always been fascinated with light. In the home I grew up in, the living room had large, bright windows from floor to ceiling. There was a desk near the window with a glass surface over the wood. I remember being enthralled with that glass. Looking straight at the glass you could clearly see the wood beneath it. But bringing my face close to the glass, reflections of what was outside those big windows would begin to appear on the surface until it became just like a mirror. I was also intrigued that looking directly through the glass, it was always clearly transparent, but looking in through the sides, the glass was a translucent pale green. As my knowledge has increased through the years and I can attach physical concepts to these observations, I see more clearly the remarkable behavior of light and continue to be intrigued by it. ... It would also be immensely interesting to utilize ultra-fast spectroscopy in the study of structural changes in condensed phase matter with Keith A. Nelson*

*Jeremy Johnson, 15 Dec 2005  
Statement of Objectives in Applying to MIT*



# Chapter 1

## Overview

Spectroscopy is simply the study of the interactions of light and matter. As our mere existence is certainly tied to the light that emanates from the sun, mankind, at least to a certain extent, has likely pondered such interactions from the earliest times. It was ponderings and investigations by Newton and a host of others that led to deeper understanding of many foundational principles of the modern physical sciences. When one stops to reflect, it truly is astounding the multitude of systems that can be investigated and the myriad of physical processes that can be observed using electromagnetic radiation.

It has long since been established that light can excite and probe acoustic modes and thermal responses in the bulk or at the surfaces of samples. In fact the very first stimulated Brillouin scattering photoacoustic experiments carried out by C. H. Townes with a “giant-pulse ruby maser” were performed in the Spectroscopy Laboratory at MIT [Chiao], the very lab where the photothermal and photoacoustic experiments contained in this thesis were conducted. With the advent and advancement of pulsed light sources, the ability to observe dynamics at short time scales has become increasingly practical. Single spot, short-pulsed pump-probe measurements were and still are important in research and offer a wealth of information. But studies of the wave-nature of light long ago presented potential advantages in spatial shaping due to constructive and destructive interference, which really gave birth to the fields of optical holography [Collier] and four-wave-mixing [Bloembergen] in which optical beams are combined in distinct temporal and spatial patterns. Impulsive stimulated light scattering (ISS), also commonly known as transient grating spectroscopy (TG), is a simplification of four-wave mixing methods, where two time-coincident, coherent pump pulses are crossed to form a spatially periodic excitation pattern. A probe beam diffracts off the periodic material response and the time-dependent signal is monitored. Modeling of the

material response is facilitated due to the well-defined wavevector of the periodic excitation. Many systems and transient grating responses may be studied, including population density gratings, space charge gratings, concentration gratings, and the main focuses of this work: thermal gratings and density/stress/strain/acoustic wave gratings [Eichler,Fourkas].

In this thesis, I will discuss many of the ISS studies of thermal transport and mechanical material properties that I have performed during my graduate studies. Due to the collaborative nature of all the projects I've been involved with and the many people I appreciate for helping to make this research possible, I will use the plural 'we' in writing this thesis.

Chapter 2 provides an introduction to impulsive stimulated light scattering. Focused on photoacoustic and photothermal measurements, the relevant methodology will be developed. The experimental setup as situated in the G. R. Harrison Spectroscopy Lab will be described. Additionally, a few variations on the ISS theme will be presented. After the general experimental overview, this thesis is divided into two major parts, reflecting the two major projects that my graduate studies consisted of, namely the study of fundamental properties of thermal transport in semiconductors and the nature of structural relaxation in supercooled liquids. Chapters 3-5 cover thermal transport and Chapters 6-8 cover work involving supercooled liquids.

In Chapter 3, we give a brief overview of important factors governing thermal transport in semiconductors and dielectric crystals, as well as a short description of efforts to design materials with modified thermal transport properties. In Chapter 4 we present the methodology in detail for reflective transient grating measurements of thermal transport, and illustrate the technique by determining the in-plane thermal diffusivity of a PbTe thin film, thus showcasing the ability to measure, in a non-contact, non-destructive way, thermal transport properties of a surface layer. In an effort to understand the effects of multiple interfaces on thermal transport, we further utilize the technique to measure the in-plane thermal transport in two

GaAs/AlAs superlattices and compare the results with optical transient thermorefectance measurements of the cross-plane thermal transport in these one-dimensional structures. Chapter 5 shifts to efforts aimed at deepening our understanding of intrinsic properties in bulk materials that influence thermal transport, namely the mean free paths of phonons that carry heat. When considering whether transport is in the diffusive or ballistic regime, two key length scales are the energy carrier mean free path and the distance over which transport is measured. We show direct evidence of the initial crossover from diffusive to ballistic thermal transport in the common semiconductors silicon and gallium arsenide at room temperature and at measurement length scales much longer than previously thought possible. These experimental results are compared with first-principles calculations and we discuss the important information that can be provided in order to aid in the design of novel materials with custom thermal transport properties.

In Chapter 6, we introduce relevant phenomenology and theory related the nature of structural relaxation in supercooled liquids. In Chapter 7 we derive appropriate equations of motion for ISS measurements of viscous materials including the propagation of longitudinal and shear acoustic waves, and present a comparison between longitudinal and shear relaxation. Chapter 8 focuses on the analysis of a broadband acoustic spectrum, acquired at many temperatures and compiled with data collected using a number of experimental techniques, each with its own limited frequency range.

Finally in Chapter 9, we diverge from the two main thesis themes to present ISS photoacoustic measurements of the energetic crystal RDX. Discrepancies in reported elastic constants determined using techniques with varied frequency ranges led some to posit a relaxation-induced frequency dependent speed of sound. We report measurements performed using ISS and picosecond acoustic interferometry of the speed of sound in RDX, from which the elastic constants are determined, at acoustic frequencies covering the range of the disagreeing techniques.



# Chapter 2

## Spectroscopic techniques to determine mechanical and thermal transport properties

The theory of impulsive stimulated light scattering can be defined in the framework of four-wave mixing and non-linear optics, but many processes that one would naturally describe with such an approach are on much faster timescales than experiments presented in this thesis, so adequate classical mechanics and phenomenological descriptions will be used predominately to describe excitation and probing processes. ISS measurements have been conducted on many types of samples [Eichler] in transmission and reflection geometries. A typical transmission setup is shown in Fig. 2.1. The relevant methodology for various cases, focused on photoacoustic and photothermal measurements, is developed below. We will use the term impulsive stimulated light scattering (ISS) generally, but to add more specificity, we will use transient grating spectroscopy (TG) to describe photothermal measurements. We begin with a description of excitation induced with crossed laser beams, followed by the probing process and heterodyne detection.

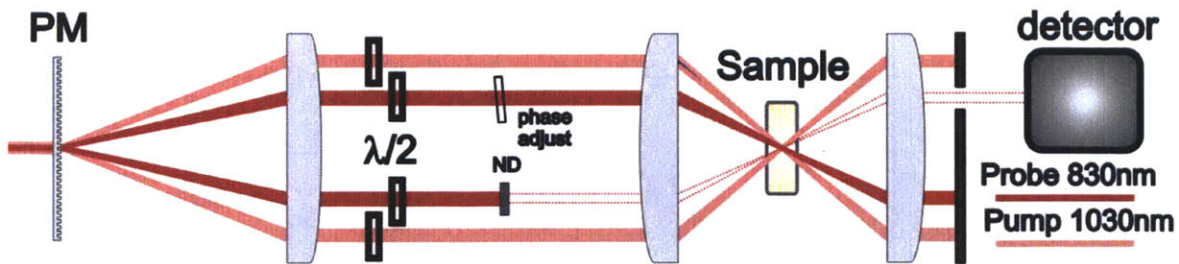


Fig. 2.1. Schematic illustration of ISS transmission-mode setup. A diffractive optic, a binary phase-mask (PM), splits pump and probe into  $\pm 1$  diffraction orders. Pump beams are focused and crossed at the sample surface by a set of lenses, generating the transient grating. Diffracted probe light is combined with an attenuated reference beam (ND) and directed to a fast detector. The relative phase difference between probe and reference beams is controlled by adjusting the angle of a glass slide (Phase Adjust) in the probe beam path. Half-wave plates allow independent polarization control of each beam.

## 2.1. Crossing beams

Constructive and destructive interference between crossed plane waves, having the same polarization and wavelength, leads to a periodic intensity profile. This interference fringe pattern can be visualized by crossing two optical beams, in this case cylindrically focused, on the surface of a CCD as depicted in Fig. 2.2(a).

In an ISS experiment, two short pump pulses are crossed in or at the surface of a sample of interest. Resonant absorption or non-resonant light-matter interactions will lead to a periodic sample response, the “transient grating” [Nelson, Yan, Eichler, Fourkas]. The transient grating period is given by

$$L = \frac{2\pi}{q} = \frac{\lambda_{air}}{2n_{sample} \sin \frac{\theta_{sample}}{2}} = \frac{\lambda_{air}}{2 \sin \frac{\theta_{air}}{2}}, \quad (2.1)$$

where  $\lambda$  is the laser wavelength,  $n$  is the refractive index,  $\theta$  is beam crossing angle, and  $q$  is the grating wavevector magnitude.

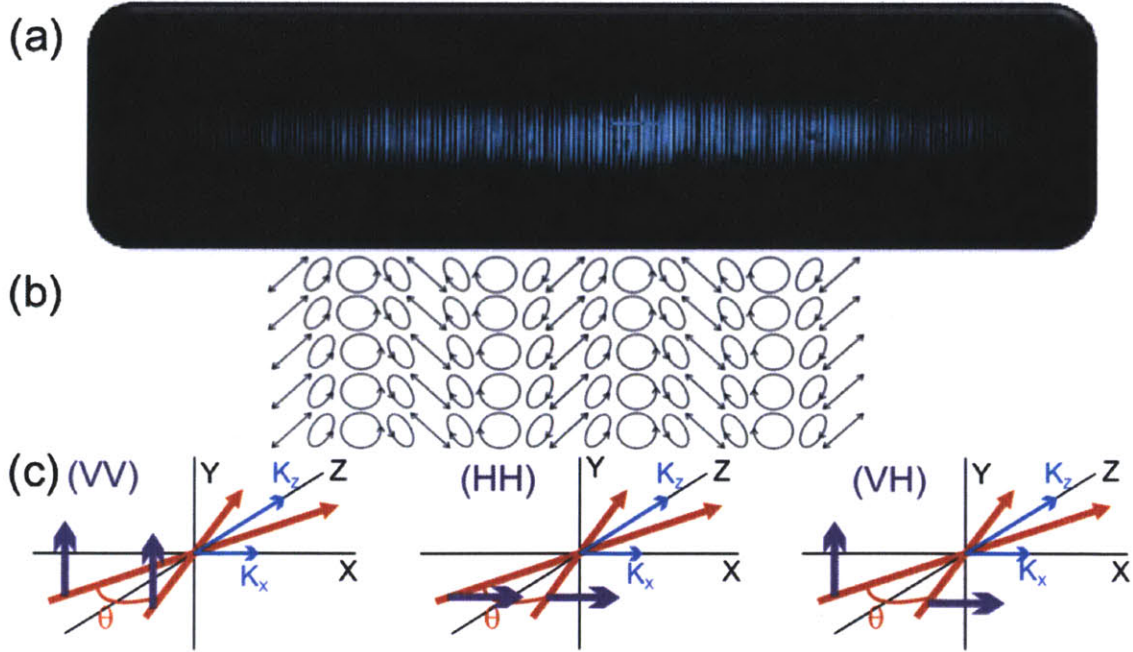


Fig. 2.2 (a) Optical interference pattern formed by crossing two cylindrically focused laser beams with parallel polarizations (VV or HH) on a CCD. (b) Periodic optical polarization pattern formed by crossing beams with crossed (VH) polarizations. (c) Diagram illustrating different beam polarizations.

In a typical transmission-mode ISS experiment, both laser beams enter the sample through a common face and the interference fringe period is identical to the case where the beams cross in air, regardless of the material refractive index. This follows because the change in angle between the incoming beams after refraction in the sample exactly compensates for the change in optical wavelength due to the refractive index. Crossing pump beams with vertical (indicated VV) or horizontal (HH) polarizations (see Fig. 2.2(c)) will lead to a periodic intensity profile depicted in Fig. 2.2(a). Using crossed polarized beams (VH or HV) will result in a uniform intensity profile, but a periodic polarization pattern with alternating regions of linear, elliptical, and circular polarizations as depicted in Fig. 2.2(b).

## 2.2. The excitation process

### 2.2.a. Impulsive stimulated thermal scattering

In a transmission measurement, the simplest case of ISS excitation occurs when VV or HH pump light is simply absorbed by an isotropic sample. Periodic heating and fast thermal expansion result in a transient thermal grating and a step-function-like stress, which launches counter-propagating coherent acoustic waves with wavelength  $L$  given by Eq. (2.1). The temperature rise,  $\delta T$ , is related to the absorbed energy, proportional to the light intensity,  $I$ , as

$$\delta T(x) \propto I(x) = I_0 \cos^2\left(\frac{q}{2}x\right) = I_0(1 + \cos(qx)) . \quad (2.2)$$

The periodic spatial profile of the thermally induced stress,  $\sigma_T$ , is illustrated in Fig. 2.3(a) and given, using Einstein notation subscripts [Nye, Landau], as

$$\sigma_{ijT}(x) = c_{ijkl}\alpha_{kl}\delta T \propto c_{ijkl}\alpha_{kl}\cos(qx), \quad (2.3)$$

where  $\alpha_{kl}$  is the thermal expansion tensor,  $c_{ijkl}$  is the elastic stiffness tensor, and  $q$  is the grating wavevector defined in Eq. 2.1. In an isotropic material,  $\alpha_{kl}$  becomes the scalar thermal expansion coefficient and  $c_{ijkl}$  is the bulk elastic modulus. In addition to the acoustic response, a periodic thermal profile will persist until heat diffuses from grating peaks to nulls. Strain and thermally induced changes in the refractive index will lead to time-dependent diffraction of a probe beam; the probing process



of the acoustic and thermal material response will be described in more detail in section 2.3 below. This pump-probe process is termed impulsive stimulated thermal scattering (ISTS) [Rogers94,Yang].

In a strongly absorbing material, as is typically the case in reflection geometry measurements, light will only be absorbed close to the sample surface. Heating and thermal expansion will therefore result in surface displacement and the coherent generation of counter-propagating surface acoustic waves (SAWs) [Rogers00]. Now the thermal transport dynamics will be governed by diffusion parallel to the surface between grating peaks and nulls as well as perpendicular to the surface into the depth of the material [Käding]. The temperature and displacement dynamics in the case of surface heating will be described in more detail in Chapter 4.

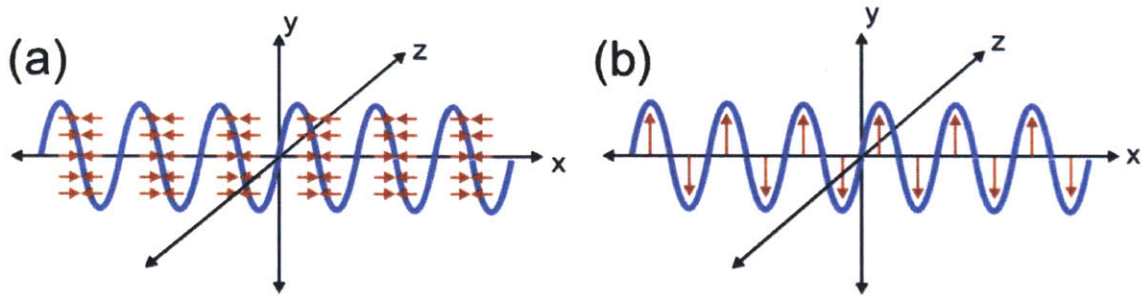


Fig. 2.3. Laser induced stress profiles in isotropic materials for (a) VV and HH polarizations via ISTS or ISBS mechanisms and (b) VH polarization via ISBS.

### 2.2.b. Impulsive stimulated Brillouin scattering

Even in the case of no optical absorption, there will still be an impulsive laser-induced stress due to electrostriction, with the pump-probe process designated impulsive stimulated Brillouin scattering (ISBS) [Nelson,Yan]. The time-averaged electric field of the pump pulses non-resonantly distorts the electron cloud of the sample, which induces nuclear motion toward new strained positions. The stress lasts only as long as the pump pulse duration, and the spatial distribution is given by

$$\sigma_{ijE}(x) = \gamma_{ijkl} E_k E_l^* . \quad (2.4)$$

The material-dependent constants  $\gamma_{ijkl}$  are directly related to the photoelastic constants [Nye] and  $E_i$  are the optical electric fields. In contrast to the step-function like time-dependence of the ISTS stress, the ISBS stress for temporally short pump



pulses is best described by a delta function in time,  $\delta(t)$ . The delta function is the time-derivative of a step-function, which in the solutions to the equations of motion (see Chapter 7), yields a linear frequency dependence in the elastic response amplitude and the ISBS signal intensity; for a given speed of sound, the ISBS acoustic signal will therefore scale with transient grating wavevector  $q$ . Using parallel (VV or HH) or crossed (VH) polarization will lead respectively to an impulsive periodic compressional or shear stress (as depicted in Fig. 2.3) able to excite longitudinal or transverse acoustic waves, the latter when the material can support shear wave propagation. When inspecting Newton's equations for a given system, the driving force is related to the gradient of the applied stress. The electrostrictive driving forces resulting from various pump beam polarizations are listed in Eq. 2.5

$$\begin{aligned}
(VV) \quad F_x &\propto E_0^2 q \gamma_{1122} \sin(qx) \delta(t) \\
(HH) \quad F_x &\propto E_0^2 q \left( \gamma_{1111} \cos^2 \frac{\theta}{2} + \gamma_{1122} \sin^2 \frac{\theta}{2} \right) \sin(qx) \delta(t) \\
(VH) \quad F_x &\propto E_0^2 q (\gamma_{1111} - \gamma_{1122}) \cos \frac{\theta}{2} \sin(qx) \delta(t)
\end{aligned} \tag{2.5}$$

In a mechanically isotropic material, ISBS can drive both longitudinal and transverse acoustic waves, whereas ISTS can only drive longitudinal acoustic waves. But ISTS has the advantage of heating the sample leading also to a thermal grating, which can be analyzed to investigate thermal transport properties. Equations of motion describing these material responses are described in more detail in subsequent chapters.

A useful comparison between the step-function ISTS force and delta-function ISBS force can be derived from the equation of motion for a simple damped harmonic oscillator (see [Marion]). In the case of under-damping, as long as a driving force is applied faster than  $\sim 1/4$  period, damped oscillations will result, but the initial phase of the oscillations will depend on the nature of the driving force. Fig. 2.4 shows calculated responses for a damped harmonic oscillator given a step, impulse, and combined driving force. Due to oscillation about a new equilibrium position, the step response is phase lagged behind the impulse response. In ISS, the angular frequency,  $\omega$ , of the generated acoustic oscillations is given by the material speed of

sound,  $v$ , and excited wavevector,  $q$ , as  $\omega = vq$ . In general, the driving force will be a combination of ISTS and ISBS, so the initial phase of acoustic oscillations will depend on the relative contribution of each excitation mechanism.

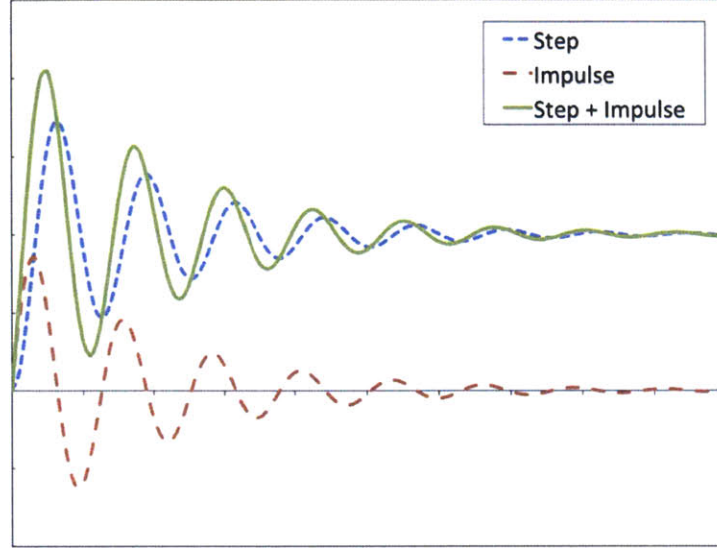


Fig. 2.4 Response of a classical damped harmonic oscillator to step function (blue short dashed line) and impulse function (red dashed line). The solid green line is a combination step + impulse response. The dependence of the phase of the oscillations on the driving force is evident in the plot.

### 2.3. The probing process

The excitation processes and resulting material responses described above lead to time-dependent, spatially periodic changes in the optical properties of the material that can be monitored with a probe beam [Berne]. ISBS- and ISTS-excited acoustic waves as well as ISTS heating and thermal expansion lead to changes in strain and temperature that can couple to the index of refraction [Eichler]. In the linear regime, deviations from the equilibrium real and imaginary refractive index,  $n^* = n + ik$ , can be written as

$$\begin{aligned}\delta n &= \frac{\partial n}{\partial \varepsilon} d\varepsilon + \frac{\partial n}{\partial T} dT \\ \delta k &= \frac{\partial k}{\partial \varepsilon} d\varepsilon + \frac{\partial k}{\partial T} dT\end{aligned}\quad (2.6)$$

where  $\varepsilon$  is the strain and  $T$  is the temperature. Time-dependent spatially periodic variations in  $n$  and  $k$  will lead respectively to phase and amplitude transient

diffraction gratings; the dynamics of the induced transient grating will be encoded in probe light diffracted and directed to a detector as illustrated in Fig. 2.5.a.

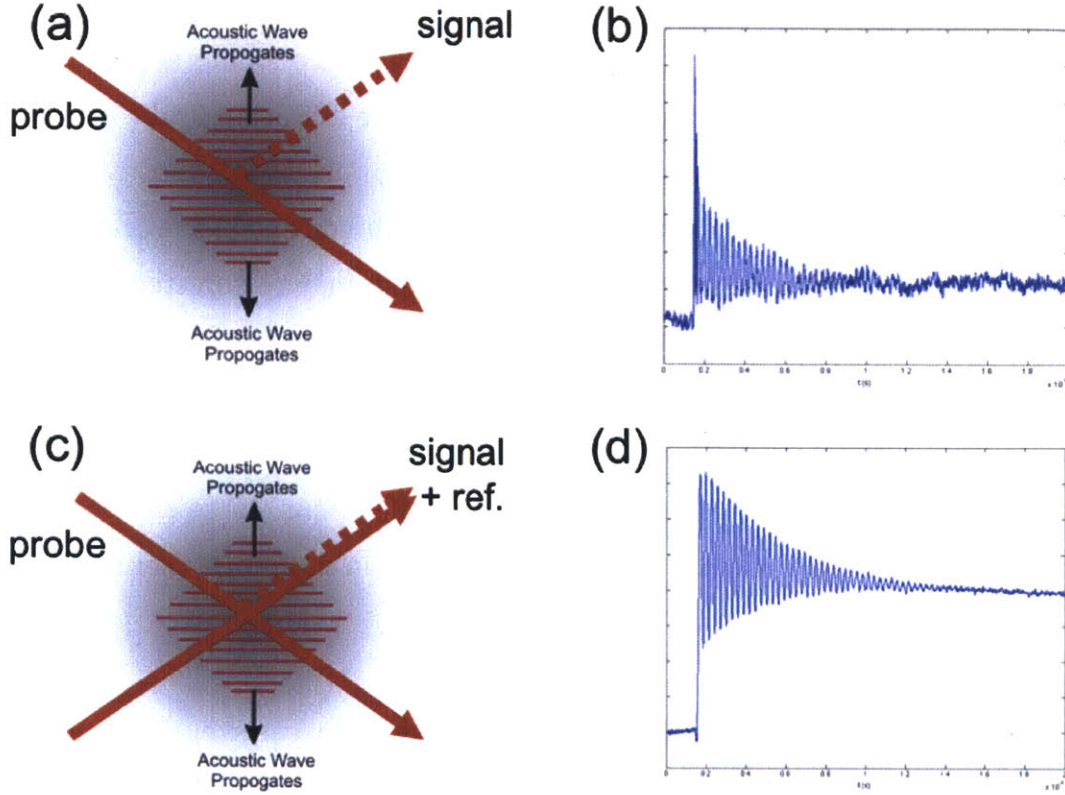


Fig. 2.5. (a) Diagram illustrating diffraction of probe beam from transient grating (here illustrated as counter-propagating acoustic waves). (b) Time-dependent diffracted signal recorded on the oscilloscope according geometry in (a). (c) The heterodyne geometry entails overlapping the diffracted signal with a reference beam. (d) Adjusting the heterodyne phase allows for increased signal levels and removal of parasitic noise sources as shown here (in comparison to (b)) and described in the text.

In practice either a variably delayed pulse or a continuous wave (CW) beam can be used as probe. All of the ISS experiments presented in this thesis utilized CW probing and fast detection electronics, with the electronic bandwidth determining the time resolution of the experiment. The diffracted probe light is directed to a detector and the time-dependent trace is recorded on the oscilloscope as shown in Fig. 2.5.b. As is the case when any waveform is modulated in time, that modulation will result in a shift or creation of side-bands in the frequency spectrum of the original waveform. For example, in ISS the optical-frequency probe beam is modulated by diffraction from excited acoustic waves, which leads to an optical

frequency shift of the diffracted probe light equal to the acoustic frequency. This frequency shift can be resolved spectrally given a spectrometer with adequate resolution [Maznev96] and is also the basis for Brillouin light scattering (BLS) measurements, but in BLS light is scattered and frequency shifted by thermal acoustic phonons [Vacher], rather than coherently generated phonons as in ISS. One immediate downside to the approach of detecting the diffracted probe light directly in the time (or frequency) domain is that only variations in intensity (or frequency) are detected, and a phase shift between amplitude and phase grating signal contributions is lost. Additionally, spurious signals may be detected and are difficult to remove through any type of data processing or experimental manipulation. In Fig. 2.5.b we observe the ISTS excited acoustic oscillations in liquid isopropanol, but these may be obscured by the sharp spike at  $t=0$  due to scattered pump light reaching the detector as well as slower modulations due to electronic noise from a high-voltage switch driving the Pockels cell in the pump laser system.

## 2.4. Heterodyne detection

To allow for separation of amplitude and phase grating signal contributions, as well as to facilitate cancelation of noise sources, we employ phase-controlled heterodyne detection [Maznev98]. In heterodyne detection as depicted in Fig. 2.5.c with accompanying signal trace in Fig. 2.5.d (also from isopropanol with identical grating period to that used in 2.5.b), the diffracted probe beam is superposed with a reference beam and directed to a detector. The relative phase difference between probe and reference beams is well defined and easily adjusted by rotating a thin glass plate in the path of either probe or reference beam before the sample (see Fig. 2.1).

As an example of heterodyne detection, let us consider the details of the signal formation in a transmission ISS measurement. In an experiment as depicted in Fig. 2.1, a probe beam with wavelength  $\lambda_p$  is incident at the sample on the transient grating. The diffracted light is spatially overlapped with an attenuated reference beam (derived from the same probe source as depicted in Fig. 2.1) and directed to a

detector where the time-dependent intensity is measured. Optical fields associated with the probe and reference beams incident on the sample are approximated as plane waves respectively as

$$E_p = E_{0p} \exp\left(i\left(k_p^2 - q^2/4\right)^{1/2} z - i(q/2)x - i\omega_p t + i\phi_p\right) \quad (2.7)$$

and

$$E_R = t_r E_{0p} \exp\left(i\left(k_p^2 - q^2/4\right)^{1/2} z + i(q/2)x - i\omega_p t + i\phi_R\right) \quad (2.8)$$

where  $E_{0p}$  is the incident probe amplitude,  $k_p$  is the optical wavevector,  $q$  is the transient grating wavevector defined above,  $\omega_p$  is the optical frequency,  $\phi_p$  and  $\phi_R$  are the phases of probe and reference beams respectively, and  $t_r$  is the attenuation factor for the reference beam. For a thin, time-dependent grating, and assuming the grating is a small perturbation, the complex transfer function is given by

$$t^*(t) \propto 1 + \cos(qx) [\delta k(t) + i\delta n(t)] , \quad (2.9)$$

where  $\delta n$  and  $\delta k$  are deviations from the equilibrium refractive index as described in Eq. 2.6. The first term in square brackets represents amplitude modulation of the incident field while the second term represents phase modulation. The diffracted field can be obtained by multiplying the input field by the complex transfer function [Collier]. Assuming the sample is located at  $z = 0$ , for the +1 diffraction order of the probe beam one obtains

$$E_{p(+1)} = E_{0p} [\delta k(t) + i\delta n(t)] \exp\left(i\left(k_p^2 - q^2/4\right)^{1/2} z + i(q/2)x - i\omega_p t + i\phi_p\right) \quad (2.10)$$

and for the zero order reference beam

$$E_{R(0)} = t_r E_{0p} \exp\left(i\left(k_p^2 - q^2/4\right)^{1/2} z + i(q/2)x - i\omega_p t + i\phi_R\right) \quad (2.11)$$

We have neglected attenuation due to absorption, but this can easily be included.

The two beams are collinear and their interference gives an intensity

$$I_s = I_{0p} \left[ t_r^2 + \delta k^2(t) + \delta n^2(t) + 2t_r (\delta k(t) \cos \phi - \delta n(t) \sin \phi) \right] , \quad (2.12)$$

where  $I_{0p}$  is the intensity of the probe beam and  $\phi = \phi_p - \phi_R$  is the heterodyne phase.

In the absence of the reference beam, the non-heterodyned diffraction signal is

given by

$$I_{non-het} = I_{0p} [\delta k^2(t) + \delta n^2(t)] \quad (2.13)$$

Thus without heterodyning the signal is comprised of a mixture of real and imaginary refractive index terms. Since the relative magnitudes and time-dependences of these terms are often unknown beforehand, unambiguous quantitative analysis of this signal could be difficult. If the reference beam intensity is much greater than that of the diffracted probe ( $t_r \gg \delta k, \delta n$ ), then the time-dependent signal is dominated by the heterodyne term

$$I_{het} = 2t_0 I_{0p} [\delta k(t) \cos \phi - \delta n(t) \sin \phi]. \quad (2.14)$$

As is evident in Eq. 2.14, the heterodyne signal is proportional to the probe intensity and reference attenuation. Typically we would increase the probe intensity as high as possible while avoiding over-heating and sample damage, and the reference beam would be attenuated to optimum detector levels, mainly to avoid saturation. The phase and amplitude grating probing processes can be thought of as the inverse of the ISBS and ISTS excitation processes. Therefore one will only be sensitive to the amplitude grating signal contribution when the probe beam is partially absorbed by the sample. If the time-dependences of  $\delta n$  and  $\delta k$  are different, the temporal shape of the signal will depend on  $\phi$ . By changing  $\phi$ , one can select the signal purely due to an amplitude grating at  $\phi = 0, \pm\pi$  following the dynamics of  $\delta k(t)$  and at  $\phi = \pm\pi/2$  purely due to a phase grating following  $\delta n(t)$ . Amplitude and phase grating data are often collected at two heterodyne phase settings allowing for cancellation of signals, like the Pockels cell interference, that are not sensitive to the heterodyne phase. A similar methodology can be used to derive the signal in a reflection ISS experiment, but in such a case, surface displacement additionally contributes to the signal (see Chapter 4).

## 2.5. The experimental setup

In the experiments described in this thesis, a short-pulsed excitation laser beam was derived from an amplified Yb:KGW laser system (HighQ femtoRegen, usually set to 1

kHz repetition-rate) lasing at 1030 nm. Although the laser output pulse duration is as short as 300 fs, electronically changing the position of an internal compressor mirror can stretch the pulse to  $\sim 1$  ps. In most experiments, to avoid sample damage or unwanted non-linear optical effects from high peak powers, we have completely bypassed the compressor to obtain  $\sim 60$  ps pulses. For details on the operation and potential trouble-shooting of the HighQ laser, please see Appendix A in [Torchnisky]. When shorter pump wavelengths were desirable, we have utilized an external, temperature-tuned BBO crystal for second harmonic generation to produce 515 nm pulses. The BBO crystal was optimally cut for 1064 nm, not 1030 nm, so the temperature was tuned quite high (240 C) for efficient second harmonic generation. In the ISS experiments the pump beam was split with a custom diffractive optic (a binary phase mask pattern) into two beams, which passed through a two-lens telescope, typically with 2:1 imaging, and were focused and crossed with external angle  $\theta$  in the sample or at the sample surface. The continuous probe beam followed an almost identical optical path as depicted in Fig. 2.1. To avoid undesirable effects due to chromatic aberrations in the imaging optics, experiments were typically conducted with pump and probe wavelengths matched with optimized optics for these wavelengths for transmission and reflection geometries. When using the 1030 nm fundamental pump laser wavelength, a Sanyo DL8032-001 150 mW at 830 nm or DL-8141-002 200 mW at 808 nm laser diode was used as the probe laser together with Thorlabs NIR achromatic doublets. The 515 nm second harmonic pump was used with Thorlabs visible achromatic doublets and probing with the output of a Coherent Verdi V5 single-longitudinal-mode, intracavity frequency-doubled Nd:YAG laser at 532 nm. Mainly in order to reduce sample heating, an electrooptic modulator (EOM – ConOptics 350-50 with 302RM high voltage source) was used in conjunction with a delay generator to chop the Verdi probe beam. Depending on the sensitivity and bandwidth needs, the probe beam was directed to either a very sensitive Hamamatsu C5658 Si APD with 1 GHz bandwidth or a New Focus 1591 high speed InGaAs photoreceiver with 4.5 GHz bandwidth. The signal traces were recorded on a Tektronix TDS 7404 oscilloscope



with 4 GHz bandwidth. For ISS measurements, Thorlabs absorptive ND filters were used to attenuate the reference beam, typically ND 3 for the Hamamatsu detector and ND 2 for the New Focus Detector. For phase control we found that the glass slides originally used had very poor parallelism and thus could introduce phase distortions that would reduce signal quality. We have found that highly parallel CVI SQW1-1512-UV fused silica plates work well, and heterodyne phase selection automation is possible with the use of a Thorlabs Z612 motorized actuator with TDC001 Servo controller. For temperature control, we have used a Janis ST-100H cryostat controlled by a Lakeshore 331 temperature controller. Data acquisition and control of heterodyne phase and temperature were facilitated using Labview on the computer. The laser table was set up as shown schematically in Fig. 2.6.

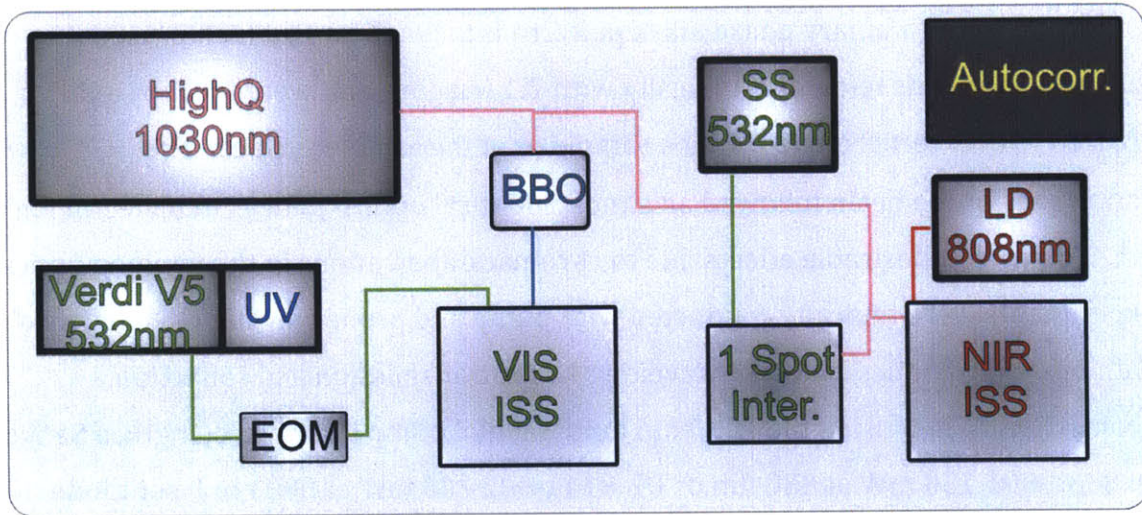


Fig. 2.6. Schematic illustration of laser table and the location of various experimental setups. The pump laser is labeled HighQ, the temperature controlled doubling crystal BBO, the green probe with UV output capabilities is the Verdi V5, the ~800 nm laser diode probe source is LD, and the electrooptic modulator is EOM. The ISS setups are labeled VIS ISS and NIR ISS. And a solid state laser with green (532 nm) output (SS) is used for the single pump spot nanosecond acoustic interferometry technique described in section 2.9. The pump pulse duration can be determined with the autocorrelator (Autocorr.).

## 2.6 ISS wavevector range

In ISS, the largest wavevector, and therefore smallest transient grating period, that can be generated or probed is for  $\theta = 180^\circ$  (grazing incidence), giving  $L = \lambda/2n$ . But this geometry can be very difficult in practice; relative phase stability between the



pump pair and probe & reference pair is needed, otherwise heterodyne detection becomes significantly less efficient due to heterodyne phase fluctuations. In the early ISS experiments, beam splitters and separate mirrors were used to divide and cross the beams [Nelson]. The major advantages offered by the setups described above are the common path optics, made possible by the phase mask, which provides passive phase stabilization. Additionally the fact that the pump and probe beams both pass through the same phase mask pattern ensures that the reference beam is always at the correct angle to provide overlap with the Bragg diffracted probe light for heterodyne detection. Essentially, the pump beams and probe and reference beams image the grating pattern of the phase mask to the sample plane, so the smallest grating period we can generate is given by the phase mask grating period and the numerical aperture of the final lens in the imaging setup. The numerical aperture ( $NA$ ) is defined as

$$NA = n \sin\left(\tan^{-1} \frac{D}{2f}\right), \quad (2.15)$$

where  $n$  is the index of refraction,  $f$  is the lens focal length, and  $D$  is the lens diameter. The  $NA$  in both NIR and visible ISS setups was 0.32 for two-inch diameter lenses with 7.5 cm focal length. On the other hand, the largest transient grating period essentially is given by the imaging ratio, the laser spot size and fluence requirements for adequate signal at the sample, and how close the beams can be without overlapping in the region between imaging optics, allowing for placement of ND filters or a glass plate for heterodyne phase control. With the typical 2:1 imaging this translates to about  $L = 2\text{-}75 \mu\text{m}$  on the NIR setup and  $L = 1\text{-}50 \mu\text{m}$  on the green setup.

## 2.7 Additional approaches for short grating periods

As the transient grating fringe spacing scales with light wavelength (Eq. 2.1), one way to access smaller periods is to utilize a UV source for pump and probe. Other alternatives to increase the  $NA$  of the final lens would involve using larger ( $>2''$ ) diameter optics, aspheric lenses, large reflective optics, microscope objectives, or multiple lens imaging. Each method could significantly reduce the grating period,

but would also present complications that would need to be overcome, such as increased difficulty in alignment or being compatible with a cryostat for temperature controlled experiments. There exist oil immersion microscope objectives with  $NA$  as high as 1.6, but such imaging setups could prove impossible to use with a cryostat, two objectives would be needed with near perfect alignment, a small sample volume would be required for transmission measurements, and the immersive nature of the setup would make reflection measurements significantly more difficult to analyze. In attempting to go to higher  $NA$  setups, there will always be tradeoffs in  $NA$  and working distance that need to be considered. Below we illustrate two methods to perform measurements with increasingly small transient grating periods that could be compatible with temperature-controlled measurements in a cryostat and a variety of sample types.

### **2.7.a Reflective setup**

As an example, in Fig. 2.7.a we show a schematic drawing for a reflective setup that could potentially reach large beam crossing angles, and therefore small transient grating periods. The phase mask splits pump and probe into two beams, which pass the sample on either side. Spherical focusing mirrors cross and focus the beams in the sample and the heterodyne signal can be directed to a detector. Fig. 2.7.b shows the signal in ethylene glycol measured with the described setup with 1030 nm pump and 808 nm probe. Based on the measured frequency of 1.53 GHz and known speed of sound [Silence], the acoustic wavelength was  $\sim 1\text{ }\mu\text{m}$ , almost half the shortest acoustic wavelength possible to excite on the lens-based NIR setup. One difficulty of this approach, or the idea of using short focal length aspheric lenses, is the potential problem of compatibility with an optical cryostat; the cryostat must fit between beams or optics.

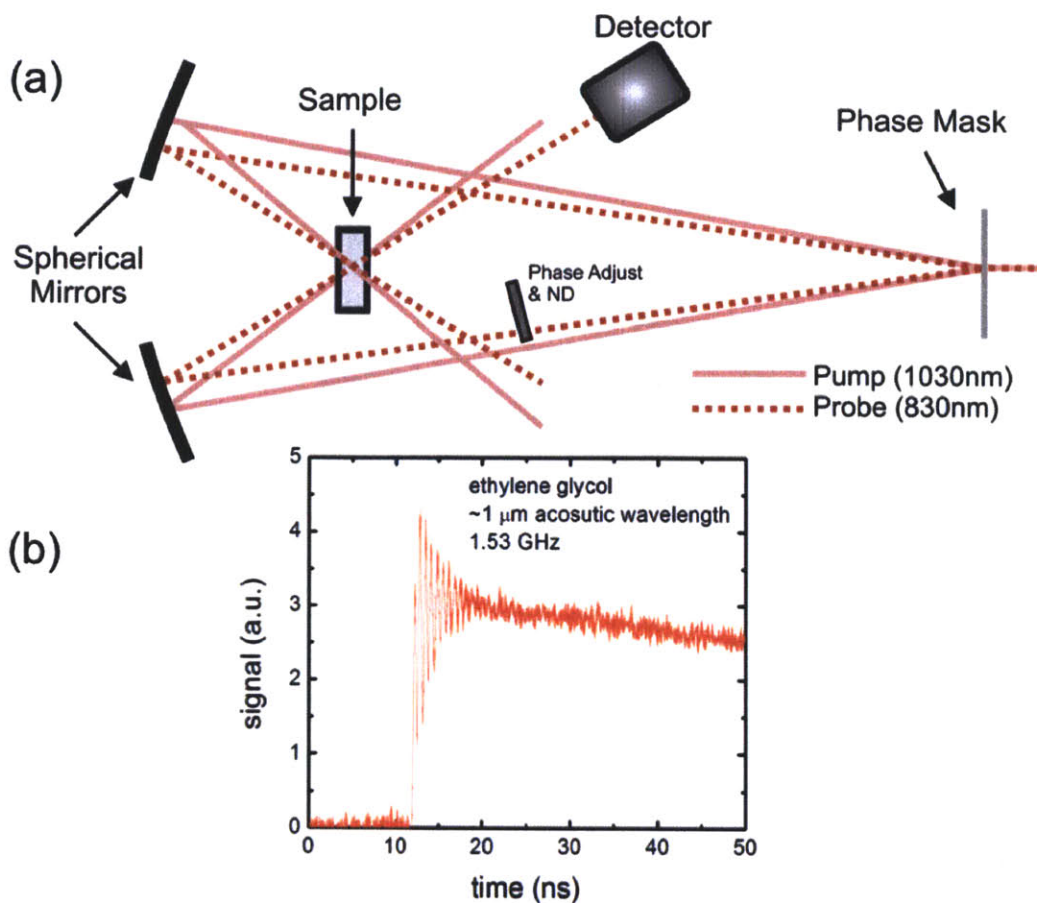


Fig. 2.7. (a) Reflective ISS setup capable of larger beam crossing angles. (b) Recorded trace of ISTS generated acoustic waves at 1.53 GHz in ethylene glycol corresponding to  $\sim 1 \mu\text{m}$  acoustic wavelength.

### 2.7.b. Immersion imaging

It is also possible to incorporate more complex optics with the existing visible and NIR lens setups to increase the numerical aperture, which are also compatible with cryostat use; another lens can simply be added before the sample (as well as after in transmission measurements). For optimal imaging, a positive meniscus lens would be best, but adequate signal has also been observed with short focal length, 1" Thorlabs achromatic lenses as depicted in Fig. 2.8.a. In the case of liquid samples, simply replacing the windows of the liquid sample cell [Halalay] resulted in generation of 720 nm wavelength acoustic waves in the liquid 5-phenyl 4-ether oil (5P4E), also known as Santovac 5, reduced from 1150 nm in the normal sample cell as shown in Fig. 2.8.b. As in liquid-immersion lithography [Hoffnagle], both beams do not enter the sample structure through a single plane so the index of refraction in

the material also contributes to reduction of the interference spacing. This technique offers the distinct advantage of being easily compatible with existing sample cells and cryostat.

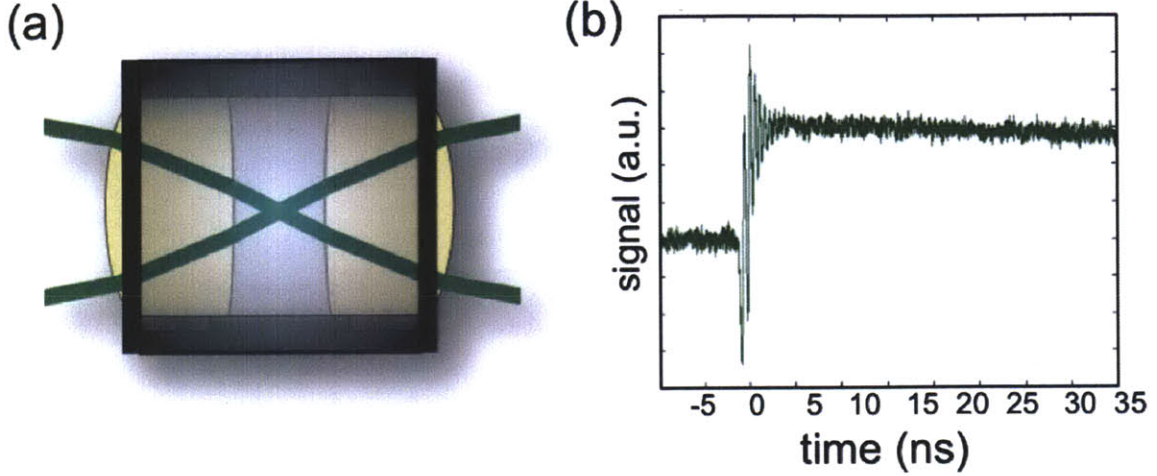


Fig. 2.8. (a) Liquid sample cell with lenses in place of windows to be used in conjunction with lens based ISS setup (see Fig. 2.1). (b) Longitudinal acoustic waves with 720 nm wavelength recorded in liquid 5P4E using lens cell.

## 2.8 Single beam excitation

ISS experiments are wavevector selective measurements. The transient grating wavevector is in truth doubly determined by both the excitation and the probe. In any type of experiment, it is not always necessary to excite a narrowband response in order to probe at a particular wavevector or frequency, and that is indeed the case with ISS. If a single beam is used to photo-excite a broadband acoustic wavepacket, detection of a single wavevector component is still straightforward with the ISS setups described above. In this case, the wavevector components excited in the  $x$  direction are given by the Fourier transform of the laser spot at the focus, given by

$$\frac{1}{\sqrt{2\pi}} \exp\left(-\frac{4q^2 a^2}{4}\right) = \int_{-\infty}^{\infty} \frac{1}{a\sqrt{\pi}} \exp\left(-\frac{x^2}{a^2}\right) \exp(-iqx) dx \quad (2.16)$$

where  $a$  is the  $1/e$  radius of the laser spot. One way to understand and visualize this in comparison with crossing beams to excite a single wavevector as described by Eq. 2.1 is shown in Fig. 2.9.a. A single beam has portions, from either side of the beam, that cross at many different angles and therefore excite a wide range of

wavevectors. But detection at a particular wavevector can still be selected by the probe geometry, as illustrated in Fig. 2.9.b. A single pump beam with small spot size was used to excite a broadband acoustic wavepacket in isopropanol, and signal was monitored via heterodyne detection at the diffraction angle corresponding to  $2\pi/32.5 \mu\text{m}^{-1}$  wavevector, showing damped coherent acoustic oscillations in Fig. 2.9.c.

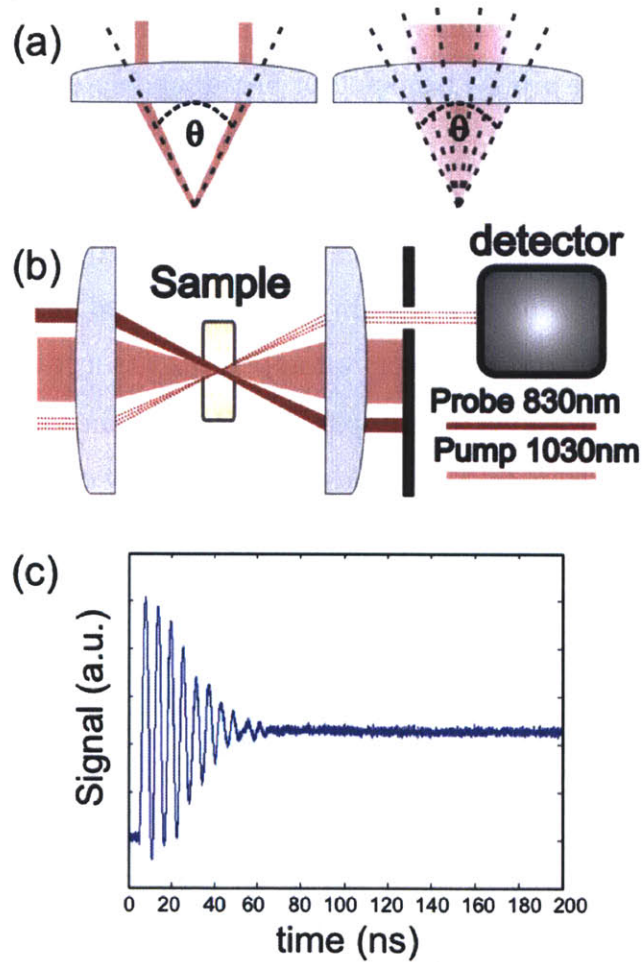


Fig. 2.9. (a) Simple comparison between angular intensity distribution in crossed beams and a single beam. (b) Single-pump, crossed beam probe setup. (c) Broad band excitation, narrow band crossed beam detection of acoustic signal recorded in isopropanol.

The fact that either the pump or probe process can select the wavevector opens the avenue for studying narrowband acoustic properties with a number of broadband acoustic excitations methods. Here we have illustrated the possibility simply due to the material response from absorption by a single laser spot, but optically excited



metal or semiconductor acoustic transducers are also available for generation of broadband acoustic wavepackets. Such high frequency techniques are complimentary to ISS measurements; more details and a short comparison between ISS and high frequency measurements will be offered in Chapter 9.

## **2.9 Point source/point probe – interferometric detection**

The next natural step in progression of pumping and probing geometries is the use of a single pump beam for multiple wavevector, broadband excitation, in conjunction with a single probe laser spot for broadband detection. An experimental setup for such an experimental geometry is illustrated in Fig. 2.10.a, and again we utilize the photoacoustic response in a liquid as a means to understand the methodology, which we call nanosecond acoustic interferometry (NAI). A picosecond duration pump beam is loosely focused in the sample using a spherical lens ( $\sim 200\text{-}300\text{ }\mu\text{m}$   $1/e$  beam radius). Weak absorption leads to heating and thermal expansion through the sample, impulsively generating a cylindrical wave radiating outwards [Patel,Neubrand], with frequency components in the low MHz range. The cylindrical wave is detected at two points in space [Hess] using a phase mask interferometer [Glorieux04]. As the cylindrical acoustic wavepacket passes through the two interferometer arms in succession, a phase difference is created due to density-induced changes in refractive index. As the interferometer arms recombine at the diffraction grating, this translates to time-dependent changes in the intensity of a single beam, which is directed to a detector.

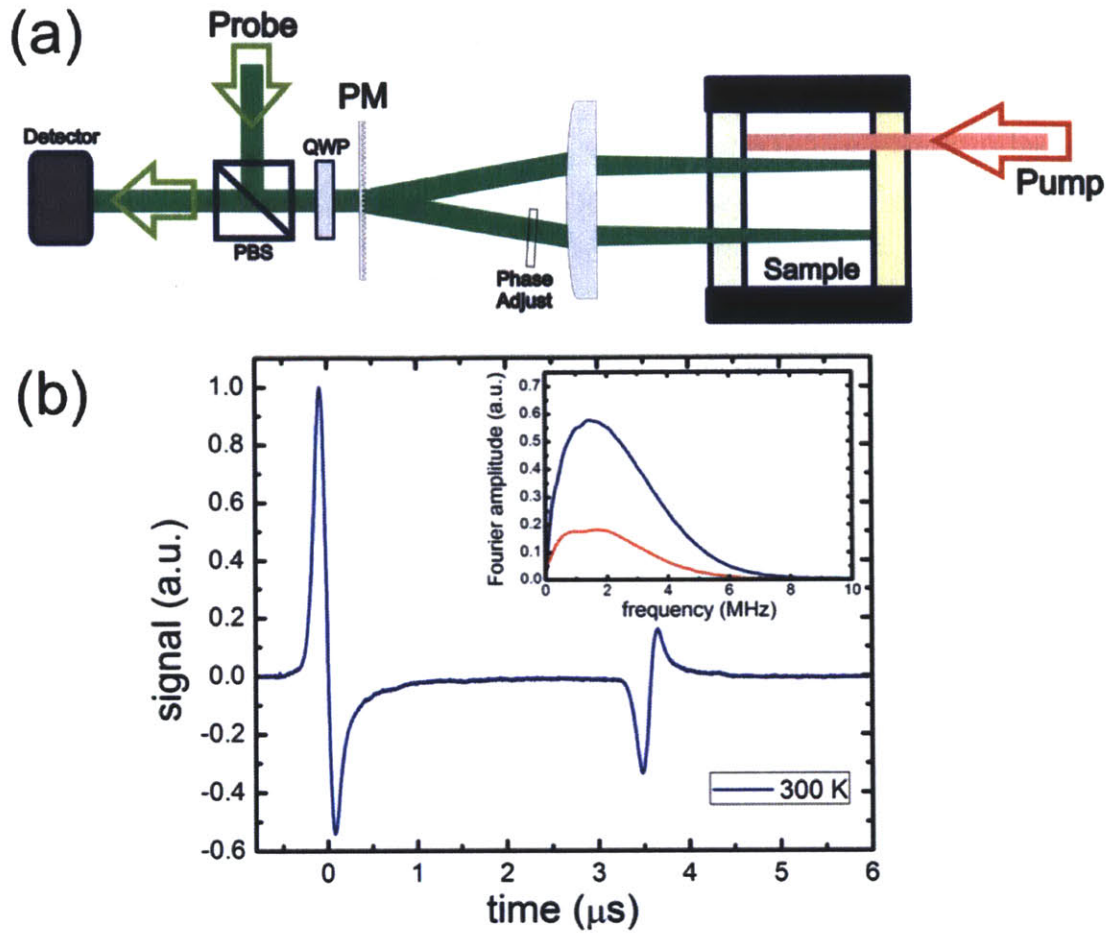


FIG. 2.10. (a) Nanosecond acoustic interferometry setup, where PBS is a polarizing beam-splitting cube, QWP is a quarter wave-plate, and PM is the phase mask. (b) NAI trace recorded in DC704 at room temperature. A pump pulse is absorbed in the sample generating a cylindrical wave radiating outwards. We observe the acoustic pulse passing first through one probe point and then through the second, where the amplitude reduction is clearly observed. The inset shows the Fourier amplitude of the pulse at the first (blue) and second (red) points.

To achieve maximum sensitivity, the incoming continuous wave probe beam passes through, first, a polarizing beam splitting cube (PBS), and then a quarter waveplate (QWP) to induce circular polarization. After passing through the phase mask (PM),  $\pm 1$  diffraction orders are brought parallel and focused by a lens through the sample cell to a dichroic mirror at the back of the sample cell, which reflects the probe beams. The returning beams recombine at the phase mask, pass again through the QWP, and the single beam is the correct polarization for transmission through the PBS to a fast detector. We have also inserted a glass plate in the path of one

interferometer arm that can be rotated for relative phase control. Signals were recorded at relative phases  $-\pi/2$  and  $\pi/2$ , midway between maximum constructive and destructive interference, where the induced phase change, and therefore the detected response, was greatest [Glorieux04]. In Fig. 2.10.b, a recorded trace shows the acoustic pulse generated in liquid DC704 passing through the first probing point at  $t=0$  and the second at longer times. The inset shows the Fourier amplitude of the pulse at each point, where wave amplitude attenuation is apparent. With sufficient signal-to-noise ratio, Fourier analysis can be performed to recover the frequency-dependent speed of sound and attenuation rate data as described in more detail in section 8.1.

## **2.10 Summary**

In this chapter we have described important experimental details of ISS and related optical techniques. Experiments have been carried out aimed at understanding fundamental properties of thermal transport in semiconductors and measuring complex mechanical properties to learn about structural relaxation in supercooled liquids. These will be discussed in subsequent chapters, emphasizing important benefits of the ISS experimental geometry with well-defined transient grating wavevector.







# Chapter 3

## Phonon mediated thermal transport

Active research and development of novel micro- and nano-structured materials indicates the need for a deeper knowledge of material thermal transport properties. Understanding how heat moves over short distances is central to manipulation and management of thermal transport, and thus to development of more efficient nano-electronics as well as thermoelectric materials for solid state power generation [Cahill03]. Indeed the most recent progress in increased thermoelectric efficiency has come by means of reducing the thermal conductivity [Chen03,Dresselhaus,Snyder,Kanatzidis].

In dielectrics and typical semiconductors relevant for thermoelectric or nano-electronic applications, lattice excitations (phonons) are responsible for the majority of thermal transport [Chen98]. In a simplified view, thermal conductivity is directly related to the frequency-dependent phonon mean free path (MFP) and group velocity over the entire thermal distribution of phonons [Callaway,Holland]. A rigorous method for calculating the thermal conductivity involves solving the Boltzmann transport equations [Ziman,Majumdar], with phonons considered as particles, given as

$$\frac{\partial f}{\partial t} + v \cdot \nabla f + a \cdot \frac{\partial f}{\partial v} = \left( \frac{\partial f}{\partial t} \right)_{scattering}, \quad (3.1)$$

where  $f(r,v,t)$  is the phonon distribution function,  $v$  is the group velocity,  $a$  is the particle acceleration (which can be neglected for phonons). The equation here is for a single particle (wavevector), and the term on the right labeled *scattering* accounts for coupling to other phonon modes which will be described in more detail below. In general for phonon-mediated transport, solutions are exceedingly difficult and a number of approximations have been developed to simplify the problem. In the so-called relaxation time approximation (RTA) [Majumdar], the scattering term is approximated using a single lifetime (for each wavevector) and the thermal

conductivity can be calculated as

$$k = \frac{1}{3} \int_0^{\omega_{\max}} v(\omega) c(\omega) \Lambda(\omega) d\omega , \quad (3.2)$$

where  $\omega$  is the frequency of a phonon mode, and  $v$ ,  $c$ ,  $\Lambda$  are respectively mode dependent values of group velocity, heat capacity, and mean free path; Eq. 3.2 essentially communicates how quickly, how much, and how far a particular phonon mode carries heat. Integration is over all phonon frequencies the material supports, and summation of three phonon polarizations is implied, with the  $1/3$  accounting for 3 directions in space.

In this chapter, fundamental factors affecting thermal transport in semiconductors and dielectrics will be described in brief, including the basics of phonon dispersion, heat capacity, and scattering processes that determine the MFP. For a more complete and introductory overview, the reader is directed to [Ashcroft]. For a more in depth and well-presented overview, [Ziman] is very good.

### 3.1 Phonon dispersion

Just as molecular vibrations can be defined by the normal modes of the nuclear motion, so the normal modes of a crystal lattice define the lattice excitations called phonons, defined by polarization, angular frequency  $\omega$ , and wavevector  $k$ . Phonons, like photons, are bosons with motion well described by the wave equation. In isotropic solid materials phonons of three polarizations exist: one polarization that makes up longitudinal phonons with oscillating motion parallel to the propagation direction and two that make up transverse phonons with oscillating motion perpendicular to the propagation direction. In mechanically anisotropic materials (basically all crystals) these motions can be coupled which results in quasi-longitudinal and quasi-transverse waves. In isotropic solids and along some crystallographic directions in anisotropic materials, the two transverse modes will be degenerate. Many phonon properties for the case of one or multiple dimensions can be derived from simple periodic models of balls connected by springs (for

example, see Chapter 22 in [Ashcroft]), and more sophisticated models can involve *ab initio* calculations or molecular dynamics simulations [Henry,Broido,Ward].

In Fig. 3.1 we see the phonon dispersion (phonon mode frequency versus reduced wavevector) for crystalline silicon (Si) along different crystal directions. The open circles are experimentally determined points from inelastic neutron scattering and the solid and dashed lines, which show reasonable agreement, come from an adiabatic bond charge model calculation [Weber].

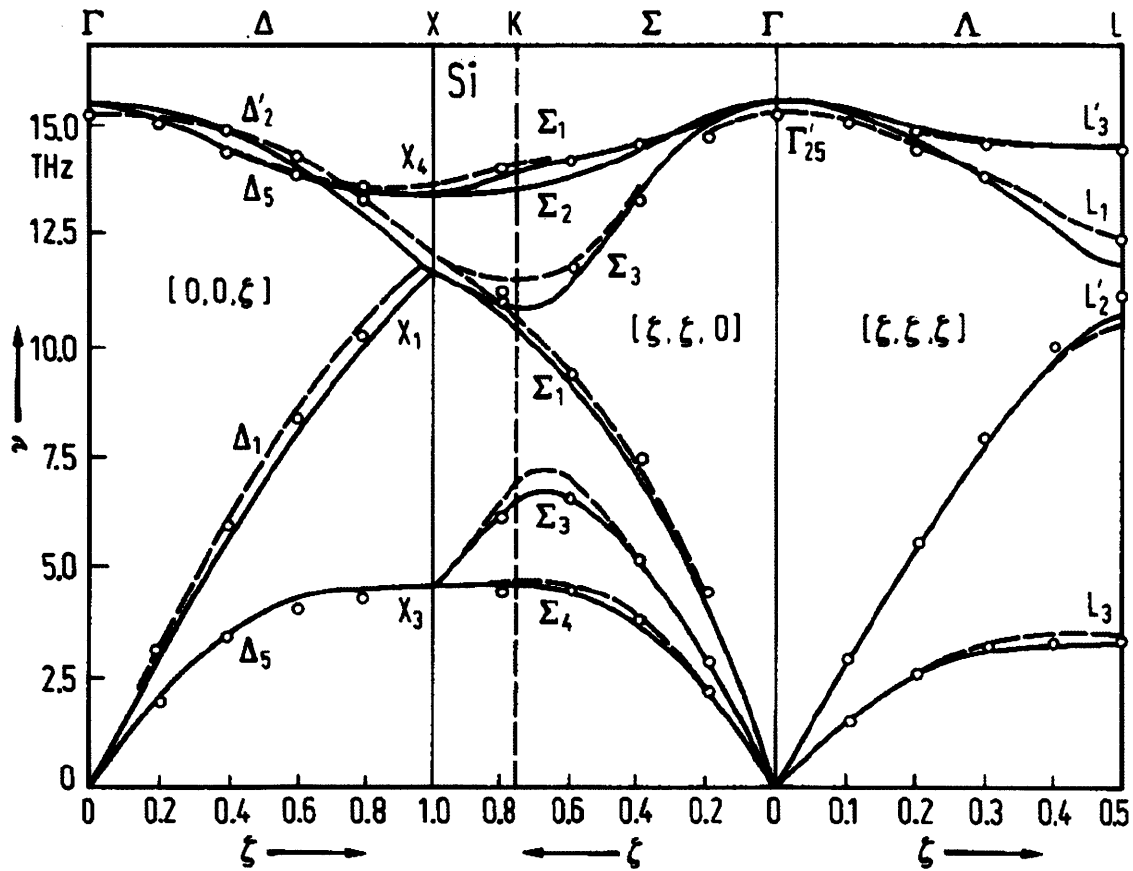


Fig. 3.1 Silicon phonon dispersion curve (adapted from [Weber]). Open circles are experimentally determined points from neutron scattering, and solid and dashed lines are calculations from bond-charge models [Weber].

Starting from the bottom, we see longitudinal branches at higher frequencies and transverse branches at lower frequencies, which are separate in some directions and degenerate in others. The phonon group velocity is given by the slope of the dispersion curve, which gives the speed of sound at low frequencies and approaches

zero at the zone boundary. Low frequency longitudinal phonons typically have group velocities about twice that of transverse phonons in the same direction. In a crystal with more than a single atom in the unit cell, as is the case with Si, zone folding occurs resulting in what we term acoustic phonons at lower frequencies and optical phonons at higher frequencies. We note the relatively flat nature of the optical branches indicative of a low group velocity. The material dispersion curve represents all of the possible phonon modes in a crystal along principle axes, from which the density of states and heat capacity can be determined.

### 3.2 Phonon heat capacity

Historically, it was investigations of the temperature dependence of the heat capacity in a variety of crystalline materials that led to the discovery of the quantum mechanical nature of lattice excitations [Ashcroft]. The differential heat capacity in Eq. 3.1 is given by

$$c(\omega) = \hbar \omega g(\omega) \frac{\partial}{\partial T} n(\omega, T), \quad (3.3)$$

where  $\hbar$  is Planck's constant divided by  $2\pi$ ,  $g(\omega)$  is the density of states, and  $n$  is the occupation number given by the Bose-Einstein distribution. In a three dimensional solid,  $g(\omega)$  is given by the phonon wavevector and group velocity according to  $q(\omega)^2/(2\pi^2 v(\omega))$ . Fig. 3.2 shows the density of states as a function of frequency from the same calculations displayed in Fig. 3.1. Starting at low frequencies we observe the quadratic wavevector dependence and a peak due to the two transverse acoustic branches (T). Following the peak and drop-off, quadratic dependence is again observed due to longitudinal acoustic phonons (L). The peak at  $\sim 14$  THz is due to the large optical phonon density of states (O). As temperature is increased, higher frequency phonon modes are populated in great numbers due to the large density of states, as well as the increased occupation number.

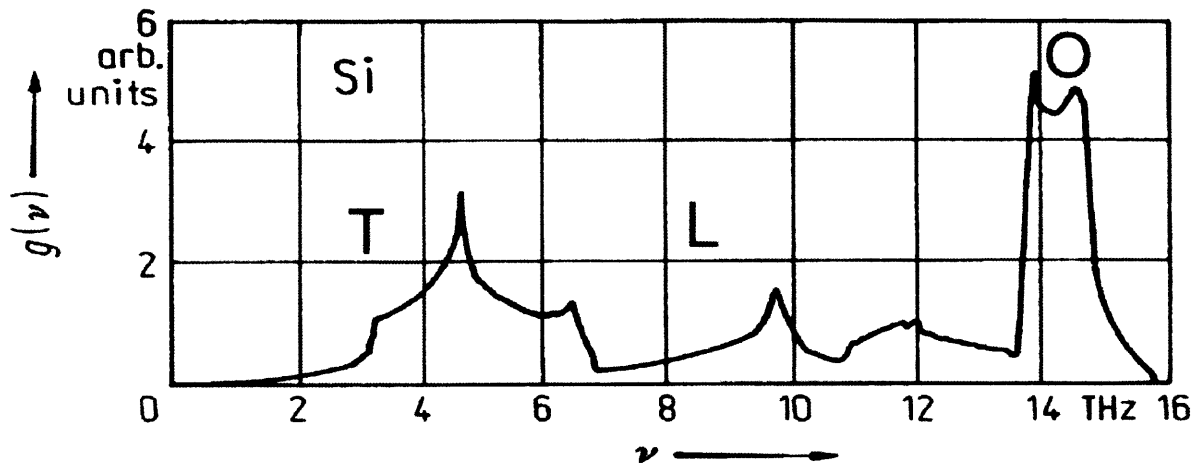


Fig. 3.2. Phonon density of states for Si calculated from bond charge model (adapted from [Weber]). Labels indicate regions dominated by transverse acoustic phonons (T), longitudinal acoustic phonons (L), and optical phonons (O).

### 3.3 Phonon mean free paths

Of the three frequency dependent properties in Eq. 3.2 that are important to calculating the thermal conductivity, the mean free path is the least well understood. A number of factors affect phonon MFPs, including size and interface effects, scattering from sample impurities, isotopes, and crystal defects, and intrinsic non-linear multiple-phonon processes like normal (N) and umklapp (U) scattering [Callaway, Holland]. Here we will loosely define a scattering event that determines the MFP as some process that results in the creation of one (or more) new phonon(s) characterized by a new wavevector and/or energy. Each type of scattering process influences particular portions of the phonon spectrum with a certain temperature dependence that influences the overall temperature dependence of the thermal conductivity. Fig. 3.3 illustrates the typical temperature dependence found in a variety of materials, exhibiting a peak at intermediate temperatures [Brüesch]. As depicted, this is often divided into temperature regions reflecting mechanisms that control relevant phonon MFPs.

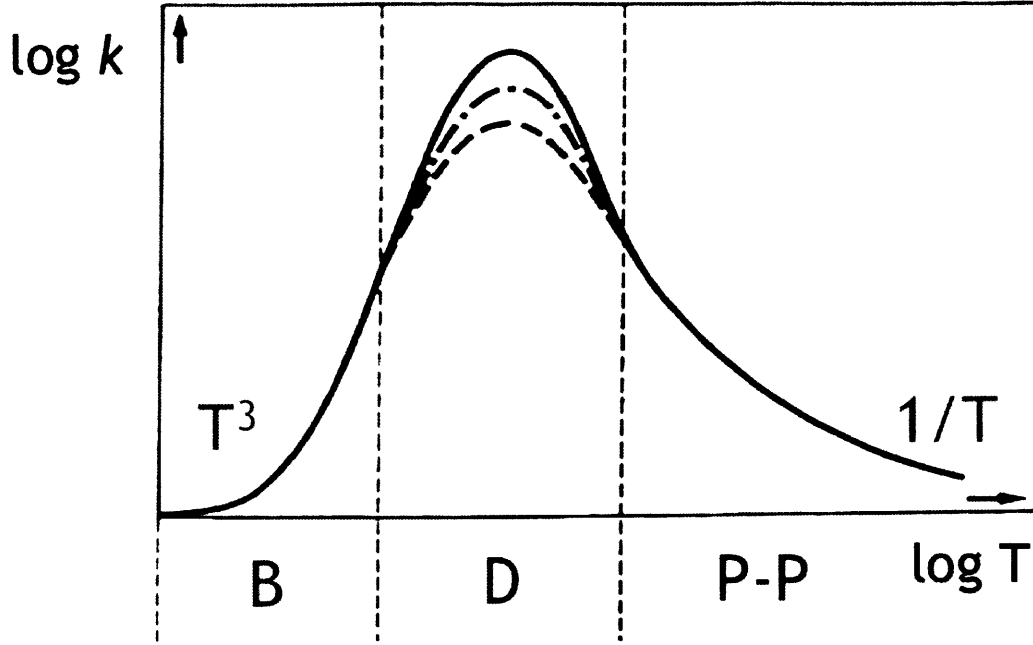


Fig. 3.3. Prototypical thermal conductivity temperature dependence divided into regions with behavior ascribed to MFP determining mechanisms. Such mechanisms are boundary or size effects (B), defect or impurity scattering (D), with different impurity or defect concentrations illustrated by the dashed lines, and intrinsic phonon-phonon scattering (P-P). Adapted from [Brüesch].

The MFP is strongly frequency dependent and can range essentially from macroscopic distances down to the lattice spacing, with long wavelength phonons (sound waves) having the longest MFPs. Thus long wavelength phonons may have MFPs limited by the sample size. At low temperatures where only such low energy phonon states are populated, all MFPs are fixed by the sample size and the thermal conductivity scales with heat capacity showing  $T^3$  behavior.

Scattering also results from isotopes, impurities, or imperfections in the lattice (here we will narrow our definition to point defects such as vacancies). In each of these cases, the scattering cross section  $\xi$  scales with phonon wavevector to the fourth power (Rayleigh scattering) and the change in mass ( $\Delta M$ ) from a perfect lattice site squared,

$$\xi(q) \propto q^4 \Delta M^2. \quad (3.4)$$

In the case of a vacancy,  $\Delta M$  would be the mass of the removed atom. Due to the  $q^4$  dependence, this effect on the thermal conductivity can be dramatic as the temperature is raised and higher frequency phonon modes become populated.



Impurity or defect scattering effects are most often seen as a decrease in the maximum of the thermal conductivity peak as depicted by the dashed lines in Fig 3.3, but also are understood as the reason for low alloy thermal conductivities.

**(a) Normal Scattering**

**(b) Umklapp Scattering**

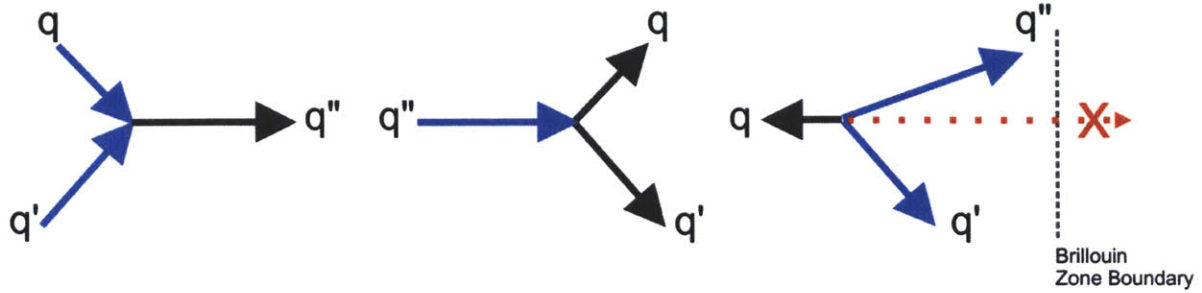


Fig. 3.4 Diagram graphically displaying wavevector selection rules for (a) Normal and (b) Umklapp 3-phonon scattering processes. The lighter arrows are incident phonons and darker arrows are the resulting phonons.

As temperature continues to increase, more and more high frequency phonon states with higher heat capacity are populated. Due to larger numbers of phonons at elevated temperatures, multiple phonon scattering events become significant. In most bulk single crystals at room temperature, the intrinsic N and U scattering rates typically control the phonon mean free path. N and U scattering are fundamentally non-linear three phonon scattering events. In either case, wavevector and conservation of energy selection rules apply, given by

$$\begin{aligned} q + q' &= q'' + G \\ \omega + \omega' &= \omega'' \end{aligned} \quad (3.5)$$

Here,  $G$  is the crystal momentum, and the process is termed Normal when  $G=0$  and Umklapp when  $G>0$ ; the two types of processes are illustrated in Fig. 3.4 where the lighter arrows indicate pre-scattering phonons, and the darker arrows indicate post-scattering phonons.

In the Debye approximation, for N scattering events, the energy flow direction is conserved as either two phonons combine to create one new phonon, or one phonon decays into two phonons (Fig. 3.4.a). Due to the finite size of the Brillouin zone, two phonons of large wavevector magnitude are forbidden to combine to create a new phonon with wavevector outside the first Brillouin zone boundaries. Due to the

lattice momentum ( $G > 0$ , U scattering), a new phonon can be created, but now travelling in the opposite direction, severely disrupting the energy flow (Fig. 3.4.b). Therefore even though N processes will influence the MFP, in the absence of dispersion, U scattering solely contributes to a thermal resistance. A variety of functional forms to describe the frequency dependence of N and U processes have been suggested, but recent first principles calculations in silicon have shown that a scattering rate proportional to  $\omega^2$  seems to be accurate for N processes and  $\omega^4$  for U processes [Ward].

We point out that the RTA, from which Eq. 3.2 is derived, was much criticized in the past [Ziman] but is now viewed as adequate for temperatures on the order of or higher than the Debye temperature. The main point of the criticism was that the RTA does not distinguish between momentum-conserving N-scattering processes and umklapp (U-) processes. Indeed, if only N-processes were present, the RTA would definitely be wrong. However, for high frequency phonons, U-processes dominate [Ward] and hence the distinction is not important. On the other hand, N-scattering of a low-frequency phonon off the high frequency “thermal reservoir” is followed by much faster U-processes within the latter, which redistribute the momentum. Thus effectively the phonon momentum is lost at a dominant rate, which is determined by N-processes for low-frequency phonons and by U-processes for high-frequency ones and can be well approximated by a single rate  $1/\tau = 1/\tau_N + 1/\tau_U$  [Ward]. Recent first-principles calculations of the thermal conductivity of Si [Henry, Broido, Ward] indicated the validity of RTA above  $\sim 100$  K.

A textbook estimate of the average MFP in semiconductors close to room temperature based on simple kinetic theory [Blakemore, Burns] yields 1-100 nm; thus thermal transport over longer length scales is thought to be well described by the classical thermal diffusion model and ballistic effects may only be observed over exceedingly short length scales. On the contrary, an increasing set of experimental and theoretical studies indicate that the effective MFP of heat-carrying phonons in single-crystals can be significantly larger than that cited above [Ju, Chen98], and

indeed a single MFP is an oversimplification in understanding length scales for diffusive versus ballistic transport.

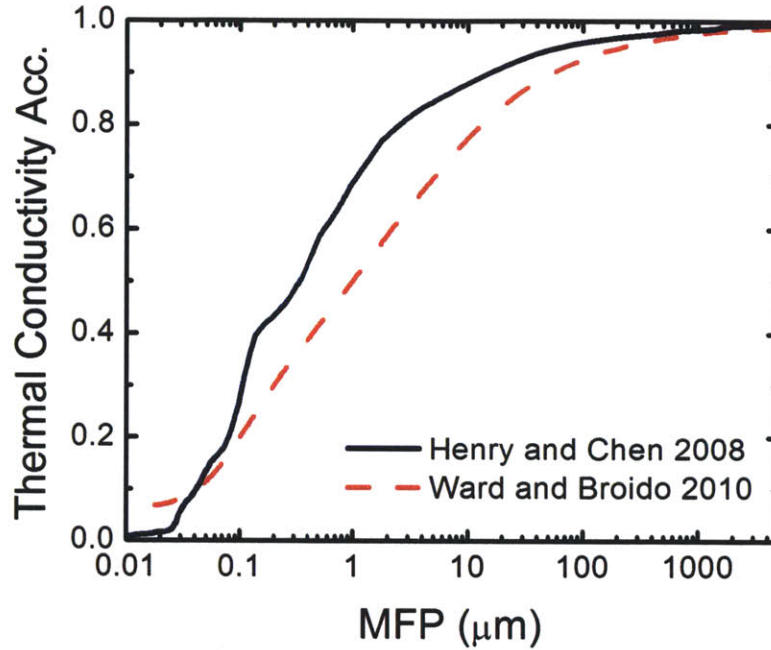


Fig. 3.5. Thermal conductivity accumulation as a function of phonon MFP according to first principles calculations of [Henry] and [Ward]. Although discrepancies exist, the importance of phonons with a wide range of MFPs to thermal transport is evident.

In fact, for any length scale there will be phonons of low enough frequency that propagate ballistically rather than diffusively. The question is therefore how much the relatively long MFP phonons contribute to the heat transport. Until very recently, in order to answer this question one had to resort to guesstimates based on fitting thermal conductivity data with Callaway- or Holland-type models with many free parameters [Callaway, Holland]. In recent years, first principles calculations of thermal conductivity free of fitting parameters have emerged [Henry, Ward, Broido]. To emphasize the utility of such calculations, we plot in Fig. 3.5 the thermal conductivity accumulation as a function of MFP for Si at room temperature according to Henry and Chen [Henry] and Ward and Broido [Ward]. We see that phonons with MFPs ranging over 5 orders of magnitude contribute significantly to the thermal conductivity, demonstrating the gross inadequacy of describing the phonons involved in thermal transport by a single MFP. Although quantitative discrepancies between the different models still persist, they invariably point to an

important role of low-frequency phonons; for example in Fig. 3.5, we see phonons with MFP exceeding 1  $\mu\text{m}$  contribute 40-50% to thermal conductivity of Si at room temperature.

### 3.4 Diffusion equation

The two length scales needed to determine if thermal transport is in the diffusive or ballistic regime are the MFPs of heat carrying phonons and the length scale over which transport is measured. At macroscopic length scales (and even microscopic length scales in many materials), the diffusion equation accurately describes thermal transport, and is thus the basis for thermal conduction modeling in many applications, systems, and geometries (see [Carslaw] for an in-depth treatment). Many of the transient grating measurements presented in this thesis are conducted in the diffusive regime, and thus we derive equations for 1-D diffusive transport relevant to an ISS experiment to give a basic introduction to the formulation. In chapter 4 more complex 2-D equations are given in relation to ISTS surface heating of opaque samples where heat diffuses parallel to the surface, as well as into the depth of the material. The diffusive transport equations are valid in all cases where the MFP of heat carrying phonons is shorter than the length scale of the measurement. In Chapter 5, the contribution of longer wavelength phonons to an ISS thermal grating decay and the crossover from diffusive to ballistic heat transport will be explored further.

The 1-D heat equation with an impulsive, spatially periodic heat source can be written

$$\frac{\partial \delta T}{\partial t} = \alpha \frac{\partial^2 \delta T}{\partial x^2} + \frac{Q}{\rho c_p} \cos(qx) \delta(t), \quad (3.6)$$

where  $\delta T$  is the deviation from equilibrium temperature,  $\alpha$  is the thermal diffusivity,  $Q$  is the energy imparted by the laser,  $\rho$  is the equilibrium density, and  $c_p$  the heat capacity. As described in chapter 2, heat is deposited sinusoidally with wavevector  $q$ . Assuming this sinusoidal spatial dependence of  $T$  and performing a Fourier transform from the time to frequency domain according to  $\tilde{f}(\omega) = \int_{-\infty}^{\infty} f(t) e^{-i\omega t} dt$ , we

arrive at

$$\tilde{T}(q, \omega) = \frac{Q}{\rho c_p (i\omega + \alpha q^2)}. \quad (3.7)$$

An inverse Fourier transform recovers the time dependent solution

$$T(q, t) = \frac{Q\sqrt{2\pi}}{\rho c_p} \exp(-\gamma t) = \frac{Q\sqrt{2\pi}}{\rho c_p} \exp(-\alpha q^2 t). \quad (3.8)$$

From this simple solution, we see that the thermal decay rate  $\gamma$  will depend simply upon the material diffusivity and the transient grating wavevector squared. This linear  $q^2$  dependence is clearly depicted for a decane nanofluid (a suspension of alumina nanoparticles in liquid decane, see [Schmidt08b]) in Fig. 3.6. Here the inverse relationship is plotted – decay time vs. inverse  $q^2$  and the slope of the line gives the inverse thermal diffusivity.

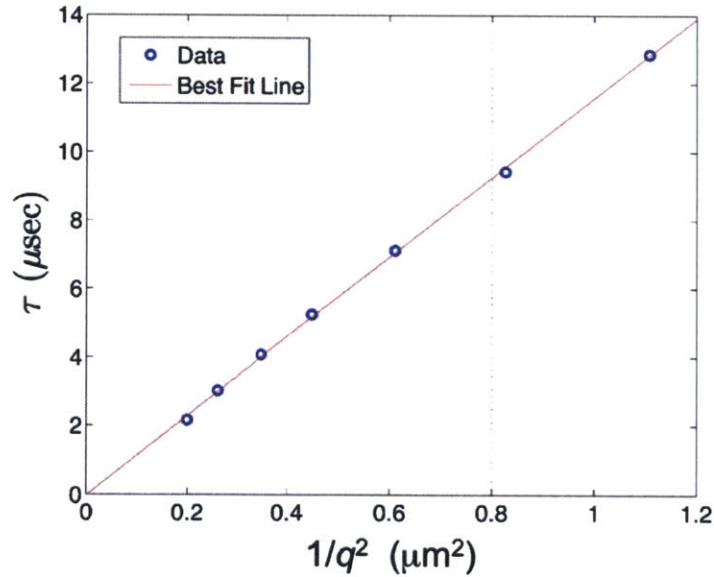


Fig. 3.6. Relaxation time versus inverse wavevector squared for decane nanofluid showing linear dependence (reproduced from [Schmidt08b]). The diffusivity can be extracted from each point or the slope of the line.

### 3.5 Manipulating thermal transport

Because they have nanometer wavelengths, heat-carrying phonons are sensitive to any imperfections at surfaces and interfaces between adjacent materials

[Chen1998,Koh]. Gaining a greater understanding of phonon MFPs and how to



manipulate them is leading to novel materials with custom thermal transport properties; introducing nanostructure such as layers or crystallite boundaries to scatter heat-carrying phonons is becoming an established method to reduce the lattice contribution to thermal conductivity [Kanatidis,Chen2003,Dresselhaus]. As an introduction relevant to experiments discussed in the following chapter, a brief discussion of the effects of a single interface between adjacent materials on phonon propagation will be given, as well as that of multiple interfaces in a superlattice structure.

### 3.5.a Interfaces

Phonons propagate as described by wave mechanics, almost identical to how we describe the propagation of light. Thus as the Fresnel equations include a material dependent wavelength, a change in propagation direction is predicted as a wave crosses a boundary between two materials with different impedances. This is determined by the refractive index for light waves, the analog of which is the acoustic impedance  $Z = \rho v$  for acoustic phonons where  $\rho$  is the material density and  $v$  is the speed of sound. One difference between light and sound waves is that sound waves include both transverse and longitudinal polarizations. When a sound wave is incident at an interface at an oblique angle, a longitudinal motion can result in transverse motion and vice versa, resulting in mode conversion. Thus in an anisotropic material, a single acoustic wave incident to an interface can result in potentially six propagating acoustic waves – three reflected (1 quasi-longitudinal + 2 quasi-transverse) and three transmitted (1 quasi-longitudinal + 2 quasi-transverse). Such mode conversion has a selection rule given by  $k_{x\text{-incident}} = k_{x\text{-result}}$  and is illustrated in Fig. 3.7.a. In certain cases, the wavevector selection rule may not be met for conversion to a particular mode as illustrated in Fig. 3.7.b where we see only two transmitted propagating modes; the third will be a diffusive mode which in optics is termed an evanescent wave. The curves in Fig. 3.7 are called slowness curves and indicate possible wavevectors for slow and fast transverse waves (ST and FT respectively) and longitudinal waves (L) at a GaAs/AlAs interface [Tamura].

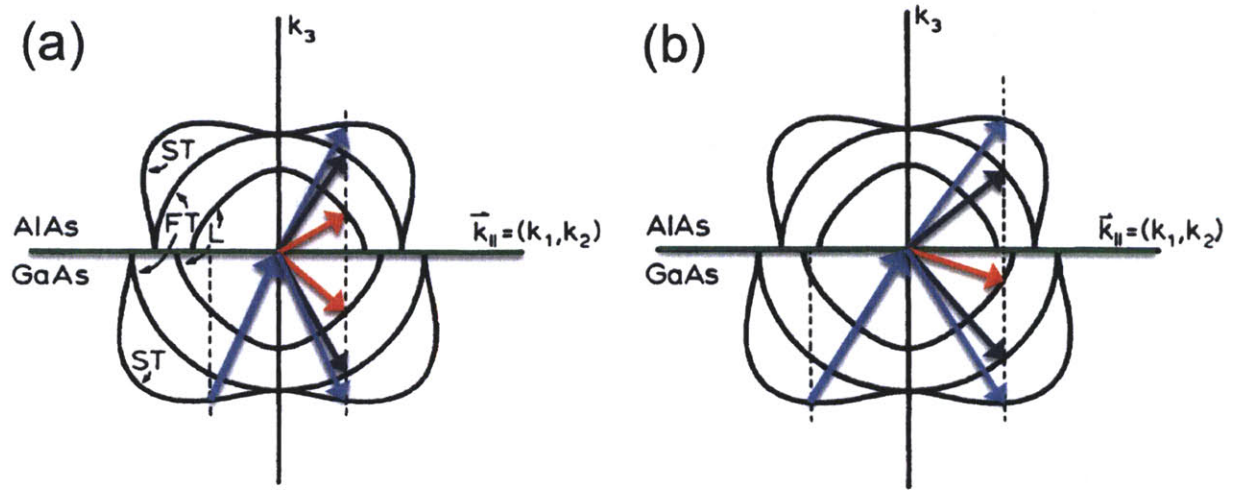


Fig. 3.7. Illustrations of mode conversion at GaAs/AlAs (100) interface (adapted from [Tamura]). (a) Indicates full mode conversion of incident slow transverse (ST) wave to three propagating reflecting waves and transmitted waves: one ST, one fast transverse (FT), and one longitudinal (L). (b) An incident angle that results in only two transmitted propagating waves due to the selection rules.

The preceding arguments are valid in the case of specular reflection, which assumes a perfect interface and is termed acoustic mismatch theory. In reality, just as there are defects in the bulk material, there may be defects and dislocations at interfaces, which can lead to diffuse scattering. In such a case, it has been suggested that phonons scattered at an interface lose all memory of a previous direction or state, and transmission across an interface is proportional to the density of states; this formulation is termed diffuse mismatch theory [Swartz]. As is the case with defect scattering in the bulk, short wavelength phonons will be sensitive to atomic scale defects or interface roughness. Thus whether a phonon sees the interface as specular or diffuse will be highly wavelength dependent. In order to reduce thermal transport, the MFPs of phonons with a variety of wavelengths should be decreased, and so nano- as well as meso-scale structuring can be employed.

### 3.5.b Superlattices

Perhaps the most straightforward means to decrease MFPs due to diffuse scattering at interfaces is to simply build a superlattice (SL) structure with a high interface density. Thus the diffuse mismatch effect will be additive with the number of SL layers. In the case of specular reflection, a number of interesting effects evolve in

periodic superlattices due to constructive and destructive interference wave effects, as is also the case with optical Bragg stacks [Saleh]. Constructive and destructive interference of multiple reflections off interfaces leads to the formation of “stop bands”, which means the transmission coefficient for a particular frequency tends to zero with an increasing number of SL layers. Depending on the acoustic impedances of individual layers composing the SL, stop bands develop with typically only 10-20 SL periods. A look at the dispersion curve indicates that the periodic SL leads to zone folding. This is similar to the zone folding that distinguishes acoustic from optical phonons, but instead of the lattice spacing, it is the SL period that determines where the SL zone boundaries will be. Just like phonons in a bulk crystal, the group velocity goes to zero at the SL zone edge (and center for higher frequencies) and band gaps open (not coincidentally at identical frequencies to the stop bands).

Such a SL transmission and dispersion plot is shown in Fig. 3.8, which we calculated for a 8nm GaAs/8nm AlAs SL according to a transfer matrix technique [Mizuno]. While scattering at interfaces will reduce the MFPs of heat carrying phonons important to Eq. 3.2, the SL dispersion effects modify the material group velocity, essentially cutting out phonons at stop band frequencies from contributing to the thermal conductivity. One important thing to note in real SL structures such as those measured and presented in the following chapter is that there are potentially hundreds or thousands of layers. But the highest frequency phonons may have short enough intrinsic MFPs that they won’t “see” that many layers, thus stop bands may not completely form.



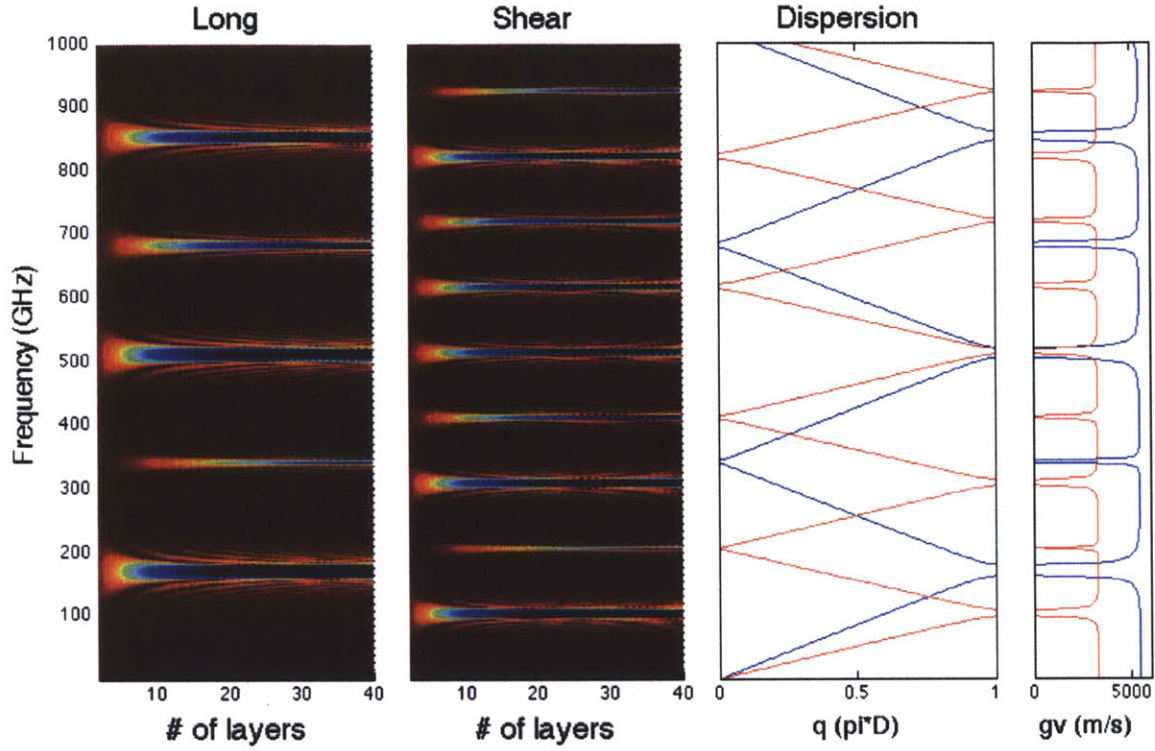


Fig. 3.8. (a) Stop band formation in 8nm GaAs + 8nm AlAs SL. Red indicates complete transmission and blue zero transmission. (b) SL zone folded dispersion curve and group velocity. The red line corresponds to transverse waves and the blue line to longitudinal.

A better understanding of the influence of interface scattering and zone folding on reducing thermal conductivity in real materials is needed. While research in this direction is currently underway in a number of groups, it is still an open question and some means of distinguishing between the two effects independently must be developed.

### 3.6 Summary and experimental techniques

Although progress has been made in manipulating thermal transport, a number of important issues remain unclear. What are the relevant length scales in bulk materials for ballistic versus diffusive thermal transport? Does the acoustic impedance mismatch determine reflection and transmission of phonons at interfaces, or are phonons scattered diffusely? What are the relative contributions to thermal conductivity reduction from rough interface versus zone-folding related effects in superlattices? How strongly do these effects vary with temperature, if at

all? The literature is extensive on these subjects [Chen98,Hyldgaard,Hepplestone] but even with recent advances, clear understanding still awaits in the future. Some of these important issues will be addressed in the following chapters.

These unanswered questions in conjunction with the development of innovative materials create the need for accurate characterization of thermal transport properties. A number of experimental approaches have been developed and utilized to measure thermal transport such as ac calorimetric methods [Hatta,Govorkov] including the  $3\omega$  technique [Cahill], and optical methods including flash [Parker], pump-probe transient thermorefectance (TTR) [Capinski], and transient grating techniques [Harata,Pennington,Rogers93]. Optical measurements of thin-film and other structured materials offer potential advantages over contact methods such as avoiding thermal contact [Fletcher] and interface conductance effects [Lyeo] and offering contactless, non-destructive characterization.

In the transient grating method, which we have previously referred to as impulsive stimulated thermal scattering [Rogers93], two crossed laser pulses create a spatially sinusoidal temperature profile (thermal grating) in the sample and the dynamics of acoustic and thermal responses is monitored via diffraction of a probe laser beam. TG measurements have long proffered accurate and straightforward means for measuring acoustic and mechanical properties of complex samples, and commercial instruments exist for on-line measurements of layered materials [Gostein,Maznev03]. In addition to ascertaining mechanical properties, TG measurements simultaneously allow determination of thermal transport properties [Eichler,Harata,Tokmakoff,Rogers,Käding].

TG measurements can be greatly enhanced by optical heterodyne detection [Goodno,Maznev98] which has become a standard technique adopted for many applications. As briefly outlined in Chapter 2, heterodyning allows separation of so called phase and amplitude grating contributions to the transient grating signal [Terazima,Gedik]. In the next chapter we utilize the phase control to resolve ambiguities in the interpretation of the transient thermal grating signal.





# Chapter 4

## Transient thermal grating measurements in the reflection geometry

### 4.1 Introduction

In this chapter, the methodology for a heterodyned laser-induced transient thermal grating technique for non-contact, non-destructive measurements of thermal transport in opaque material and experimental measurements of a PbTe thin film and GaAs/AlAs superlattices are presented. In materials with weak optical absorption, thermal grating decay is exponential as outlined in section 3.4 and extraction of the thermal diffusivity from the data is straightforward. In opaque materials, the thermal grating is formed at the sample surface and a two-dimensional thermal diffusion equation needs to be solved to determine the temperature dynamics [Käding]. Furthermore, measurements on opaque samples are conducted in reflection geometry with the diffracted probe beam intensity affected both by surface displacement and by variations of the reflection coefficient. The dynamics of the surface displacement and thermorefectance are different [Käding] which further complicates the interpretation of the data. Oftentimes it is simply assumed that the diffraction signal is due to the surface displacement only [Harata], and we will show that this assumption can be highly inaccurate.

Below we introduce the relevant methodology for measuring thermal transport in an opaque sample using the transient thermal grating technique in reflection geometry with phase-controlled heterodyne detection. In every sample we have tested, the phase grating signal includes components associated with both transient reflectivity and surface displacement whereas the amplitude grating contribution is governed by transient thermorefectivity alone. We isolate the thermorefectance component of the signal, which allows direct comparison to a two-dimensional

thermal transport model for the extraction of the thermal diffusivity. Measurements of the in-plane thermal diffusivity of a 5  $\mu\text{m}$  thick single crystal PbTe film yielded excellent agreement with the model over a range of grating periods from 1.6 to 2.8  $\mu\text{m}$ . In-plane thermal diffusion measurements of GaAs/AlAs superlattices were also performed in tandem with transient thermorefectance (TTR) measurements, which are more sensitive to the cross-plane thermal transport, allowing comparison of in- and cross-plane thermal transport on 1-D, and therefore presumably anisotropic, superlattice structures.

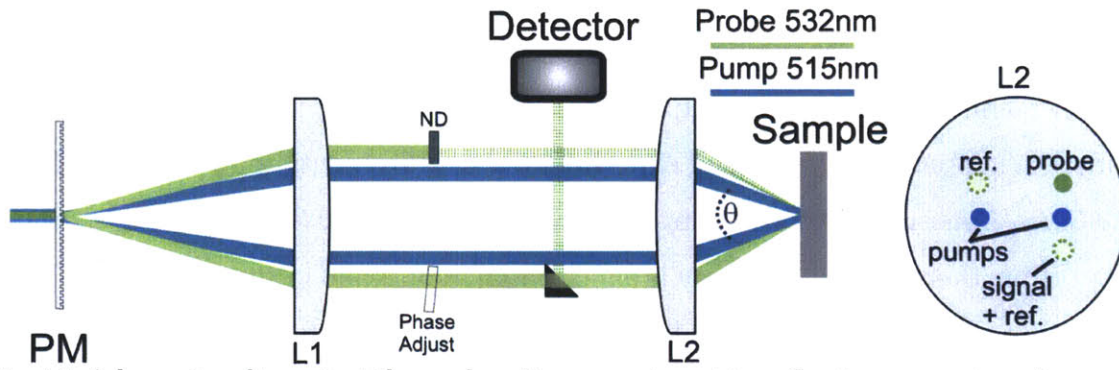


Fig. 4.1. Schematic of transient thermal grating experiment in reflection geometry. A diffractive optic, a binary phase-mask (PM), splits pump and probe into  $\pm 1$  diffraction orders. Pump beams are focused and crossed at the sample surface by a set of lenses (L1 and L2), generating the transient thermal grating. Diffracted probe light is combined with an attenuated reference beam (ND) and directed to a fast detector. The relative phase difference between probe and reference beams is controlled by adjusting the angle of a glass slide (Phase Adjust) in the probe beam path. To the right, the spatial arrangement of beams on L2 is depicted.

## 4.2 Amplitude vs. phase grating signal

In a reflection transient grating experiment as depicted in Fig. 4.1, two short excitation pulses with wavelength  $\lambda_e$  are crossed, at the surface of the sample of interest at an angle  $\theta$ . Optical interference leads to a periodic intensity profile with fringe spacing given by

$$L = \frac{2\pi}{q} = \frac{\lambda_e}{2\sin(\theta/2)} . \quad (4.1)$$

Absorption leads to spatially periodic heating and rapid thermal expansion, resulting in a transient grating with period  $L$  and grating wavevector magnitude  $q$ . There are two main transient grating contributions from which a probe beam can be

diffracted: a static “thermal grating”, of primary interest here, that remains until the heat diffuses away as well as an oscillating, standing-wave grating from impulsively generated surface acoustic waves (SAWs) that persists until the acoustic waves are damped out or simply leave the probing region [Rogers94]. A probe beam with wavelength  $\lambda_p$  is incident on the transient grating. The diffracted light is spatially overlapped with an attenuated reference beam (derived from the same probe source as depicted in Fig. 4.1) and directed to a detector where the time dependent intensity is measured.

Many of the details of the signal formation in the set-up described above have already been presented in section 2.4. But here for a thin, time-dependent reflection grating, again assuming the grating is a small perturbation, the complex transfer function is now a combination of the complex reflection coefficient and phase change due to surface displacement, which we give by

$$t^*(t) = r_0 \left( 1 + \cos(qx) \left[ r'(t) + i \left( r''(t) - 2k_p u(t) \cos \beta_p \right) \right] \right), \quad (4.2)$$

where the dynamic complex reflection coefficient is  $r^*(t) = r_0 [1 + r'(t) + i r''(t)]$ ,  $u(t)$  is the vertical surface displacement, and  $\beta_p$  is the incidence angle of the probe beam on the surface. The first term in square brackets represents amplitude modulation of the incident field while the second term represents phase modulation. Again the diffracted field can be obtained by multiplying the input field (Eq. 2.7) by the complex transfer function [Collier]. For the +1 diffraction order of the probe beam one obtains

$$E_{p(+1)} = r_0 E_{0p} \left[ r'(t) + i \left( r''(t) - 2k_p u(t) \cos \beta_p \right) \right] \exp \left( -i \left( k_p^2 - q^2/4 \right)^{1/2} z + i(q/2)x - i\omega_p t + i\phi_p \right) \quad (4.3)$$

and for the zero order reference beam

$$E_{R(0)} = r_0 t_r E_{0p} \exp \left( -i \left( k_p^2 - q^2/4 \right)^{1/2} z + i(q/2)x - i\omega_p t + i\phi_R \right). \quad (4.4)$$

The two beams are collinear and their interference gives an intensity

$$I_s = I_{0p} R_0 \left[ t_r^2 + r'^2(t) + \left( r''(t) + 2k_p^2 u^2(t) \cos \beta_p \right)^2 + 2t_r \left( r'(t) \cos \phi - \left( r''(t) - 2k_p u(t) \cos \beta_p \right) \sin \phi \right) \right], \quad (4.5)$$

where  $I_{0p}$  is the intensity of the incident probe beam,  $R_0 = |r_0|^2$  is the surface

reflectivity, and  $\phi = \phi_p - \phi_R$  is the heterodyne phase. In the absence of the reference beam, the non-heterodyned diffraction signal is given by

$$I_{non-het} = I_{0p} R_0 \left[ r'^2(t) + r''^2(t) - 4r'(t)k_p u(t) \cos \beta_p + 4k_p^2 u^2(t) \cos^2 \beta_p \right]. \quad (4.6)$$

Thus without heterodyning the signal is comprised of a mixture of real and imaginary transient reflectivity and displacement terms. Since the relative magnitudes of these terms are rarely known beforehand, unambiguous quantitative analysis of this signal would be difficult to say the least. If the reference beam intensity is much greater than that of the diffracted probe ( $t_r \gg r', r'', k_p u$ ), then the time-dependent signal is dominated by the heterodyne term

$$I_{het} = 2t_r I_{0p} R_0 \left[ r'(t) \cos \phi - (r''(t) - 2k_p u(t) \cos \beta_p) \sin \phi \right]. \quad (4.7)$$

If the time dependences of the reflectivity and displacement are different, the temporal shape of the signal will depend on  $\phi$ . By changing  $\phi$ , one can select the signal purely due to an amplitude grating at  $\phi = 0, \pm\pi$ , following the dynamics of  $r'(t)$ , and at  $\phi = \pm\pi/2$  purely due to a phase grating, representing the combination of  $r''(t)$  and  $u(t)$ . Thus while straightforward to isolate the transient reflectivity signal  $r'(t)$ , it is not at all straightforward to isolate the displacement signal  $u(t)$ . Assuming that  $r'(t)$  and  $r''(t)$  follow the same temporal dependence, the displacement signal may be isolated at  $\phi = -\arctan(r'/r'')$ ; however, this requires knowledge of the relative amplitudes of  $r'$  and  $r''$  which is not readily available. Sometimes a distinct known feature in the temporal behavior of the transient reflectivity such as a sharp step can be used to determine  $r'/r''$  (for example, see [Wright]). For our purposes, the preferable strategy for the quantitative analysis of the TG signal is to set  $\phi$  for pure amplitude grating and work with transient reflectivity rather than displacement.

### 4.3 TG experiments on a PbTe thin film

Heterodyne TG measurements were performed on a 5  $\mu\text{m}$ -thick single crystal, undoped PbTe film grown via molecular beam epitaxy (MBE) on a (111) BaF<sub>2</sub>



substrate<sup>1</sup>. The deposition sequence entailed a 30-minute substrate bake at 575 °C to desorb any moisture or native oxide on the surface. After the substrate bake, the temperature was reduced to 325 °C and PbTe film growth was initiated with a 10:1 PbTe/Te flux. Fig. 4.2 is an atomic force microscope image of the PbTe film surface, showing the surface step structure with very low surface roughness (9 Å rms roughness over 10 μm<sup>2</sup>) indicative of a single crystal thin film. We note that the single crystal PbTe film does have a high dislocation density ( $>10^8$  cm<sup>-2</sup>), as determined by cross-sectional transmission electron microscopy, and is due to the PbTe/BaF<sub>2</sub> lattice mismatch producing 4.1% strain. PbTe has shown promise for use in solid-state thermoelectric power generation [Khokhlov] and therefore thermal transport properties of thin films are of interest.

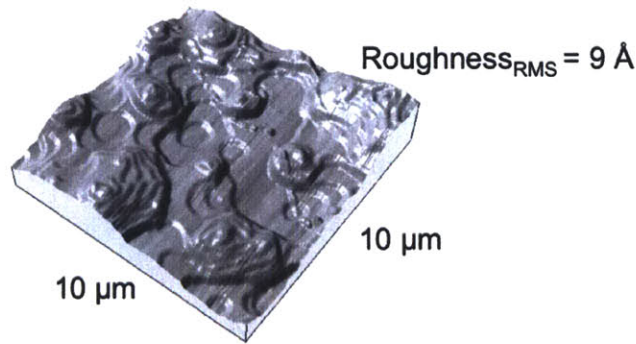


Fig. 4.2 Atomic force microscope image of 10 μm<sup>2</sup> section of the PbTe thin film. The low surface roughness is indicative of a single crystal layer, but it still has a high dislocation density due to the film/substrate strain mismatch.

For these measurements the visible-wavelength ISS setup was used, which entails a short-pulsed laser beam ( $\lambda_e = 515$  nm, second-harmonic of HighQ femtoRegen, 60 ps pulse width, 1 kHz repetition-rate) that is split with a diffractive optic (binary phase mask pattern, PM) into two beams, which are then focused (300 μm 1/e beam radius, 0.66 μJ per pulse total energy) and crossed with angle  $\theta$  at the surface of the sample of interest as depicted in Fig. 4.1. Pump-induced changes in the complex transfer function of the sample will lead to time dependent diffraction of an incident

---

<sup>1</sup> PbTe films were grown by M. Bulsara in E. Fitzgerald's group at MIT and T. C. Harman, S. Calawa, C. J. Vineis, and G. Turner at Lincoln Laboratory.

continuous wave probe beam (532 nm, Coherent Verdi V5, 150  $\mu\text{m}$  radius at the sample, chopped with an electro-optic modulator to 64  $\mu\text{s}$  pulses to reduce sample heating, 8.7 mW average power). In the heterodyne detection scheme as described above, this diffracted light is superposed with a reference beam, derived from the same source and attenuated by a neutral density filter (ND), and directed to a fast detector (Hamamatsu C5658, 1 GHz bandwidth); the temporal signal is observed and recorded on the oscilloscope. The heterodyne phase  $\phi$  is controlled by motorized adjustment of the angle of a glass plate in the path of the probe beam.

In a direct gap semiconductor like PbTe (0.31 eV bandgap at 300 K [Wang]), above gap excitation results in fast thermalization of hot carriers, which promptly relax and transfer energy to the lattice [Siegal, Othonos]. In a TG experiment, energy is deposited with sinusoidal spatial dependence at the sample surface, exponentially decaying with penetration depth  $1/\xi$ . Heat will subsequently diffuse into the depth of the material as well as from grating peak to null parallel to the surface. Initial rapid thermal expansion will also launch counter-propagating surface acoustic waves resulting in a rapidly oscillating standing wave pattern. The combined effect of thermal grating and acoustic waves will lead to a time dependent complex transfer function described by Eq. (4.2). In general, the complex reflectivity may include contributions from changes in temperature (thermoreflectance) as well as strain (photoelasticity). Photoelastic and displacement responses should include contributions of both the thermal grating and acoustic waves whereas the thermoreflectance response includes only the contribution of the thermal grating.

To calibrate the heterodyne phase, we use a transparent liquid reference sample of m-xylene in transmission experimental geometry. The liquid acoustic response yields a pure phase grating signal. It would be preferable to use an opaque reference sample that could be measured in reflection geometry; however, a number of materials we tried, including metals such as Au, Cu, Al and Ni, and semiconductors such as Si and GaAs, invariably exhibited both phase and amplitude grating contributions at the probe wavelength of 532 nm. This underscores the

point that the TG signal from opaque samples cannot generally be ascribed to the surface displacement alone.

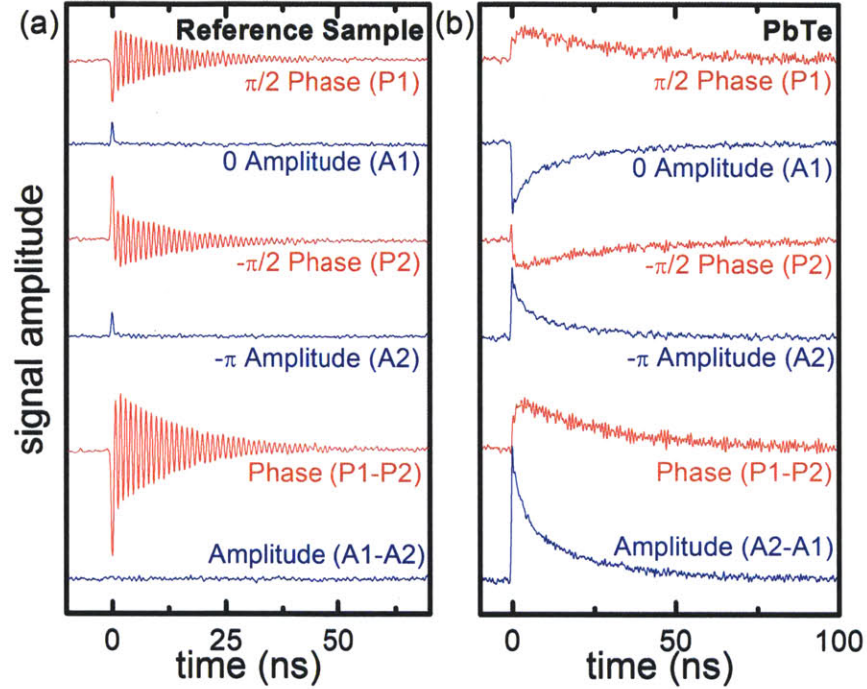


Fig. 4.3. Transient grating data at four phase settings,  $\phi = \pi/2, 0, -\pi/2, -\pi$ , for (a) reference sample liquid m-xylene and (b) PbTe. In the transparent liquid reference sample, only the phase grating shows signal from damped acoustic waves. PbTe also shows acoustic waves only in the phase grating signal, whereas the amplitude grating dynamics are governed by the temperature decay only. Subtraction of signals corresponding to appropriate relative phase settings cancels spurious signals and increases signal to noise as shown in the lowest two traces for each sample.

A transparent sample in which the acoustic waves are generated via electrostriction (i.e., by impulsive stimulated Brillouin scattering [Yan]) ensures that the signal comes from the phase grating only. Switching between transmission and reflection geometries only requires a minor re-configuration of the set-up, and can be accomplished with no reconfiguration at all if separate detectors are used for each scheme.

m-Xylene transient grating signal traces were collected at four phase settings as depicted in Fig. 4.3(a). At  $\phi = \pi/2$  and  $\phi = -\pi/2$  we see decaying acoustic oscillations; the traces are nearly identical except opposite sign, with the only difference due to a small amount of scattered pump light that reaches the detector at  $t=0$ . The

electrostrictively generated longitudinal acoustic waves modulate the density, which couples strongly to the index of refraction. This oscillating periodic index of refraction creates a time-dependent phase grating, and therefore when the acoustic oscillations are maximized, we know that the heterodyne phase is selected so signal is due to the phase grating signal contribution. When the acoustic oscillations are minimized, the signal is pure amplitude grating and due to the absence of an amplitude grating signal in m-xylene, only a spike due to scattered pump light is observed at  $t = 0$ . Once the heterodyne phase is calibrated, we can take measurements from the PbTe sample and observe the pure amplitude or phase grating signal as shown in Fig. 4.3(b). As is particularly apparent in the frequency content of the signals in the inset to Fig. 4.4, we note that surface acoustic wave oscillations are only present in the PbTe phase grating signal. The absence of the acoustic component in the amplitude grating signal indicates that  $r'(t)$  reflects the temperature dynamics rather than the photoelastic response. As can be seen in Fig. 4.3, phase grating signals at  $\phi = \pi/2$  and  $\phi = -\pi/2$ , as well as amplitude grating signals at  $\phi = 0$  and  $\phi = -\pi$ , can be subtracted to cancel any spurious signals with no phase dependence. Examples of spurious signals include the scattered pump light at  $t=0$  in the m-xylene traces and “non-heterodyned” signal components in Eq. (4.5). We also note the difference between PbTe phase and amplitude grating signals is not limited to acoustic oscillations; not unexpectedly the dynamics are totally different: the amplitude grating signal follows the temperature dynamics and the phase grating signal reflects a combination of displacement and temperature dynamics. As will be shown in Sec. 4.6 below, the initial rise of the phase grating signal is explained by the opposite signs of the displacement and thermoreflectance contributions.

By establishing that maximum displacement signal indicates the pure phase grating in PbTe, traces at  $\phi = \pi/2, -\pi/2$ , and  $\phi = 0, -\pi$  can therefore be selected by respectively maximizing or minimizing the amplitude of SAW peaks in the signal Fourier transform in real time on the oscilloscope. For all four heterodyne phase settings, traces of 40,000 averages were collected for transient grating periods  $L = 1.55, 1.80, 2.05, 2.40$ , and  $2.75 \mu\text{m}$ . For the thermal transport analysis described in the



following sections, we used the amplitude grating response obtained by subtracting corrected  $\phi=0$  and  $\phi=-\pi$  signals.

We used the following correction procedure to minimize the error in the heterodyne phase. Let us assume that the signals nominally corresponding to  $\phi_1=0$  and  $\phi_2=\pi/2$  were in fact collected at  $\phi_1=\delta_1$  and  $\phi_2=\pi/2+\delta_2$ , where  $\delta_1$  and  $\delta_2$  are unknown phase errors. According to Eq. (4.9), the respective signal waveforms are given by

$$\begin{aligned} S_1 &= 2t_r I_{0p} R_0 \left[ r'(t) \cos \delta_1 - \left( r''(t) - 2k_p u(t) \cos \beta_p \right) \sin \delta_1 \right] \\ S_2 &= -2t_r I_{0p} R_0 \left[ r'(t) \sin \delta_2 + \left( r''(t) - 2k_p u(t) \cos \beta_p \right) \cos \delta_2 \right] \end{aligned} \quad (4.8)$$

We find the corrected signal as a linear combination  $S_1^* = S_1 + bS_2$ , where the factor  $b$  is adjusted to minimize the SAW Fourier peak in the spectrum of the corrected signal. The value of  $b$  that makes the displacement contribution vanish is  $\sin \delta_1 / \cos \delta_2$ , hence

$$S_1^* = 2t_r I_{0p} R_0 r'(t) \left[ \cos \delta_1 + \frac{\sin \delta_1 \sin \delta_2}{\cos \delta_2} \right] = 2t_r I_{0p} R_0 r'(t) \left[ 1 + \delta_1 \delta_2 - \frac{\delta_1^2}{2} \right] \quad (4.9)$$

Thus the corrected signal  $S_1^*$  recovers the pure amplitude grating response determined by  $r'(t)$ .

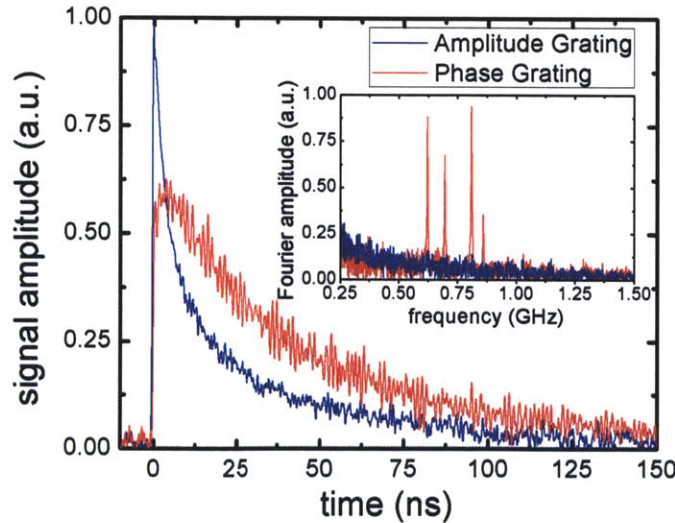


Fig. 4.4. Amplitude and phase grating signals for a  $2.05 \mu\text{m}$  grating period. The Fourier transform inset shows four thin film waveguide acoustic modes originating from the displacement contribution to the phase grating signal. The amplitude grating signal tracks temperature dynamics and is not influenced by the displacement.

#### 4.4 Analysis of the thermal transport

In analyzing the thermal grating decay, we follow [Käding] but allow for a finite absorption depth of the excitation light. Temperature dynamics following transient grating heating at the surface of a semi-infinite sample are given by the thermal diffusion equation

$$k_x \frac{\partial^2 T}{\partial x^2} + k_z \frac{\partial^2 T}{\partial z^2} = \rho c \frac{\partial T}{\partial t} + Q_0 \cos(qx) \exp(-\xi z) \delta(t), \quad (4.10)$$

where  $x$  is the grating dimension,  $z$  is into the depth of the material,  $T$  is the deviation from equilibrium temperature,  $\rho$  is density,  $c$  is heat capacity,  $Q_0$  is the energy deposited by the short ( $\delta$ -function) laser pulse to penetration depth  $1/\xi$ , and  $k_x$  and  $k_z$  are the thermal conductivity components respectively parallel and perpendicular to the sample surface (the  $z = 0$  plane), which are not assumed to be equal to incorporate the treatment of samples with anisotropic thermal transport. Appropriate boundary conditions at the surface are given by

$$\begin{aligned} \frac{\partial T}{\partial z}(z=0) &= 0 \\ T(z=\infty) &= 0 \end{aligned} \quad (4.11)$$

Assuming a sinusoidal spatial dependence of  $T$  on  $x$  according to the source term in Eq. (4.10) and performing a Fourier transform from the time to frequency domain according to  $\tilde{f}(\omega) = \int_{-\infty}^{\infty} f(t) e^{-i\omega t} dt$ , we arrive at

$$\frac{\partial^2 \tilde{T}}{\partial z^2} = \frac{\alpha_x q^2 + i\omega}{\alpha_z} \tilde{T} + Q_0 \exp(-\xi z), \quad (4.12)$$

where  $\alpha_i = k_i/\rho c$  is the thermal diffusivity and the boundary conditions are identical to Eq. (4.11). Using solutions for the homogenous and particular solutions respectively of the form

$$\begin{aligned} \tilde{T} &= A \exp(-\varphi z) + B \exp(\varphi z) \\ \tilde{T} &= C \exp(-\xi z) \end{aligned} \quad (4.13)$$

and utilizing the boundary conditions gives us the analytical frequency-domain solution

$$\tilde{T} = \frac{Q_0}{\varphi^2 - \xi^2} \left( \exp(-\xi z) - \frac{\xi}{\varphi} \exp(-\varphi z) \right), \text{ where } \varphi = \sqrt{\frac{\alpha_x q^2 + i\omega}{\alpha_z}}, \quad (4.14)$$

and time-domain solutions may be recovered through numerical inverse Fourier transform. This treatment can easily be extended to multi-layered structures [Käding].

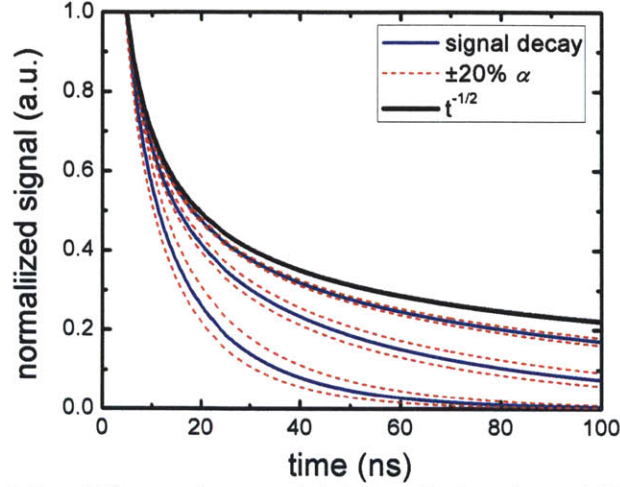


Fig. 4.5. Simulation of signal illustrating sensitivity to the in-plane diffusivity  $\alpha$  as a function of transient grating period. The solid blue lines are simulated traces for an in-plane diffusivity of  $1.3 \times 10^{-6} \text{ m}^2/\text{s}$  for TG periods of 1.1, 2.1, and  $4.3 \text{ }\mu\text{m}$  from shortest to longest decay time, and the solid black uppermost line shows  $t^{-1/2}$  decay. The dotted red traces are  $\pm 20\%$  values of the diffusivity and show high sensitivity for small periods and decreased sensitivity at larger periods as the signal approaches the  $t^{-1/2}$  decay due to diffusion into the depth of the material.

To better understand the time domain decay, we refer to the analytical solution in the limit of surface heating ( $1/\zeta = 0$ ). The temperature grating decay at the surface then follows the form [Käding]

$$T(z=0) = A_T (\alpha_z t)^{-1/2} \exp(-\alpha_x q^2 t). \quad (4.15)$$

In this case, the transient grating measurement is insensitive to the cross-plane diffusivity  $\alpha_z$  because changing it is equivalent to changing only the amplitude  $A$  of the signal. On the other hand, the in-plane thermal diffusivity contained in the exponentially decaying term can be determined by fitting the signal waveform. In Fig. 4.5, we see illustrated the signal decay as modeled by Eq. 4.15 for three grating wavevectors. The heavy dark line denotes a  $t^{-1/2}$  decay. As the wavevector gets small (large grating period), it takes more time for heat to diffuse from grating peak to null. As the decay gets longer, the long tail of the  $t^{-1/2}$  decay starts to dominate the

signal. This leads to less sensitivity to the in-plane diffusivity, as clearly indicated by the dotted traces with  $\pm 20\%$  values of the diffusivity.

We note that Eq. (4.15) diverges at  $t = 0$ . This is not the case for the full solution given by the inverse Fourier transform of Eq. (4.14) that accounts for the finite penetration depth of the laser heat source, which essentially smoothes out the diverging temperature over an initial time period  $\Delta t = (4\alpha_z \zeta^2)^{-1}$ . Therefore analyzing the initial part of the signal may help determine the cross-plane diffusivity. However, due to limits in temporal resolution and potential complications due to excited carrier diffusion, we fit the decay after 10 ns to extract only the in-plane diffusivity. Typical transient thermoreflectance (TTR) measurements [Schmidt08a] are more sensitive to the cross-plane diffusivity, so TTR and TG measurements can be used in tandem to potentially reveal anisotropic thermal transport properties, as described below in section 4.7.

#### 4.5 Thermal diffusivity measurement of PbTe film

Fig. 4.6 shows the amplitude grating signal for three representative grating periods along with the fit, which shows excellent agreement. The extracted thermal diffusivity was nearly identical for all data sets as shown in the inset to Fig. 4.6, giving an average value of  $1.32(\pm 0.03) \times 10^{-6} \text{ m}^2/\text{s}$ . The fact that for a range of grating periods we get an excellent fit yielding the same value of  $\alpha_x$  testifies to the soundness of our methodology. The determined thermal diffusivity is lower than the accepted value for bulk single-crystal PbTe of  $1.8 \times 10^{-6} \text{ m}^2/\text{s}$  at room temperature [Lide], but we note that a PbTe thin film deposited on BaF<sub>2</sub>, although single crystal, is prone to a high dislocation density ( $>10^8 \text{ cm}^{-2}$  determined for similar samples from XTEM images) due to the lattice parameter mismatch (i.e., introduction of 4.1% strain). Dislocations are expected to increase phonon scattering and reduce thermal transport [Cahill, Swartz] and a similar reduction has been observed in GaN at room temperature for comparable dislocation densities [Mion].



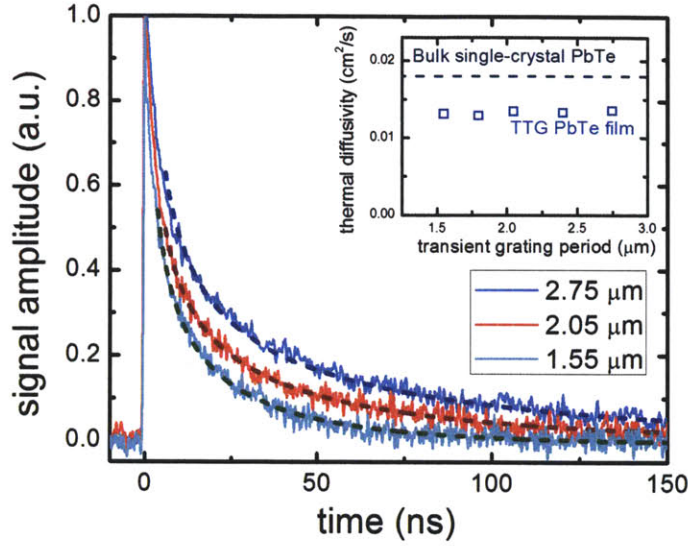


Fig. 4.6. Amplitude grating signal for PbTe film for three representative transient grating periods (1.55μm, 2.05μm, and 2.75μm). The darker dashed line with each trace is the best-fit line using the 2-D diffusion equation. The inset shows the literature PbTe thermal diffusivity in comparison with the measured thin film diffusivity at different transient grating periods.

The thermal grating period is always smaller than the film thickness; therefore, the presence of the BaF<sub>2</sub> substrate should have no effect on the analysis. Indeed, assuming a cross-plane thermal diffusivity equal or close to the measured in-plane diffusivity, the thermal penetration depth  $2(\alpha t)^{1/2}$ , where  $t=150$  ns is the time window of the experiment, will only be  $\sim 1$  μm, substantially shorter than the 5 μm PbTe film thickness.

#### 4.6 Modeling the phase grating signal

Even though we chose to use the amplitude grating signal for the thermal diffusivity measurements, the treatment of the subject matter would be incomplete without demonstrating that our model provides an adequate description of the phase grating signal as well. In particular, the initial dynamics of the phase signal poses an intriguing question. Both thermorefectance and displacement contributions to the TG signal are expected to reach a maximum immediately following the excitation pulse at  $t=0$  and decay thereafter (assuming the thermal expansion time is fast compared to the time scale of measurement). Yet the phase grating signal initially rises and reaches its maximum at  $t\sim 4$ ns. This behavior can be explained if we

assume that thermoreflectance and displacement contribute to the phase grating signal with opposite signs.

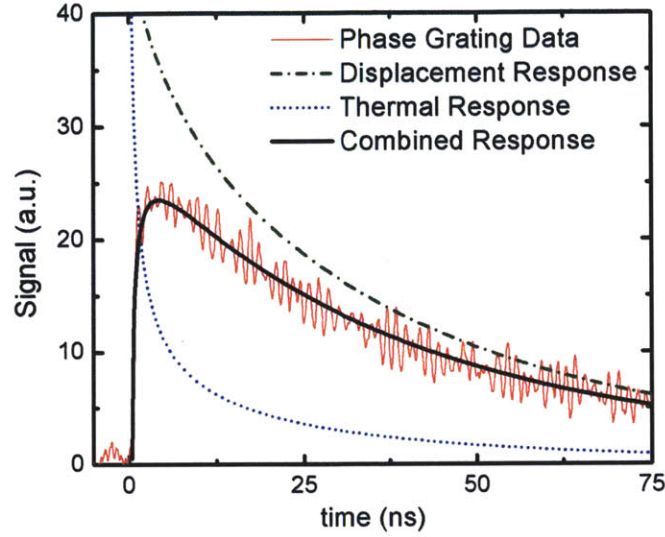


Fig. 4.7. Phase-grating signal for 2.05  $\mu\text{m}$  transient grating period. The dash-dotted green and dotted blue lines are respectively the calculated surface-displacement and thermal responses. The black line, the surface-displacement response minus the thermal response, represents the more complicated dynamics of the phase-grating signal.

According to Eq. (4.6), the phase grating signal is governed by the combination of thermoreflectance and displacement,  $r''(t) - 2k_p u(t) \cos \beta_p$ . Assuming a small absorption depth,  $1/\xi \rightarrow 0$ , which is a good approximation for PbTe at 515nm excitation wavelength, and isotropic thermal diffusivity, the surface displacement dynamics is given approximately by [Käding] (neglecting a fast initial rise)

$$u(t) = A_u \text{erfc}(q\sqrt{\alpha t}) . \quad (4.18)$$

Fig. 4.7 shows the phase grating signal from Fig. 4.4 together with calculated traces using the thermal diffusivity determined from the amplitude grating data. The dash-dotted line shows the pure surface-displacement response according to Eq. (4.18) and the dotted line shows the pure thermal response according to Eq. (4.15). The solid dark line, which has excellent agreement with the phase grating data, is a linear combination of the calculated displacement and thermal responses, taken with the opposite signs. Thus the phase grating signal follows neither displacement nor temperature dynamics. To use this signal for quantitative analysis of the

thermal transport, one would need to use an additional fitting parameter, i.e., the ratio of the transient reflectivity and displacement contributions to the phase grating signal. Such analysis might prove useful for samples yielding a weak amplitude grating signal and a strong phase signal.

#### **4.7 In- vs. Cross-plane thermal diffusivity of GaAs/AlAs superlattices**

The developed methodology has proven successful in measuring thermal transport in a number of semiconductor samples in addition to the PbTe measurements described. As discussed in Chapter 3, introducing interfaces is a means to reducing thermal transport. Understanding thermal transport in superlattice (SL) structures has applications in developing novel materials for thermoelectrics applications, as well as increasing the performance of optoelectronic devices such as semiconductor lasers. It has been shown that the thermal transport in one-dimensional SLs both across and parallel to the layers is greatly reduced from what one might expect from average values of the bulk thermal conductivities of the materials constituting the SL [Chen98]. As a model SL system, we have conducted optical measurements of the in-plane thermal transport using the transient grating technique illustrated here in conjunction with cross-plane measurements utilizing transient thermoreflectance (TTR) [Paddock,Capinski,Schmidt08a,Stevens]. Measurements of cross- and in-plane thermal transport have been conducted in GaAs/AlAs SLs [Capinski,Yao,Chen], but this constitutes the first comparison using all optical techniques and, importantly, identical samples.

##### **4.7.a SL samples**

Two sets of GaAs/AlAs thin film superlattice samples were fabricated via metalorganic chemical vapor deposition in an Aixtron close-coupled showerhead reactor<sup>2</sup>. The epitaxial films were deposited on (100) oriented GaAs substrates, which were held at a deposition temperature of 700 °C. One GaAs/AlAs superlattice structure consisted of 8 nm GaAs/8 nm AlAs (total period of 16 nm) repeating units

---

<sup>2</sup> Superlattice samples were grown by A. Jandl and M. Bulsara in E. Fitzgerald's group at MIT.



and the other consisted of 2 nm GaAs/2 nm AlAs (total period of 4 nm) repeating units. The total thickness for each superlattice thin film structure was 3  $\mu\text{m}$  (see Fig. 4.8). Fig. 4.8 also shows a cross-sectional transmission electron microscopy image of region of the 8 nm GaAs/8 nm AlAs superlattice structure showing the alternating layers of AlAs and GaAs and the abrupt interfaces between all the layers. High-resolution x-ray diffraction scans of both samples showed diffraction peaks associated with the additional periodicity from the superlattice structure; peak positions affirmed periods of 16 and 4 nm.

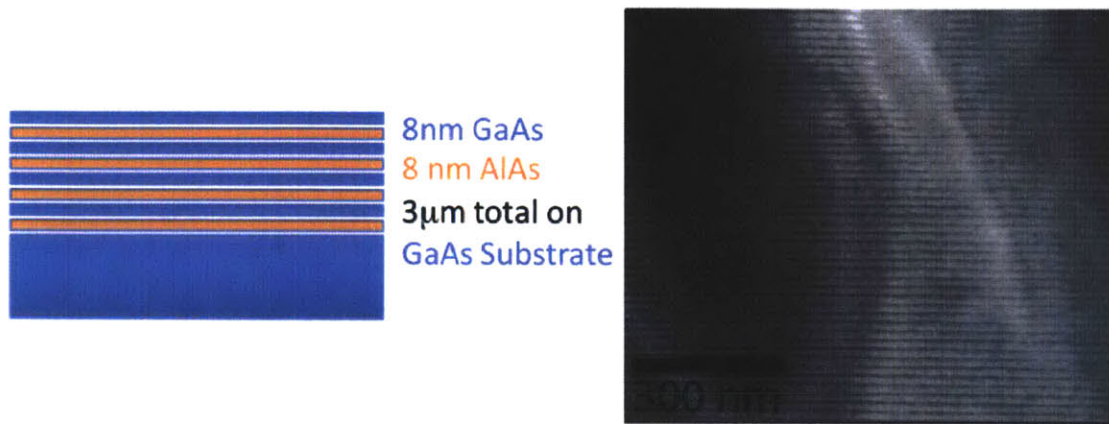


Fig. 4.8. Diagram indicating entire sample structure and cross-sectional transmission electron microscopy image of 16 nm period, GaAs/AlAs thin film superlattice structure grown on GaAs substrate. The AlAs (light contrast) and GaAs (dark contrast) layers are of the requisite thickness and exhibit sharp interfacial characteristics. The 4 nm period SL has a similar sample structure with the same total SL thickness.

#### 4.7.b TG In-plane and TTR Cross-plane measurements

We measured the in-plane thermal diffusivity on the both SL samples with an identical setup and procedure as was used for PbTe, except with a pump energy of 0.8  $\mu\text{J}$  per pulse. By comparison to the m-xylene reference sample, it was found that the amplitude grating signal did not contain any acoustic components, and thus the Fourier amplitude of SAWs was again used for isolation of amplitude and phase grating signals. The resulting isolated signals for a 2.4  $\mu\text{m}$  grating period in the 16 nm period SL are shown in Fig. 4.9.a. In Fig. 4.9.b we see amplitude grating decays for four grating periods fit to Eq. 4.15 to obtain the thermal diffusivity; the short dashed lines indicate the fits, and again, we see good agreement between the signal

traces and theory. Similar signal quality and results were obtained for the 4 nm period SL.

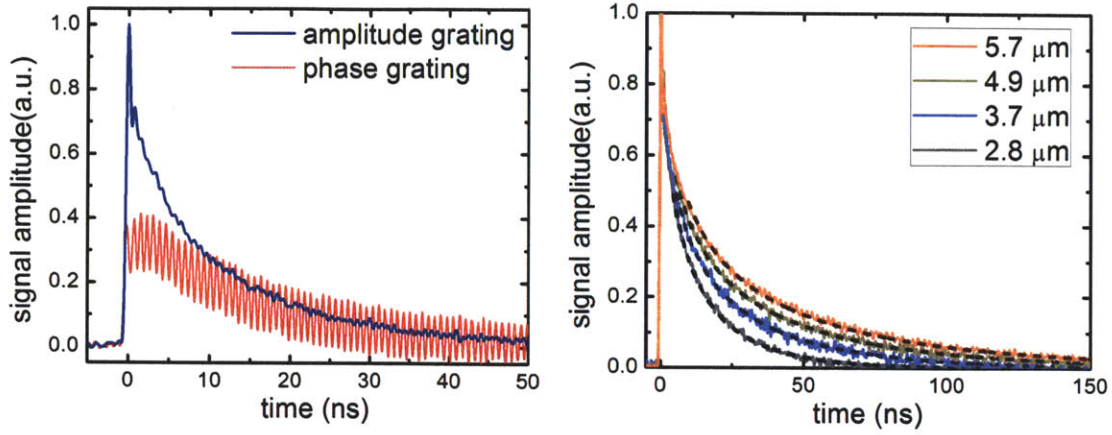


Fig. 4.9 (a) Isolated amplitude and phase grating signal for the 16 nm period GaAs/AlAs SL collected with 2.4  $\mu\text{m}$  grating period. (b) Amplitude grating decays for the 16 nm period SL at four grating periods as indicated in the legend, which show good agreement to the fit (dashed lines).

Transient thermorefectance (TTR) measurements are essentially single-spot, pump-probe measurements that are predominately sensitive to cross-plane thermal transport. A femtosecond optical pulse was incident on a thin metal transducer (aluminum) coated on the SL sample surface and the intensity of a second, variably time-delayed probe pulse is monitored. The probe intensity is related to the temperature of the sample surface, and the signal decay can be modeled using the heat diffusion equation to recover the thermal transport properties of the underlying sample. The details of TTR are explained in depth in the literature [Capinski,Schmidt08a] and won't be described in full here. In Fig. 4.10 we show a TTR trace for the 16 nm period SL at room temperature<sup>3</sup>. The circles are the recorded reflectivity points and the solid green line is a best fit of the model to the data, which incorporates the Al transducer layer, the interface conductance between the Al and SL structure, and models the SL as a single material. The dotted lines are fits with  $\pm 10\%$  values of thermal conductivity demonstrating the sensitivity to the cross-plane thermal conductivity.

<sup>3</sup> TTR measurements reported here were performed by M. Luckyanova in G. Chen's group at MIT.



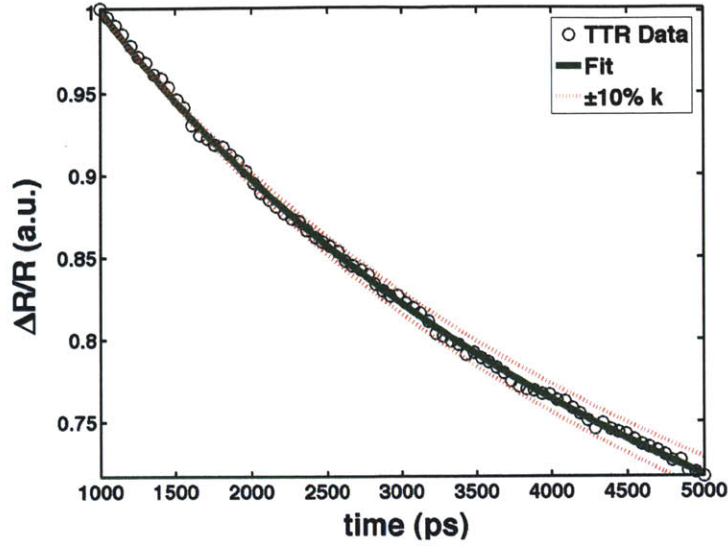


Fig. 4.10 Recorded TTR trace for 16 nm period GaAs/AlAs SL. The green line is from a best fit to the model and the red dotted lines are calculated according to the model with  $\pm 10\%$  values of the best fit thermal conductivity value.

#### 4.7.c SL thermal transport results and discussion

The resulting measured thermal diffusivities are plotted as open squares (16 nm period) and triangles (4 nm period) and dashed lines (TTR results for 16 and 4 nm periods) in Fig. 4.11. In Fig. 4.11.a we see that in- and cross-plane diffusivities for both SL samples are dramatically lower than an average of bulk GaAs and AlAs diffusivities (given by the dashed purple line), with the shorter period SL having a slightly lower in-plane thermal diffusivity. In Fig. 4.11.b we see that, as anticipated, the cross-plane diffusivities are lower than the in-plane diffusivities in both SLs. We measure  $0.069 \pm 4\%$  and  $0.042 \pm 10\%$  for respectively in- and cross-plane values for the 16 nm period SL and  $0.049 \pm 6\%$  and  $0.043 \pm 10\%$  for respectively in- and cross-plane values for the 4 nm period SL. This results due to considerations given in section 3.5. Phonon scattering may occur at each interface in these 1-D layered structures, and the interface density will vary with angle of phonon propagation, leading to anisotropic effects. Additionally, the SL dispersion effects depend on the propagation direction with respect to the SL, with reduced modification of phonons traveling perpendicular to the SL layers (the in-plane direction). Thus based on these arguments, one would expect significant anisotropy in the transport properties. When comparing to the bulk effective value, the differences in cross-

and in-plane thermal diffusivities is in fact not as great as have been measured in similar Si/Ge superlattices [Liu01, Lee, Chen98] at a variety of temperatures, including ambient conditions.

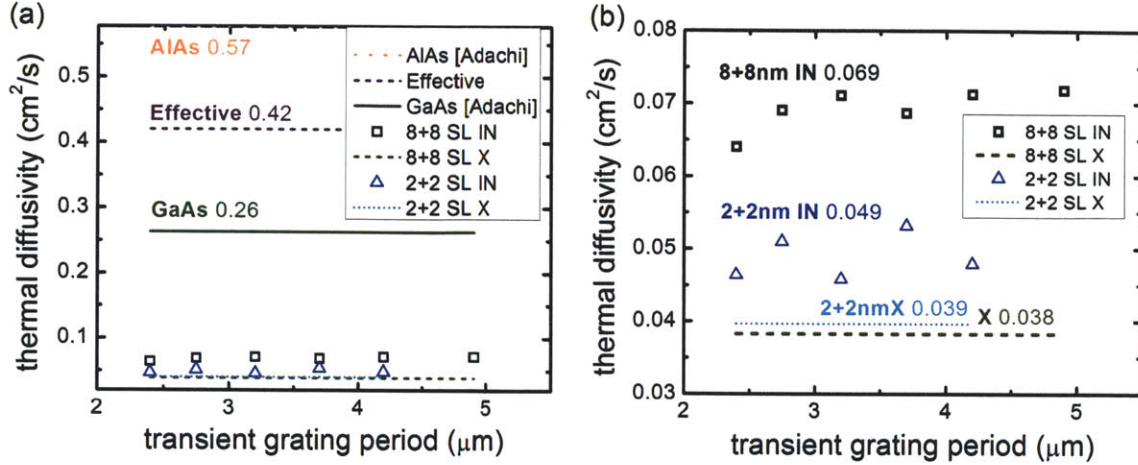


Fig. 4.11 Open squares and triangles are in-plane diffusivities as a function of transient grating period. The dashed lines along with the in-plane values indicates cross-plane (X) diffusivity measured via TTR. (a) Comparison to average value of GaAs and AlAs indicates large reduction in SL structures. (b) In- and cross-plane diffusivities are equivalent.

For the reader's consideration in Fig. 4.12, we present a compilation of reported thermal diffusivities in equal-layer-thickness GaAs/AlAs SLs, as a function of layer thickness, including measurements of both in- and cross-plane thermal diffusivity. We include TTR cross-plane measurements of Maris and co-workers [Capinski] and ac calorimetric in-plane measurements of Yao [Yao] and Chen [Chen]. The open squares indicate the in-plane diffusivities we measured and the triangles indicate the cross-plane values. First we note that the overall trend of thermal diffusivity increasing with layer thickness is consistent for both in- and cross-plane, the increase is approximately linear on a plot with a linear abscissa. We also point out that our newly recorded values are similar to previously reported values. Comparing all the data, there are only slight differences in cross- and in-plane diffusivities where layer thicknesses coincide. Differences in the reported values could be explained by differences in sample quality, and we also note that the measurements of [Yao] are more prone to error and inconsistencies. Given these considerations, we see that our data are consistent with reported GaAs/AlAs

thermal diffusivities and that the anisotropy of such SL structures may not be as pronounced as in other SLs.

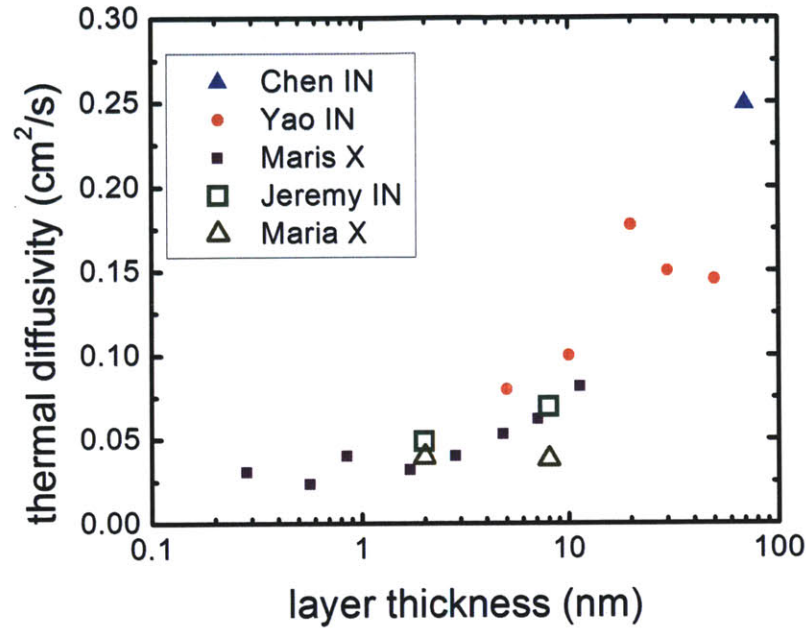


Fig. 4.12 Comparison of reported in- and cross-plane thermal diffusivities for equal layer thickness GaAs/AlAs SLs as a function of layer thickness. Linear increase in diffusivity with layer thickness is observed when plotted with linear abscissa.

In a simplified picture, we argued that there should be strong anisotropy. But the real problem is fairly complex, as seems to be the case in GaAs/AlAs SLs. The in-plane and cross-plane thermal transport are not made up of phonons just traveling in one single direction each, but are really integrated over all directions, taking wavevector components along the direction of interest. There are also the important issues of the acoustic impedance mismatch ratio, which is much smaller for AlAs and GaAs than for Si and Ge ( $Z_1/Z_2 = 0.84$  vs.  $0.69$  respectively) and the fact that mode conversion and diffuse scattering at interfaces redistribute phonons in different branches and directions, thus coupling the in- and cross-plane transport.

Attempts at modeling these effects have been made with significant simplifications [Chen98,Hyldgaard,Hepplestone], but due to complexities, a rigorous theory is still forthcoming, thus underscoring the importance of such anisotropic measurements



on identical samples. Furthermore, in order to achieve a high degree of phonon scattering in all directions, designer 2- and 3-D nanostructured materials can be fabricated. In reality, an ideal, low thermal conductivity material will probably have nano-crystalline grains of many shapes and sizes such as those produced by the Z. F. Ren group at Boston College [Poudel], but in order to learn more about the fundamentals of thermal transport across interfaces, well defined superlattice samples are favorable starting points. Further measurements exploring the thermal transport properties of selected superlattice structures at different temperatures are currently under way.

#### **4.8 TG discussion and outlook**

The presented methodology removes ambiguities in the analysis of transient thermal grating responses and lays the foundation for the use of the heterodyned transient grating method for thermal transport measurements in opaque materials. We have shown that ascribing the TG signal to the surface displacement alone may lead to significant errors in the analysis. By employing phase-controlled heterodyne detection, we have isolated the thermorefectance component of the TG response and performed analysis with a two-dimensional thermal diffusion model to extract the thermal diffusivity of thin film PbTe and GaAs/AlAs SL samples.

We have taken advantage of a number of aspects of the technique and we can envision other benefits that could be utilized in future experiments. Unlike many transient thermorefectance measurements [Paddock,Capinski,Schmidt,Stevens], the method does not require a metal transducer film deposited on the sample surface. Another benefit of TG measurements is the ability to impart a well-defined length scale of the thermal transport (effectively one half of the transient grating period  $L$ ), which can be varied typically in the range 0.5-100  $\mu\text{m}$ . Measurements at small periods are useful for characterization of thin films and on small areas (just a few TG fringes need to fit in an area to enable a measurement), while the ability to vary  $L$  could be exploited to determine depth dependent thermal properties [Käding,Harata]. On the other hand, the ability to control the thermal transport

length scale opens prospects for studying non-equilibrium thermal transport at small distances. Measurable deviations from the Fourier law at room temperature are expected to occur, for example in gold at  $L \sim 1 \mu\text{m}$  [Maznev], and the same is shown to be true in Chapter 5 for materials with high lattice thermal conductivity: Si and GaAs. Reducing the transient grating period by using shorter optical wavelengths, possibly combined with other approaches, such as immersion lens or near-field imaging, will open the avenue for studying thermal transport at the nanoscale. The use of extreme ultraviolet (EUV) light to probe photothermal and photoacoustic responses has already been demonstrated [Siemens]; using EUV to excite transient gratings would be a great advance for nanometer range measurements albeit implementing phase-controlled heterodyne detection with EUV will be a challenge. We anticipate interesting developments ahead, both experimentally and in applications to material science and thermal transport physics.





# Chapter 5

## From diffusive to ballistic thermal transport

### 5.1 Introduction

Thermal transport at microscopic distances is an area of active research [Cahill03] largely stimulated by practical needs such as thermal management of microelectronic devices [Pop], but also posing a number of fundamental physical chemistry problems. As briefly discussed in Chapter 3, the relationship between the phonon mean free path (MFP) and a characteristic length scale plays the key role in analyzing thermal transport at small distances. At cryogenic temperatures, ballistic phonon propagation over macroscopic distances has been studied extensively [Wolfe]. At room temperature, on the other hand, the majority of phonons have MFPs in the nanometer range. The frequently cited “textbook value” of the phonon MFP in Si at 273K based on a simple kinetic theory [Blakemore, Burns] is 43 nm, with even shorter MFPs listed for most other materials. Thus one would not normally expect deviations from the classical thermal diffusion model at distances significantly exceeding 40 nm.

However, a growing body of experimental and theoretical studies has been indicating that the effective MFP of heat-carrying phonons in Si is significantly larger than the number cited above. Indeed, low-frequency phonons with large MFPs are expected to contribute more to thermal conductivity than they do to specific heat. Thus the numbers 260-300 nm have been suggested for the analysis of thermal transport in thin films [Ju] and superlattices [Chen98]. Still, it has been widely held that at the  $\sim 1 \mu\text{m}$  scale room temperature heat transport in Si is consistent with simple diffusion theory [Cahill].

On the experimental side, deviations from diffusive transport at room temperature have been reported in sapphire [Siemens] and semiconductor alloys [Koh, Highland] at length scales 100-500 nm. Measurements in Si indicated non-diffusive transport

at  $\sim 1 \mu\text{m}$  scale at temperatures 100-200 K [Sverdrup] but at room temperature no deviations from the classical diffusion model have been detected [Koh, Sverdrup]. Measuring non-diffusive thermal transport at small distances in a configuration that can be quantitatively compared to theoretical models has been a challenge for experimentalists. For example, the model of heat transport through a slab of material between two black-body walls favored by theoreticians [Majumdar, Mittal, Narumanchi] is all but impossible to realize in experiment. Just to mention one difficulty, any real interface between two materials involves thermal boundary resistance, which by itself presents a long-standing problem in nanoscale thermal transport [Cahill, Swartz]. In order to be persuasive and enable theoretical analysis beyond the diffusion model, an experiment should preferably (i) avoid interfaces, (ii) ensure one dimensional thermal transport, and (iii) clearly define the distance of the heat transfer and provide a way to vary this distance in a controllable manner.

A method satisfying the above requirements has in fact been well known in the transient thermal grating technique described in this thesis. In addition to meeting the above requirements, this method yields a spatially sinusoidal temperature profile facilitating theoretical treatment. However, application of transient gratings to studying thermal transport on the nanoscale requires optical wavelengths in the UV or deep UV range, which entails experimental challenges [Cucini]. On the other hand, measurements on the  $\sim 1 \mu\text{m}$  scale pose no difficulty and can be done with conventional laser sources in the visible range. In this chapter, we present transient thermal grating measurements of in-plane heat transport in free standing silicon membranes as well as bulk GaAs. By varying the grating period we are able to directly measure the effect of the heat transfer distance on thermal transport.

## **5.2 Si membrane fabrication**

In order to ensure one-dimensional thermal transport in the sample while utilizing above-band-gap excitation for optical heating, the penetration depth of the pump and probe wavelengths needed to be longer than the sample size. Even though indirect gap silicon (Si) has a relatively long  $\sim 1 \mu\text{m}$  penetration depth at 515 and

532 nm wavelengths, it is still too short to use bulk Si wafers, thus necessitating the use of thin free-standing membranes. Free-standing Si membranes were fabricated by backside etching of silicon on insulator (SOI) wafers<sup>1</sup>. In this process, the underlying Si substrate and buried oxide layer are removed through a combination of dry and wet etching techniques to leave a top layer of suspended silicon (see Fig. 5.2). As the process used on the current samples is not currently in the literature, we present it here.

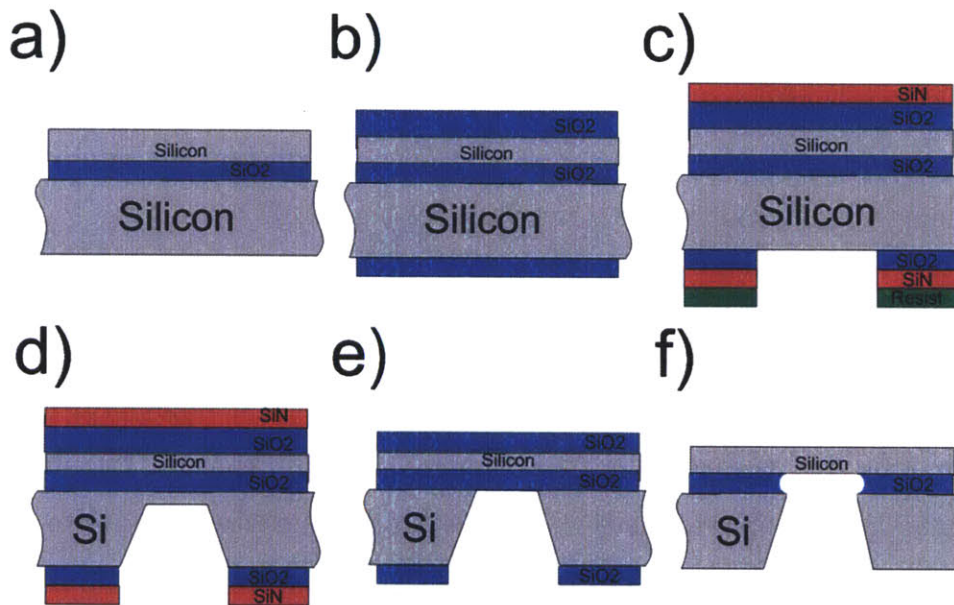


Fig. 5.2. Process flow for the fabrication of free-standing Si membranes (a) Original SOI wafer (b) Oxidation process to reduce thickness of Si layer (c) Deposition of  $\text{Si}_3\text{N}_4$ , photolithography of the etching window, including spin-coating, exposure, and development of the resist layer, and RIE of the  $\text{Si}_3\text{N}_4$  and  $\text{SiO}_2$  layers (d) Wet etching of the Si substrate using KOH, until approximately  $1\ \mu\text{m}$  of Si remains (e) Finishing of the etching of the substrate with TMAH, followed by removal of the  $\text{Si}_3\text{N}_4$  by RIE (f) Final wet etching using HF to remove the top protective oxide and the buried oxide layers, releasing the free-standing Si membrane.

The initial SOI wafers were  $625\ \mu\text{m}$  thick in total, with a top Si layer thickness of  $\sim 1.5\ \mu\text{m}$  and a  $\sim 1\ \mu\text{m}$  buried oxide layer. The target thickness of the top Si layer was achieved through oxidation of the wafer; as the thermal oxide incorporates silicon during growth, the thickness of the top Si layer is reduced. For every unit thickness

<sup>1</sup> Si membranes were fabricated by J. Cuffe and T. Kehoe in C. Sotomayor Torres' group at ICN in Barcelona.



of Si consumed, 2.27 unit thickness of oxide is grown. The oxidation was performed at a temperature of 1100 °C in an atmosphere of water vapor in two steps to achieve better control over the growth process, due to the large initial thickness of the top Si layer. Oxidation was continued until approximately 400 nm of Si remained on the top layer, and the thermal oxide was left as a protective layer as illustrated in Fig 5.2.b until the final stage of the process.

A further silicon nitride ( $\text{Si}_3\text{N}_4$ ) layer was deposited to act as a mask during the subsequent wet etching of the Si substrate and the free-standing areas of the membranes were determined through photolithography on the backside of the wafer, involving spin-coating of a photoresist, exposure, and development. The remaining photoresist was then used as a mask for Reactive Ion Etching (RIE) to open etching windows in the  $\text{Si}_3\text{N}_4$  and  $\text{SiO}_2$  (see Fig 5.2.c).

A wet etching process with potassium hydroxide (KOH) and tetramethylammonium hydroxide (TMAH) was used to remove the Si substrate. The selectivity of TMAH is better when using a  $\text{Si}_3\text{N}_4$  or  $\text{SiO}_2$  mask for the etching of Si, though the cost is higher, and the etch rate is slower. The layer of  $\text{Si}_3\text{N}_4$  was deposited to improve the etch selectivity compared to the  $\text{SiO}_2$ , and the Si substrate was etched with KOH until approximately 1  $\mu\text{m}$  of Si substrate remained (Fig. 5.2.d). The etching of the substrate was finished with TMAH, and the  $\text{Si}_3\text{N}_4$  was then removed by RIE. (Fig. 5.2.e). KOH etches preferentially in the  $\langle 100 \rangle$  direction with an etching angle of 54.7 degrees, thus the areas of the membranes are substantially smaller than the original patterns on the backside of the wafer. The reduction in length of one side can be calculated approximately by  $x_f = x_i - 2d_{\text{sub}}/\tan(54.7)$ , where  $d_{\text{sub}}$  is the thickness of the Si substrate,  $x_i$  is the initial length on the backside of the wafer, and  $x_f$  is the final length on the topside of the wafer. This relaxes the resolution requirements for the photolithography, and the photolithography masks were produced from disposable acetate in place of quartz, offering the advantage of cheap custom masks.

After the wet etching process of the Si substrate, the top, bottom, and buried oxides were removed by a wet etch of Hydrofluoric acid (HF) to release the free standing Si membranes (Fig. 5.2.f). Measurements were conducted on two membranes with  $400 \times 400 \mu\text{m}^2$  free-standing area and thicknesses of 392 and 390 nm, determined by optical reflectometry.

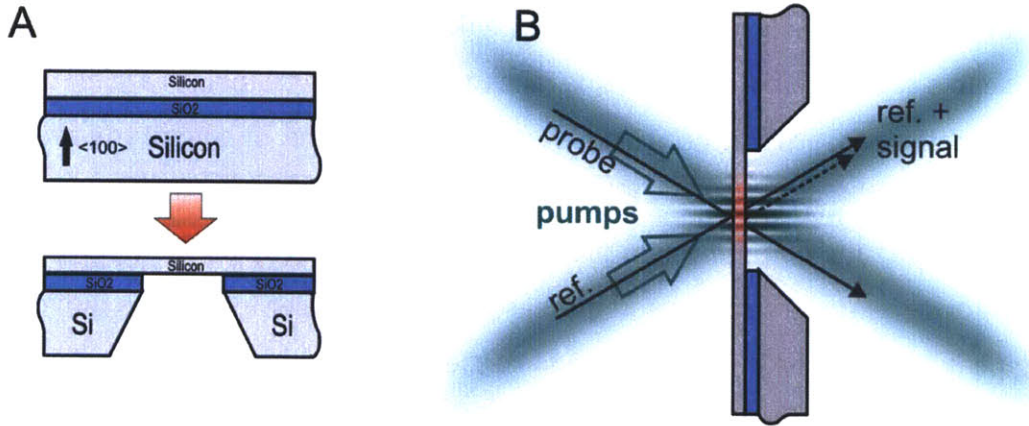


Fig. 5.3 (a) Schematic illustration of the backside etching process for the fabrication of free-standing Si membranes from SOI wafers. (b) Pump beams are focused and crossed in the silicon membrane, generating the transient thermal grating. Diffracted probe light is combined with a reference beam and directed to a fast detector.

### 5.3 Experiments on Si membranes

515 nm excitation laser pulses derived from the frequency-doubled output of the amplified Yb:KGW system were focused to a  $300 \mu\text{m}$   $1/e$  beam radius and crossed in the Si membrane with external angle  $\theta_e$  as depicted in Fig. 5.3.b. Optical interference and spatially periodic optical absorption in the silicon membrane led to excitation of hot carriers, which promptly transferred energy to the lattice and relaxed to the conduction band edge [Goldman, Othonos]. Energy was deposited with a sinusoidal intensity profile resulting in a transient thermal “grating” with period  $L$  and wavevector magnitude  $q$ ; excited carriers and heat subsequently diffused from grating peak to null parallel to the surface. Temperature and excited carriers induced changes in the complex transmittance, giving rise to time-dependent diffraction of a continuous wave probe beam ( $\lambda_p = 532 \text{ nm}$ ,  $150 \mu\text{m}$  beam radius at the sample). We used optical heterodyne detection as described in

Chapter 2. Heterodyne detection not only increases the signal level but also yields a signal linear with respect to material response, simplifying the interpretation and analysis of the data [Maznev].

Data were collected at  $\sim 15$  transient grating periods ranging from 2.4 to 25  $\mu\text{m}$  in the two silicon membranes. Fig. 5.4.a shows traces collected from the 392 nm membrane with transient grating periods from 3.2 to 18  $\mu\text{m}$ . A complete waveform shown in the inset reveals a sharp negative peak due to electronic excitation, which gives rise to a carrier population grating. Fortunately, the ambipolar carrier diffusion coefficient in Si [Linnros,Li,Zhang] is about an order of magnitude greater than the thermal diffusivity. Thus electronic and thermal transport are well separated in the time domain. From the traces in Fig. 5.4.a, we can see that the signal decay is slower as the grating period increases; it takes longer for heat to move from grating peak to null. The initial rise due to carrier transport is also slower for larger grating periods, but always far faster than the thermal transport.

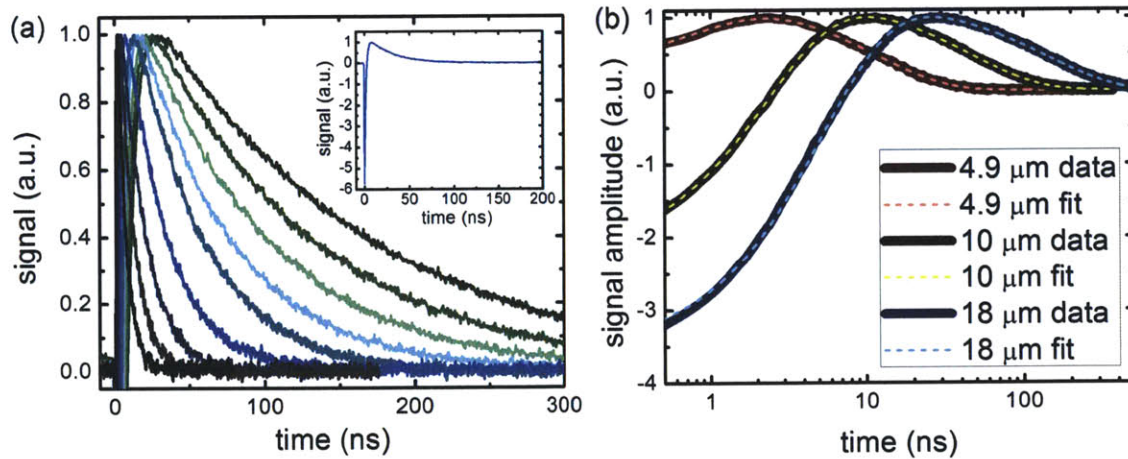


Fig. 5.4. (a) Experimentally measured, normalized thermal decay traces in a Si membrane for transient grating periods ranging from 3.2 to 18  $\mu\text{m}$ . The inset shows the complete trace for the 7.5  $\mu\text{m}$  period. (b) Full traces of 4.9, 10, and 18  $\mu\text{m}$  grating periods on logarithmic time scale with accompanying bi-exponential fits (dashed lines).

As outlined in Chapter 3, the thermal grating decays exponentially according to the diffusion equation,

$$T \propto \exp(-\gamma t) , \quad (5.1)$$



where the thermal decay rate  $\gamma$  is simply given by

$$\gamma = \alpha q^2, \quad (5.2)$$

where  $\alpha$  is the thermal diffusivity expressed in terms of the thermal conductivity  $\lambda$ , density  $\rho$ , and heat capacity  $C$  as  $\alpha = k/\rho C$ .

To account for the electronic response, which follows a similar diffusion equation [Linnros], we fit the signal to a bi-exponential form; good agreement at all times is seen in Fig. 5.4.b for three representative grating periods, thus indicating that the thermal decay remains exponential. However, the decay rate deviates from the expected  $q^2$  dependence as can be seen in Fig. 5.5.a. This departure from diffusive behavior is even more apparent in Fig. 5.5.b where we have plotted the thermal diffusivity, obtained from the measured thermal decay rate using Eq. 5.3, as a function of the grating period for the two silicon membranes.

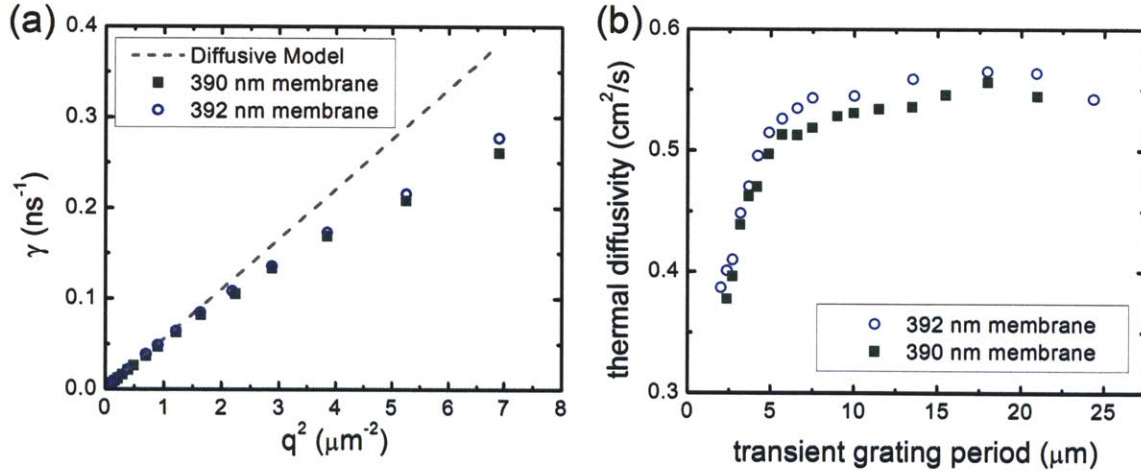


Fig. 5.5 (a) Thermal decay rate versus  $q^2$  showing the departure from diffusive behavior (dashed line). The dashed line was obtained by fitting the low-wavevector data in the range 15-25  $\mu\text{m}$ . (b) The scaled thermal conductivity determined at different transient grating periods compared with theory. (b) The theoretical scaled thermal conductivity as a function of transient grating period for different membrane thicknesses calculated using Eqs. 5.10 and 5.11 with differential thermal conductivity values from [Henry].

At large grating periods, the measured thermal diffusivity approaches a constant value, which is still significantly smaller than the bulk diffusivity of  $0.89 \text{ cm}^2/\text{s}$ . It is well known that in-plane thermal transport of thin membranes is reduced due to scattering of phonons at the boundaries [Ju, Majumdar, Narumanchi]. However, as long as the diffusion model is valid, the thermal grating decay rate should vary as  $q^2$ ,

and the measured thermal diffusivity value should remain independent of the grating period. We observe a significant further reduction in measured thermal diffusivity as the grating period is reduced below about 10  $\mu\text{m}$ , indicating a clear departure from purely diffusive thermal transport. We note that measurements very similar to the ones described here have been in fact reported [Schmoltz]; however, the shortest grating period was about twice that in the current work, which, together with a large uncertainty in the data, prevented detection of non-diffusive transport.

#### 5.4 Transient thermal grating decay in the non-diffusive regime

The fact that the crossover to the ballistic transport regime for part of the phonon spectrum slows down thermal transport compared to the predictions of the diffusion model has been well appreciated [Koh,Sverdrup,Majumdar]. In the relaxation time approximation [Henry,Ward], thermal conductivity is given by the integral over the phonon spectrum,

$$k = \frac{1}{3} \int_0^{\omega_{\max}} C_{\omega} v \Lambda d\omega , \quad (5.3)$$

where  $C_{\omega}$  is the differential frequency-dependent specific heat,  $v$  is the phonon group velocity,  $\Lambda$  is the frequency-dependent MFP, and the summation over all phonon branches is implied. According to Eq. 5.3, the contribution of phonons at a given frequency to the heat flux is given by

$$Q_{\omega} = \frac{1}{3} C_{\omega} v \Lambda \frac{\Delta T}{l} , \quad (5.4)$$

where  $l$  is the distance between the heat source and the heat sink and  $\Delta T$  is the temperature difference. According to Eq. 5.4, the heat flux increases indefinitely with increasing MFP, which cannot be true when the MFP exceeds the heat transfer distance; obviously, the heat flux cannot exceed the black body radiation limit,

$$Q_{\omega BB} = \frac{1}{4} C_{\omega} v \Delta T . \quad (5.5)$$

Thus the contribution of ballistic phonons with  $\Lambda \gg l$  to thermal transport will be suppressed *at least* by a factor of  $3/4(l/\Lambda)$  compared to the predictions of the

diffusion model. In the simplest model [Koh] the contribution of all phonons with  $\Lambda > l$  is simply disregarded, while for all phonons with  $\Lambda < l$  the diffusion model is assumed to hold. In this case the “effective” thermal conductivity is found by simply cutting off the low frequency part of the integral in Eq. 5.3,

$$k_{eff} = \frac{1}{3} \int_{\omega_0}^{\omega_{max}} C_{\omega} v \Lambda d\omega, \quad (5.6)$$

where  $\Lambda(\omega_0) = l$ .

The simplicity of the transient grating geometry allowed us to develop a more rigorous theory based on the Boltzmann transport equation for phonons with MFP on the order of or larger than  $l = L/2$  in combination with the diffusion equation for the “thermal reservoir” of high frequency phonons with  $\Lambda \ll l$  [Maznev11b]. We found that the grating decay remains exponential, and the decay rate can be obtained by replacing thermal conductivity in Eq. 5.3 by the effective conductivity,

$$k_{eff} = \frac{1}{3} \int_0^{\omega_{max}} A C_{\omega} v \Lambda d\omega$$

$$A(q\Lambda) = \frac{3}{q^2 \Lambda^2} \left( 1 - \frac{\arctan(q\Lambda)}{q\Lambda} \right), \quad (5.7)$$

where the “correction factor”  $A$  becomes unity in the diffusive limit  $q\Lambda \ll 1$  and falls off as  $(q\Lambda)^{-2}$  in the ballistic limit  $q\Lambda \gg 1$ . Unlike the simple “cut-off” model, Eq. 5.7 describes a smooth transition between diffusive and ballistic limits as plotted in Fig. 5.6. The contribution of ballistic phonons to thermal transport is suppressed even more than according to an estimate based on black body radiation limit. This is because in the transient grating experiment the heat transport does not occur between black bodies; our heat “sources” and “sinks”, i.e. maxima and minima of the thermal grating, become almost transparent for ballistic phonons in the limit  $q\Lambda \gg 1$ , which accounts for an additional factor of  $\sim (q\Lambda)^{-1}$  in the ballistic phonon contribution to the heat flux.

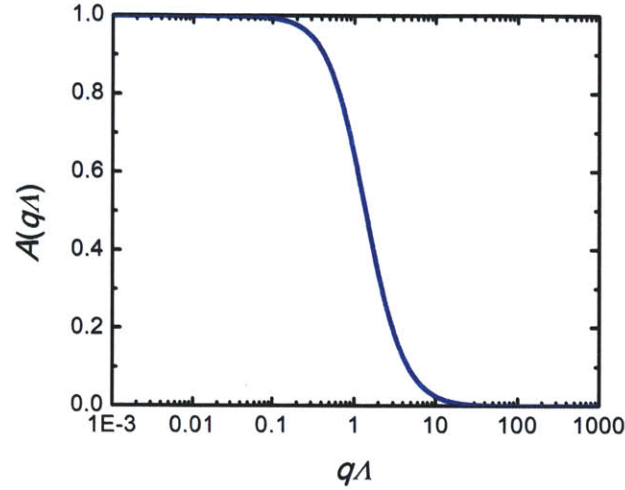


Fig. 5.6 Transient grating thermal conductivity correction factor  $A$  from Eq. 5.7 showing transition from diffusive ( $A=1$ ) to ballistic ( $A=0$ ) behavior for a particular phonon mean free path  $\Lambda$  and transient grating period  $q$ .

To get a more quantitative view of how the ballistic phonon contribution to the thermal grating decay rate is modified from the long-grating-period, diffusive limit, we show in Table 5.1 how much the contribution of a phonon of particular MFP to the TG signal decay is reduced for a given transient grating period.

Table 5.1. Reduction in contribution of phonons to thermal grating decay relative to the diffusive model according to correction factor  $A$  in Eq. 5.7.

transient grating period $L$ ( $\mu\text{m}$ )	bulk MFP $\Lambda$ ( $\mu\text{m}$ )	relative contribution
10	10	6 %
	5	18 %
	1	81 %
	0.5	95 %
	0.1	100 %
5	10	2 %
	5	6 %
	1	54 %
	0.5	81 %
	0.1	99 %
1	10	0.1 %
	5	0.3 %
	1	6 %
	0.5	18 %
	0.1	81 %



Eq. 5.7 solves the problem of finding the thermal grating decay rate provided that phonon density of states, group velocities and relaxation times for all phonon branches are known. For Si at room temperature, these quantities have been calculated from first principles [Henry, Brodido, Ward]. Still, performing calculations according to Eq. 5.7 would be a tedious task. Fortunately, we can take advantage of the calculation of the thermal conductivity accumulation vs. MFP [Henry, Ward],

$$k_{tot} = \int_0^{\infty} k_{\Lambda} d\Lambda . \quad (5.8)$$

We find the effective thermal conductivity by multiplying the integrand by the correction factor,

$$k_{eff} = \int_0^{\infty} A(q\Lambda) k_{\Lambda} d\Lambda . \quad (5.9)$$

It is instructive to plot  $k_{eff}(q)$ , or equivalently  $k_{eff}(L)$ , to see how reducing the TG period  $L$  reduces the effective thermal transport measured; the result of this calculation for bulk Si is shown in Fig. 5.7.a. Effective conductivity approaches the bulk value at large grating periods and drops down at small periods. The calculation is valid under the assumption of [Maznev11b] that diffuse phonons with  $\Lambda \ll L/2$  account for most of the specific heat, which holds well at  $L > 1 \mu\text{m}$ . Below we discuss how the membrane thickness can be accounted for.

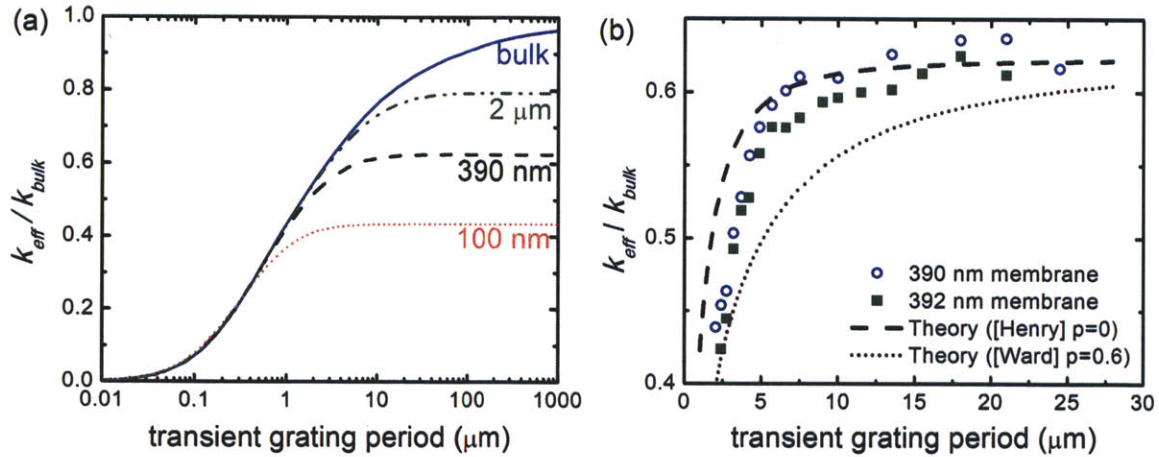


Fig. 5.7 (a) The theoretical scaled thermal conductivity as a function of transient grating period for different membrane thicknesses calculated using Eq. 5.11 with differential thermal conductivity values from [Henry]. (b) The scaled thermal conductivity determined at different transient grating periods compared with theory.

## 5.5 Si membrane comparison to theory

In the Si membrane, we should account for the reduction of MFP caused by boundary scattering. In-plane phonon transport in thin films has been studied extensively [Ju, Majumdar, Narumanchi, Liu, Turney]. The theoretical foundation has been laid by Fuchs [Fuchs] and Sondheimer [Sondheimer] who derived the expression for the effective MFP (originally for electrons) reduced by surface scattering:

$$\Lambda' = \Lambda F_p \left( \frac{d}{\Lambda} \right) \quad (5.10)$$

$$F_p(\chi) = 1 - \frac{3}{2\chi} (1-p) \int_1^\infty \left( \frac{1}{t^3} - \frac{1}{t^5} \right) \frac{1 - e^{-\chi t}}{1 - p e^{-\chi t}} dt$$

where  $d$  is the film thickness and  $p$  is the specularity parameter, with  $p = 0$  indicating completely diffuse scattering at the surfaces and  $p = 1$  indicating specular reflection. It is important to note that using the specularity parameter as a free parameter introduces a measure of arbitrariness in the data analysis [Chen05]; moreover, the commonly used model (Eq. 5.10) with a constant “specularity parameter” independent of both frequency and incidence angle [Sondheimer] is rather unphysical. Most studies of thermal conductivity in thin films use the “diffuse scattering” model ( $p = 0$ ), with satisfactory results [Ju, Liu, Turney]. Still, the observed small systematic difference between the data from the two samples seen in Fig. 5.7.b invites a conjecture that the scattering may be not totally diffuse in which case variations in the surface roughness might cause sample-to-sample differences in the measurements.

Table 5.2. Reduction in contribution of phonons to thermal transport in membrane relative to bulk material according to correction factor  $F_p$  in Eq. 5.11 with  $p=0$ .

membrane thickness	bulk MFP ( $\mu\text{m}$ )	relative contribution
390 nm	10	11 %
	5	18 %
	1	46 %
	0.5	63 %
	0.1	90 %

In Table 5.2 we show the relative reduction of the contribution of a phonon to thermal transport in a thin membrane compared to the bulk value, calculated according to Eq. 5.10. It's interesting to note that for a 390 nm membrane, the contribution of a phonon with 1  $\mu\text{m}$  MFP is reduced from the bulk value by about the same amount as for a 5  $\mu\text{m}$  transient grating period according to Eq. 5.8 (compare Tables 5.1 & 5.2).

We account for both thermal grating and boundary scattering effects in a somewhat crude way by simply taking the MFP reduced by the boundary scattering from Eq. 5.10 and plugging it into Eq. 5.7 in order to derive a new equation

$$k_{eff} = \int_0^\infty A(q\Lambda F_p) k_\Lambda F_p d\Lambda . \quad (5.11)$$

To be rigorous, one would need to solve the non-equilibrium thermal transport problem anew with appropriate boundary conditions at the surfaces of the membrane, which would be much harder than the analysis for an unbounded medium [Maznev11b]. Fig. 5.7.a shows the calculated results for three membrane thicknesses alongside the curve for bulk Si. The behavior of the membrane curves is similar to those for bulk material, but now in the  $\Lambda \rightarrow \infty$  limit the thermal conductivity is reduced from its bulk value due to the boundary scattering. In Fig. 5.7.b, we compare the calculations for  $d=390$  nm with the experimental data. Qualitatively, calculated curves agree with experimental data. A systematic deviation between theory and experiment is seen at short grating periods when using the calculations of [Henry] and deviations at longer periods using the calculations of [Ward]. These deviations may be explained by the approximation made in combining Eqs. 5.10 and 5.11, as well as by possible uncertainties in the thermal conductivity accumulation vs. MFP calculations. It is important to note that both sets of calculations recover the correct total thermal conductivity, but obvious differences exist in the thermal conductivity MFP spectrum.

## 5.6 Experiments on bulk GaAs

One difficulty in measuring purely one-dimensional thermal transport in semiconductors is the finite penetration depth of pump and probe pulses. For a

significant amount of lattice heating, photon energies should be significantly above the band gap, which translates to a high absorption coefficient and short penetration depth. This difficulty was removed in measurements of free-standing Si membranes due to the film thickness being shorter than the relatively long penetration depth. As mentioned above, this transmission geometry ensures 1-D thermal transport and also circumvents the need to separate temperature and displacement dynamics in reflection TG measurements, as described in the preceding chapter. But if we wish to measure thermal transport in other semiconductors with shorter penetration depths than Si, it becomes increasingly difficult to perform transmission measurements. For example, at green excitation and probe wavelengths, GaAs has  $\sim 100$  nm penetration depth and PbTe is even shorter with  $\sim 15$  nm. With recent advances it is possible to fabricate free standing, ultra thin GaAs membranes [Yoon], but boundary scattering effects would be much more pronounced, obscuring the non-diffusive effects we wish to observe. The ideal situation would be the case of a weakly absorbing bulk sample, perhaps due to two-photon absorption so carriers are initially excited with enough energy to induce enough lattice heating. Then the thermal transport would be purely 1-D as with the Si membranes, but without complicating boundary scattering effects.

In the absence of this ideal situation, we have performed reflection TG measurements of thermal transport in bulk GaAs. The heat transport in this case is indeed 2-D with transport from grating peaks to nulls parallel to the surface and into the depth of the material, but as discussed in the previous chapter, the TG measurement is predominately sensitive to the in-plane transport at short transient grating periods. At such periods, we unambiguously observe non-diffusive transport effects at 295 K and 425 K in a semi-insulating GaAs wafer.

Fig. 5.8 shows the results of the GaAs measurements. In Fig. 5.8.a we see representative corrected (as described in Chapter 4) amplitude grating decay traces recorded at room temperature along with fits to Eq. 4.15 to allow extraction of the in-plane effective thermal diffusivity. The inset to Fig. 5.8.a shows similar departure from diffusive behavior as was observed in Si (see Fig. 5.5.a), where here the dashed

line was calculated using the literature GaAs diffusivity [Adachi]; the decay rate still increases with  $q^2$ , but not in a linear fashion nor as quickly as the diffusion model predicts. In Fig. 5.8.b we see that the experimentally determined effective thermal diffusivity is close to the literature reported values (the dash dotted lines) at large grating periods, but decreases as we move to shorter and shorter length scales at both 295 K and 425 K; we also observe the known decrease in thermal diffusivity of the limiting large period value with increasing temperature.

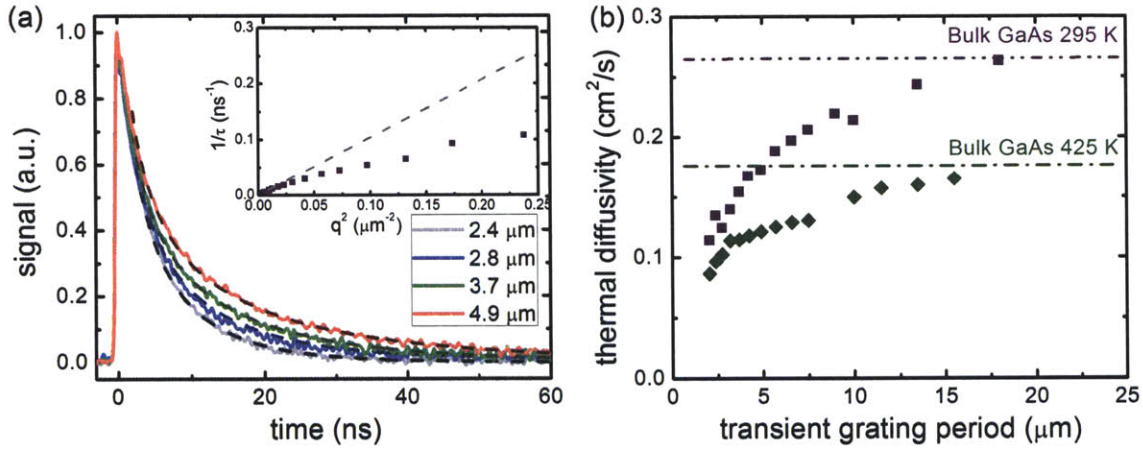


Fig. 5.8 (a) Thermal decay (amplitude grating) traces in GaAs at 295 K. The inset shows the comparison with the in-plane decay rate (see Eq. 4.15) to  $q^2$ ; the dashed line shows the diffusion model predicted behavior calculated using the literature GaAs diffusivity. (b) The measured effective thermal diffusivity as a function of transient grating period. The purple squares are for 295 K and the green diamonds are at 425 K. The labeled dash-dotted lines give the bulk GaAs diffusivity from the literature [Adachi].

## 5.7 GaAs comparison to theory

Very recent first principles calculations of the thermal conductivity accumulation in GaAs [Luo] make it possible to compare our measured bulk GaAs values to simulation without surface scattering complications. Although not shown here, these calculations produce good agreement with the bulk GaAs thermal conductivity at many temperatures. In Fig. 5.9.a we show the thermal conductivity accumulation as a function of MFP in GaAs at 300 K and 425 K; similar behavior as was observed with Si is seen here, with a good portion of the heat being carried by phonons with  $\text{MFP} > 1 \mu\text{m}$  at both temperatures. Due to the absence of surface scattering effects, we can now use the differential thermal conductivity directly in Eq. 5.9, which gives



us the dashed traces to compare with the real data. In Fig. 5.9.b we show this comparison where we have converted the measured thermal diffusivity to thermal conductivity using the literature GaAs density and heat capacity values [Adachi]. Again we see good qualitative agreement at both temperatures, but now with larger systematic deviations at short distances. We're currently unsure of the reason for discrepancies between theory and experiment, but it appears that more heat is carried in GaAs by long MFP phonons than the calculations predict. We note that the calculations are only now becoming tractable and the results should not be regarded as quantitative.

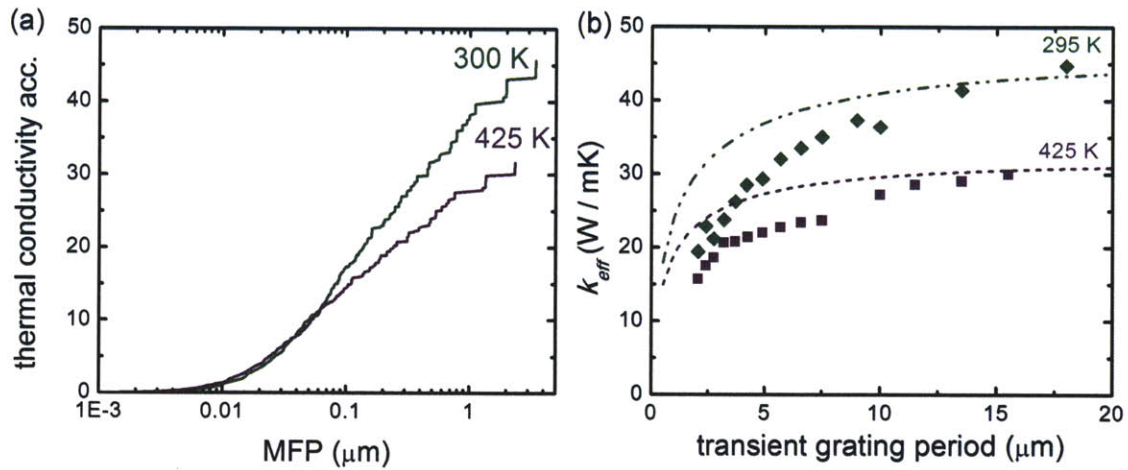


Fig. 5.9 (a) Thermal conductivity accumulation as a function of phonon MFP calculated for GaAs at 300 K and 425 K [Luo] (b) Comparison between theory and experiment for the effective GaAs thermal conductivity.

## 5.8 Conclusions and discussion

The fact that deviations from the Fourier law in phonon-mediated thermal conductivity occur at much larger distances than previously thought should change the way we think about micro-scale thermal transport. One immediate implication is that accurate measurements of thermal conductivity may be impossible on micron-sized samples. We have seen that commonly cited textbook values of a phonon MFP are of little relevance in analyzing the onset of size effects in thermal conductivity. We believe that a much more appropriate value would be that of a “median thermal conductivity MFP”  $\Lambda_m$ , such that phonons with  $\Lambda > \Lambda_m$  contribute 50% to the bulk

thermal conductivity. For Si at room temperature,  $\Lambda_m \sim 0.5 \mu\text{m}$  according to [Henry] and  $\sim 1.0 \mu\text{m}$  according to [Ward]. Moreover, if we approximate that  $\Lambda_m$  is equivalent to  $L/\pi$  when the effective conductivity we measure experimentally is half the bulk value, we report  $\Lambda_m = 1 \mu\text{m}$  for Si and  $\Lambda_m = 0.8 \mu\text{m}$  for GaAs at room temperature, and  $\Lambda_m = 0.5 \mu\text{m}$  for GaAs at 425 K. As the first principles calculations [Henry, Ward] often result in the correct total thermal conductivity but with quantitative differences in the MFP distributions as shown in Fig. 3.5, experimental measurements such as these will allow detailed refinement of the simulations. Additionally, an interesting question is whether the median MFP would be even larger for semiconductor alloys despite Rayleigh scattering caused high frequency phonon MFP reduction, which is thought to increase the relative importance of the low-frequency phonons [Koh].





# Chapter 6

## Supercooled Liquids

One of the longest standing, grand challenges of condensed matter science is a fundamental understanding of the dynamics of disordered systems [Binder]. It is not well understood how the largely uncorrelated, relatively fast relaxation of molecules in the liquid develop into slow, correlated molecular motions (many orders of magnitude slower) upon supercooling, ultimately leading to seemingly non-ergodic structural arrest at the glass transition. Such disordered, vitreous, or amorphous “glassy” materials lack the periodicity of crystals like liquids but behave mechanically like solids. From antiquity to modern times mankind has found use for amorphous solids in a number of forms and applications. Today, in addition to obvious uses of silica glass in construction and communication, amorphous semiconductors are key to many microelectronic devices, advantages of amorphous drugs have been shown in comparison to their crystalline counterparts, most plastics are amorphous solids, and even golf clubs made of metallic glasses are being manufactured [Debenedetti,Blanshard,Greer]. Furthermore, it is possible that most of the water in the Universe is in a glassy form [Jenniskens].

Upon cooling any liquid, if crystallization is avoided, a glass will be formed. Attempts have been made to describe the transition from a liquid to glass in terms of a conventional phase transition such as the entropy theory by Adams, Gibbs and DiMarzio [Gibbs,Adams], and “free” volume models like those introduced by Cohen and Turnbull [Cohen], but so far, no conventional order parameter has been defined to describe behavior near the glass transition. For example, even though the liquid-glass transition resembles a second-order phase transition in which a liquid is transformed continuously into an amorphous solid with no latent heat, the glass-liquid system exhibits no diverging correlation length, symmetry change, or obvious order parameter during the transition as is expected in a thermodynamic phase

transition [Santen].

A common feature of glass-forming liquids is their propensity for supercooling (avoiding crystallization below the freezing temperature). The transition from supercooled liquid to glass is marked by a jump in heat capacity at a particular temperature, even though a thermodynamic phase transition order parameter is absent; but this calorimetric glass transition temperature increases with the cooling rate, thus leading to some ambiguity in its definition for a particular material [Angell95].

A hallmark of supercooling is a dramatic increase in the viscosity with decreasing temperature, in fact changing over 17 orders of magnitude in a relatively small temperature window [Angell95]. This decrease in the material flow rate is closely related to a characteristic structural relaxation time. Due to such strong kinetic markers, the approach to the glass transition is most appropriately understood in a dynamical framework; but again, an obvious transition, also in the dynamics, is lacking. Therefore the kinetic glass transition temperature  $T_g$  is defined arbitrarily when the characteristic relaxation time reaches  $10^2$  or  $10^3$  seconds or the viscosity reaches  $10^{13}$  Poise. Upon further cooling, the viscosity and relaxation time continue to increase, but quickly become longer than most experimentalists will reasonably desire to watch. This dynamical nature has led some to state that a glass isn't a solid at all, but only behaves as a solid on time scales shorter than the characteristic relaxation time associated with structural rearrangement and flow.

A plethora of phenomenological theories has been developed and tested to describe the dynamical slowing down of the structural relaxation, some of which involve models connecting the elastic, short-time, properties of a material to the slow relaxation [Dyre96,Novikov,Dyre06,Torchnisky09]. For many years, the only theory derived from first-principles aimed at explaining the structural relaxation in supercooled liquids has been the Mode-Coupling Theory of the glass transition (MCT). Developed by Kawasaki [Kawasaki] and Oppenheim [Keyes] to describe seemingly anomalous liquid dynamics, it was first extended to the supercooled

regime, independently, by Das [Das86] and Gotze [Götze88]. An interesting commonality between MCT and elastic models is a connection between fast and slow dynamics. In section 6.3 we will discuss more details of MCT including experimentally testable predictions. Experiments discussed in the following chapters are aimed at testing MCT predictions and studying the structural relaxation of supercooled liquids. Despite over a century of theoretical and experimental work surrounding the subject, there is still much to learn about the transition from a supercooled liquid to the amorphous solid state.

## 6.1 Phenomenology of Supercooling

The many-order-of-magnitude increase in viscosity upon cooling is universal amongst supercooled liquids. The viscosity is connected with the characteristic structural relaxation time, and the variation with temperature is illustrated for a number of materials in Fig. 6.1 where viscosity is plotted versus inverse temperature scaled by  $T_g$  (reproduced from [Angell85]). This led Angell to classify materials as “strong”, “intermediate”, and “fragile” glasses (with no connection to the likelihood of fracture upon impact).

For strong materials such as silica glass the temperature-dependence of the viscosity,  $\eta(T)$ , is well represented by the Arrhenius law

$$\eta(T) = A \exp(E_a/k_B T), \quad (6.1)$$

where  $A$  is temperature independent material parameter,  $k_B$  is the Boltzmann constant,  $E_a$  is an activation energy associated with a structural rearrangement. Pure Arrhenius behavior is shown with the solid straight line in Fig. 6.1. Many materials also apparently deviate from the Arrhenius predicted behavior and show a strong, super-Arrhenius increase in viscosity approaching  $T_g$ . The slope of the viscosity or relaxation time approaching  $T_g$  is taken as a metric for material classification and is termed the fragility index  $m$  [Angell85]. Strong, Arrhenius behaving materials have a low  $m$  value typically in the 4-10 range, intermediate glass formers have  $m$  values ranging from 20-50, and fragile glass formers with the steepest slopes have  $m$  values ranging from 60 to over 100. So we see that for

fragile materials, the relaxation time is extremely sensitive to temperature close to  $T_g$ . Many attempt to extract fundamental information about the underlying dynamics by fitting the temperature-dependent relaxation time to certain expressions, but often expressions that fit well over a broad temperature range have many fitting parameters thus leading one to question the information content of the fit. For an overview of the numerous expressions used to fit the temperature-dependent relaxation time, see section A.1.2 of reference [Angell00].

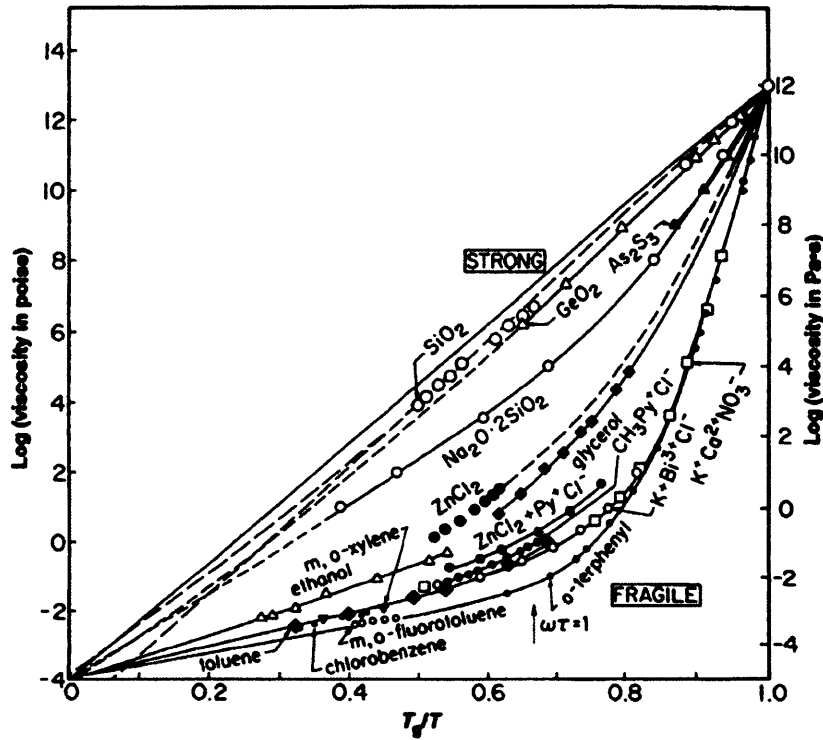


Fig. 6.1 Angell plot of the logarithm of viscosity versus inverse temperature scaled to  $T_g$  ( $T_g$  is arbitrarily defined as when the viscosity reaches  $10^{13}$  poise). The solid diagonal line illustrates Arrhenius behavior. Materials close to Arrhenius are termed “strong” while those with super-Arrhenius behavior approaching  $T_g$  are “fragile”. Figure reproduced from [Angell85].

Relaxation times are often extracted from measurements of a complex susceptibility spectrum  $\chi(\omega)$  in the frequency domain or from the decay of a relaxation function in the time domain  $F(t)$ . In measuring a change in a property  $\delta A$  of a system due to a driving field  $a_\omega$  at frequency  $\omega$  in the linear regime, the complex susceptibility  $\chi(\omega) = \chi'(\omega) + i\chi''(\omega)$  is defined according to

$$\delta A = \chi(\omega) a_\omega \quad (6.2)$$

Such frequency-domain spectra have been measured utilizing different driving fields for various techniques including dielectric spectroscopy [Lunkenheimer], mechanical and ultrasonic spectroscopy [Christensen, Mandanici, Yan87], NMR [Böhmer], and a number of other techniques (see [Götze99, Binder, Das05] for reviews of examples). The relation between the susceptibility  $\chi(\omega)$  and relaxation function  $F(t)$  is given through an intermediate function [Brodin] – the impulse response function  $\chi(t)$ , defined as the Fourier transform of the susceptibility function

$$\chi(t) = \int_{-\infty}^{\infty} \chi(\omega) e^{i\omega t} d\omega. \quad (6.3)$$

The relaxation function, which is the step response function (for a perturbation turned on at  $t=-\infty$  and turned off at  $t=0$ ), is given using the impulse response as

$$F(t) = \int_t^{\infty} \chi(t') dt'. \quad (6.4)$$

Complex dielectric susceptibility spectra measured in glycerol at different temperatures, here in terms of real frequency, are shown in Fig. 6.2 (adapted from [Schneider]); apparent are a number of spectral features common to many glass formers. The most prominent feature is what has been termed the  $\alpha$ -relaxation, the broad peak in the imaginary (loss) spectra in Fig. 6.2.b that shows strong temperature dependence and is associated with the primary structural relaxation. Due to a Kramers-Kronig relation, a connection exists between real and imaginary parts and a corresponding step is seen in the real (reactive) spectra in Fig. 6.2.a.

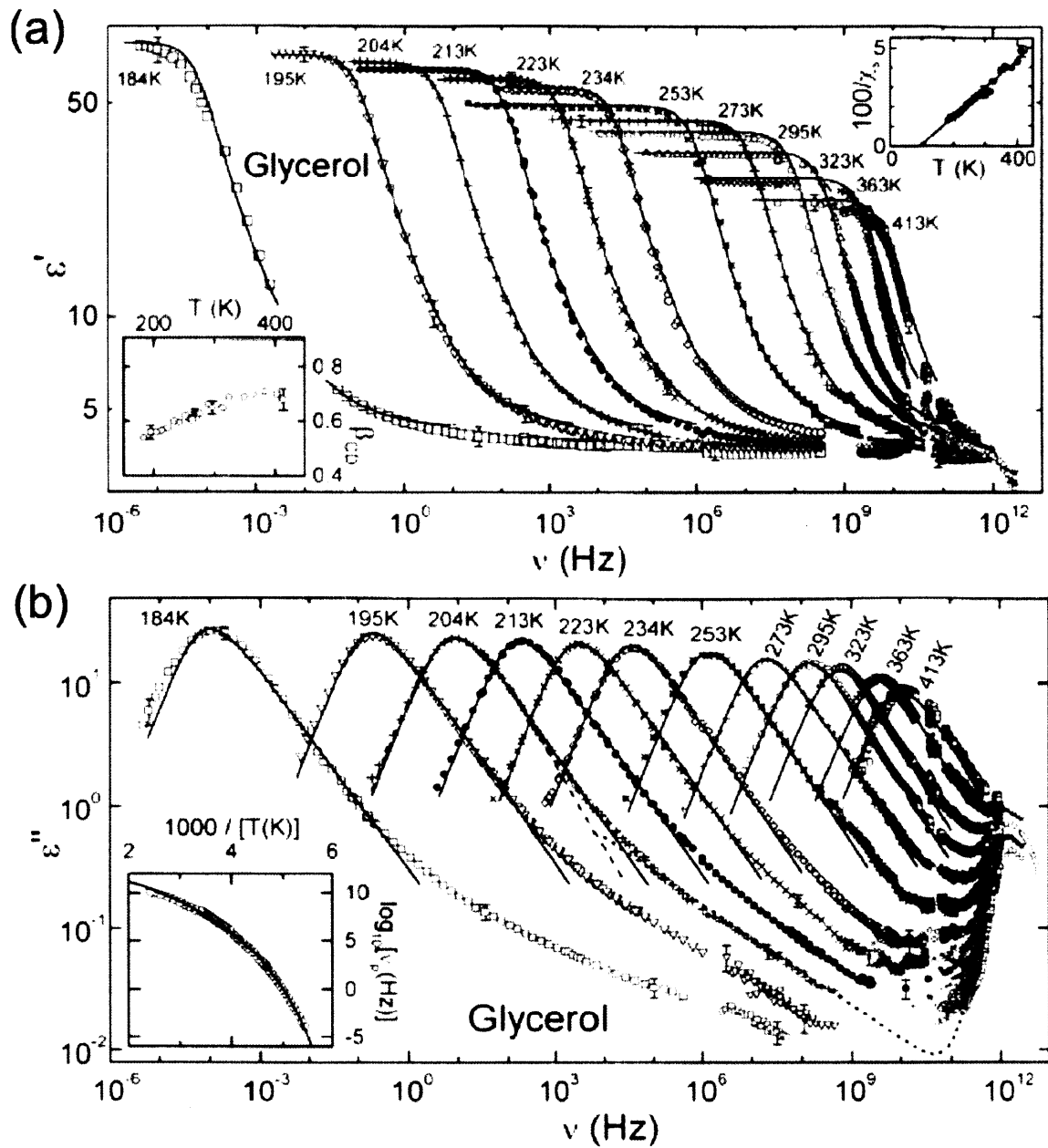


Fig. 6.2. Dielectric susceptibility (a) real (reactive) and (b) imaginary (dissipative) spectra at many temperatures for the glass former glycerol adapted from [Schneider].

A characteristic structural relaxation time is extracted often directly from the imaginary spectra alone or a combination of the pair by fitting to a variety of phenomenological functions. The behavior in the frequency domain is similar to Debye relaxation, which corresponds to a simple exponential relaxation in the time domain. A general functional form for the frequency domain is the Havriliak-Negami relaxation function (HN) [Havriliak] given by



$$\chi(\omega) = \chi_{\infty} + \frac{\chi_0 - \chi_{\infty}}{\left(1 + (i\omega\tau_{HN})^{\alpha}\right)^{\beta}}, \quad (6.5)$$

where  $\chi_0$  is the low frequency limiting value,  $\chi_{\infty}$  is the high frequency limiting value,  $\tau_{HN}$  is the characteristic relaxation time, and  $\alpha$  and  $\beta$  are spectral parameters that can vary between 0 and 1. Debye relaxation is given by  $\alpha = \beta = 1$ . An analogous time-domain function is the Kohlrausch-Williams-Watts (KWW) stretched exponential relaxation function [Kohlrausch,Williams]

$$F(t) = F_0 \exp\left[-\left(\frac{t}{\tau_{KWW}}\right)^{\beta_{KWW}}\right], \quad (6.6)$$

with  $\tau_{KWW}$  the characteristic relaxation time and  $\beta_{KWW}$  the stretching parameter which varies between 0 and 1. The frequency domain functions for Debye ( $\alpha=\beta=1$ ) and HN ( $\alpha=1$ ;  $\beta=0.5$ ) relaxation with  $\tau_{HN} = 1$  are illustrated in Fig. 6.3.a.

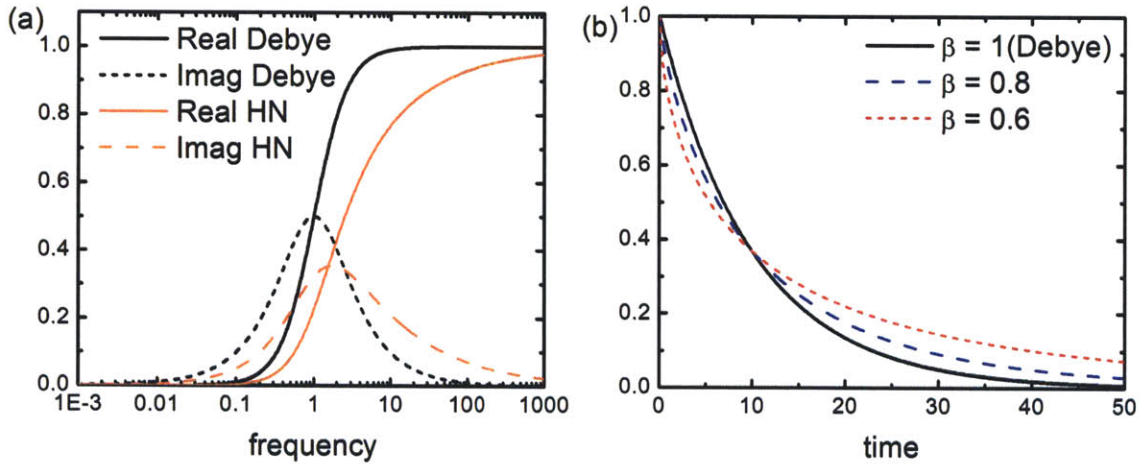


Fig. 6.3. Phenomenological relaxation functions (a) Real (solid lines) and imaginary (dashed lines) part of Debye (black) and HN (orange) with  $\alpha_{HN} = 1$  and  $\beta_{HN} = 0.5$  (b) KWW relaxation function with the stretching parameter  $\beta_{KWW} = 1$  (Debye), 0.8, and 0.6.

The Debye peak, even though narrow in comparison to the HN peak, is still somewhat broad, covering nearly two decades in frequency. The HN spectral parameters  $\alpha$  and  $\beta$  serve respectively to broaden and skew the peak. The stretched exponential function is plotted in Fig.6.3.b with  $\tau_{KWW} = 10$  and  $\beta_{KWW} = 1, 0.8, 0.6$ . We note that even though the KWW relaxation time is identical for each trace, the stretching parameter significantly alters the actual decay. A similar behavior is also

seen comparing HN to Debye relaxation in Fig. 6.3.a: even though  $\tau_{HN}$  is identical, the corresponding frequency of the peak maximum is different. The stretching of relaxation functions is often thought of in two limiting descriptions: in one case we simply have exponential relaxation events with a distribution of relaxation times and in the other we have relaxation events that are inherently non-exponential. In all likelihood, a combination of these two descriptions may be the reality [Binder].

These simple functions are mainly used to model the  $\alpha$ -relaxation, yet there are other evident features in the recorded spectra. Another prominent feature appearing in Fig. 6.2.b is a temperature-independent peak at high frequencies, also with corresponding step in Fig. 6.2.a, that the  $\alpha$ -relaxation seems to grow out of as temperature is reduced. This high frequency peak (sometimes peaks) is thought to arise from differing mechanisms ranging from the fast microscopic rearrangements associated with particle motion in “cages” of nearest neighbors (termed simply the microscopic peak or high frequency  $\beta$ -relaxation in an MCT framework) as well as an excess of oscillatory states above the Debye description (the Boson peak – a controversial subject) [Lubchenko,Taraskin,Schirmacher]. A final feature we’ll point out, especially observable for the lower temperature data, is an excess wing to the  $\alpha$ -relaxation peak occurring at intermediate frequencies. In many materials this excess wing is manifest as a separate peak called the Johari-Goldstein  $\beta$  relaxation process, often associated with segmental motion of longer chain molecules [Johari].

In order to gain a deeper understanding of the underlying physical processes than these phenomenological functions offer, the measured relaxation should be connected with an appropriate correlation function. Because our primary interest lies in understanding structural relaxation, a density space-time correlation function termed the intermediate scattering function, given by Eq. 6.7, is of premier importance.

$$F(q,t) = \frac{1}{N} \langle \delta\rho(\mathbf{q},t) \delta\rho^*(\mathbf{q},t) \rangle = \frac{1}{N} \left\langle \sum_{j=1}^N \exp[i\mathbf{q} \cdot \mathbf{r}_j(t)] \sum_{k=1}^N \exp[-i\mathbf{q} \cdot \mathbf{r}_k(t)] \right\rangle, \quad (6.7)$$

where  $N$  is the number of particles,  $\mathbf{q}$  is the wavevector,  $q$  is the wavevector

magnitude,  $\mathbf{r}_i$  is the position vector of the  $i$ th particle, and  $\delta\rho$  is the deviation from equilibrium density. For good discussions of correlation functions relevant to liquid dynamics and the glass transition, please see [Balucani,Boon,Frenkel]. It's also crucial to have a technique with enormous dynamic range, as is the case with the dielectric spectroscopy data displayed in Fig. 6.2, showing data over an unmatched 17 orders of magnitude; but dielectric spectroscopy probes primarily the orientational correlation function, not the density relaxation. Dielectric data offer clues to the structural relaxation due to rotational-translational coupling (coupling between orientational motion and collective structural relaxation), but this coupling is a rich field of study in its own right and can obscure comparison to theory.

Techniques that measure the frequency-dependent mechanical and acoustic properties are promising due to the direct coupling between sound waves and density correlations [Balucani]; the complex acoustic compliance has direct connections to the density correlation function (equivalent to the relationship between a susceptibility spectrum and the corresponding relaxation function) [Wang85]. Measurements of mechanical properties at relatively low frequencies ( $\leq$  MHz) utilizing piezo-transducer and ultrasonic techniques have been commonplace for a number of years [Christensen,Mandinici], but extending to higher frequencies has been challenging. ISS offers a clear means of generation and detection of MHz to low GHz frequency longitudinal and shear acoustic waves, and recent improvements in picosecond ultrasonic measurements in liquids have extended the range to even higher frequencies [Yan87,Yang]; indeed temperature-dependent broadband acoustic compliance spectra of the glass forming liquid tetramethyl tetraphenyl trisiloxane (DC704) have, for the first time, been constructed utilizing these different techniques [Hecksher,Torchinsky,Klieber]. Such broadband acoustic spectra offer a unique look at the high and low frequency material response with the ability to test mode-coupling-theory predictions linking fast and slow relaxation. In Chapter 8 we add additional data to frequency gaps in the reported broadband spectra [Klieber] using the nanosecond acoustic interferometry technique introduced in Chapter 2 and we test key MCT predictions.

## 6.2 Mode Coupling Theory of the glass transition

### 6.2.a Introduction

Mode coupling theory provides an intuitively appealing physical picture involving caging effects and associated retardation of collective structural relaxation. The theory of MCT is developed for a system of particles to describe the dynamics of the intermediate scattering function. In the sixties and seventies theoretical methods were developed to quantitatively describe the dynamics of simple liquids [Kawasaki]. Equations of motion for the intermediate scattering function that provided a good description of liquid dynamics at the triple point were derived using the Zwanzig-Mori projection operator formalism [Zwanzig] with mode-coupling approximations. They showed that the dynamics could be understood in terms of trapping of particles in a cage formed by their neighbors; a nonlinear feedback mechanism re-routes the energy back to the original particle, keeping it in place until collective relaxation (flow) occurs, breaking up the “cages”. MCT describes this collisional energy and momentum transfer between the central particle and the surrounding particles and later equations were simplified neglecting terms deemed irrelevant at low temperatures [Bengtzelius]. Lowering the temperature increases the density and reduces the available energy for structural rearrangement, leading to a quasi-static disordered structure (glass) for longer and longer times, emphasizing the purely dynamical nature of the liquid-glass transition. The following section outlines a few key steps and approximations in the theory originally developed by Götze and Sjögren [Bengtzelius, Leutheusser], and is given in more detail in [Binder].

### 6.2.b Mode Coupling Theory equations

Considering an isotropic system so that  $F(q,t)$  only depends on the magnitude of  $\mathbf{q}$ , the equations of motion can then be written as an integro-differential equation

$$\ddot{\Phi}(q,t) + \Omega_q^2 \Phi(q,t) + \Omega_q^2 \int_0^t [M^{reg}(q,t-t') + M(q,t-t')] \dot{\Phi}(q,t') dt' = 0 . \quad (6.8)$$

where  $\Phi(q,t)$  is the normalized intermediate scattering function,  $F(q,t)/F(q,0)$ , and the squared frequency  $\Omega_q^2$  follows directly from the short time expansion of the equations of motion and is given by

$$\Omega_q^2 = \frac{q^2 k_B T}{m S(q)}, \quad (6.9)$$

where  $S(q) \equiv F(q,0)$  is the static structure factor,  $m$  is the mass of the particles and  $k_B$  is Boltzmann's constant. The memory function has been divided into two parts with  $M^{reg}(q,t)$  representing the "regular" short time dynamics and  $M(q,t)$  responsible for the dynamics at long times of interest here. One of the central approximations in the original MCT formulation is given in the expression for  $M(q,t)$  as a bi-linear product of the correlation functions

$$M(q,t) = \frac{1}{2(2\pi)^3} \int d\mathbf{k} V^{(2)}(q,k,|\mathbf{q}-\mathbf{k}|) \Phi(k,t) \Phi(|\mathbf{q}-\mathbf{k}|,t), \quad (6.10)$$

with vertex  $V^{(2)}$  that can be calculated from the static structure factor as

$$V^{(2)}(q,k,|\mathbf{q}-\mathbf{k}|) = \frac{n}{q^2} S(q) S(k) S(|\mathbf{q}-\mathbf{k}|) \left( \frac{\mathbf{q}}{q} [\mathbf{k} c(k) + (\mathbf{q}-\mathbf{k}) c(|\mathbf{q}-\mathbf{k}|)] \right)^2. \quad (6.11)$$

Here  $n$  is the particle density and  $c(k) = n(1-1/S(q))$ . The mode-coupling equations 6.8-6.11 form a closed set of self-consistent coupled equations for  $F(q,t)$ , where the only input parameter is the static structure factor  $S(q)$  that can be measured experimentally or calculated from first principles.  $S(q)$  gives the strength of the vertex (Eq. 6.11), which in turn determines the amplitude of non-linear couplings in the product of correlation functions in the memory function in Eq. 6.10. These non-linear couplings describe the feedback mechanism that is the core of MCT. There are two main assumptions involved in the derivation of these equations, which has been termed Ideal MCT. One is that the full expressions for Eq. 6.10 and 6.11 in fact include higher order correlation functions, here approximated as a product of 2-point correlation functions. Another simplification given in the full derivation (see [Binder] for details) is an explicit substitution of an anomalous propagator for a typical one in the Zwanzig-Mori formulation. Even with the two main assumptions, the equations are still too complex for an analytical solution without making simplifications to the static structure factor [Leutheusser], but numerical solutions to the coupled equations of motion can be obtained.

Given one such simplification to the static structure factor, [Bengtzelius] calculated

the decay of the density correlator  $\Phi(q,t)$ , shown in Fig. 6.4.a, where the lines labeled A-G are simulated for decreasing temperature. As temperature is reduced, the decay of the correlator slows down and a step in the decay becomes apparent; physically this is associated with the cage trapping effect mentioned above and reproduces in the frequency domain two main peaks such as those in Fig. 6.2.b. One of the immediately visible shortcomings of Ideal MCT is that, as temperature is further decreased, a divergence in the relaxation time appears – as  $t \rightarrow \infty$  for low temperatures labeled B', D', F', the correlator never fully decays to zero. Albeit this mathematical non-ergodicity at some critical temperature  $T_c$  is not physical, it has led, in the MCT framework, to a number of testable predictions as to the decay of the density correlator.

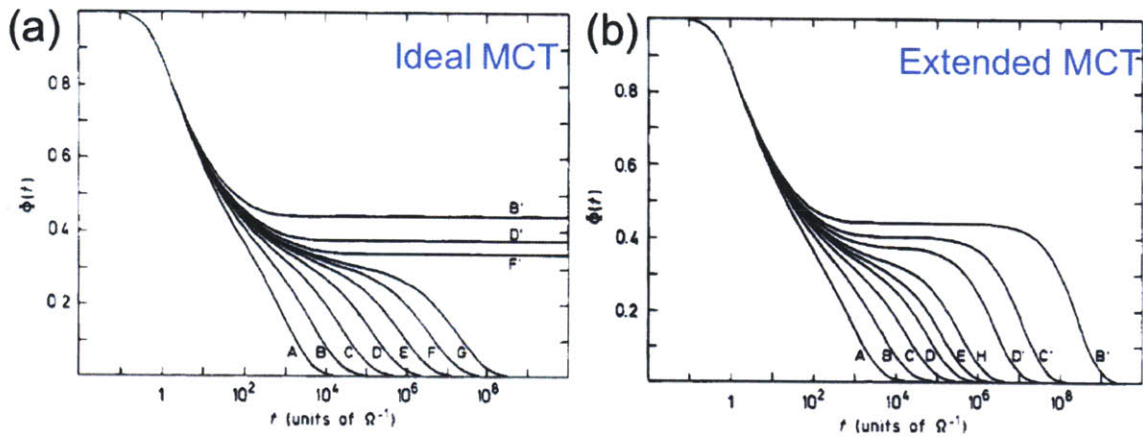


Fig. 6.4 MCT calculations of the decay of the density correlator. (a) Ideal MCT calculations for decreasing temperature (A-G, D', C', B') showing non-ergodic transition as  $T$  is lowered below  $T_c$ . (b) Due to coupling to transverse current and thermally activated hopping, ergodicity is restored at all temperatures according to Extended MCT calculations. (Plots adapted from [Bengtzelius].)

Through the years a number of improvements to the Ideal MCT have been proposed that restore ergodicity for all temperatures, resulting in what is termed Extended MCT. [Bengtzelius] added somewhat phenomenological couplings that involved shear modes and thermally assisted hopping, with the results shown in Fig. 6.4.b. The original formulation by Das and Mazenko utilizing fluctuating hydrodynamics [Das86,Das04,Das09] did not result in such unphysical non-ergodic behavior because to the coupling to shear modes restores ergodicity at all temperatures.

Other approaches have shown that this divergence results from the mathematical simplifications discussed above, and by removing these assumptions and including higher order density correlation functions, the correlator will in fact eventually decay to zero at all temperatures without coupling to other modes [Wu,Mayer]. We know that experimentally there is no divergence in viscosity or relaxation time, but understanding the connections to theory and potential influence of coupling between modes to facilitate structural rearrangement is one of the goals of modern research.

### 6.2.c Predictions of the Mode Coupling Theory

As discussed, the pertinent predictions of mode-coupling theory revolve around a critical temperature  $T_c$  at which the  $\alpha$ -relaxation time of the system diverges (we will use  $\tau_{HN}$  in the analysis in subsequent chapters). Despite the MCT extensions and improvements that suppress this divergence, some predictions of the Ideal MCT are still shown to hold near the transition temperature  $T_c$ , where now  $T_c$  is understood as a crossover to different low temperature dynamics [Das04,Mayer]. Here we outline these Ideal MCT predictions, which should hold, strictly speaking, when the separation parameter,

$$\sigma = \frac{T_c - T}{T_c}, \quad (6.12)$$

is small (often this separation parameter and related MCT predictions are given in terms of density or packing fraction as well:  $\sigma = (\Delta - \Delta_c)/\Delta_c$  where  $\Delta$  is the packing fraction).

In both Ideal and Extended MCT, as temperature decreases, the step in the correlator decay becomes longer and longer as well as higher. The non-zero level to which the correlator decays in Ideal MCT at  $T_c$  and below, as well as the plateau height above  $T_c$ , is called the non-ergodicity parameter  $f_q^c$ . Just above  $T_c$ , the MCT equations can be expanded in terms of  $\Phi(q,t) - f_q^c$  and the asymptotic analysis of this behavior yields the derivation of several MCT predictions.

The first is what we call the factorization property given by



$$\Phi(q,t) - f_q^c = h_q G(t) , \quad (6.13)$$

which predicts that the  $q$ -dependence of  $\Phi(q,t) - f_q^c$  in the asymptotic region is completely encapsulated in the amplitude  $h_q$  and the time dependence is given by the  $q$ -independent function  $G(t)$ , called the  $\beta$ -correlator. MCT solutions show that  $G(t)$  first decays as  $t^{-a}$  (the critical decay) down to the plateau termed the  $\beta$ -relaxation regime, then decreases initially from the plateau as  $-t^b$  (the Von Schweidler law) to the  $\alpha$ -relaxation regime (note that some confusion can arise because the  $a$  exponent is associated with  $\beta$ -relaxation, while the  $b$  exponent is associated with the  $\alpha$ -relaxation). The MCT connection between fast and slow dynamics mentioned previously is due to the predicted relationship between the two exponents  $a$  and  $b$  according to

$$\lambda = \frac{\Gamma^2(1-a)}{\Gamma(1-2a)} = \frac{\Gamma^2(1+b)}{\Gamma(1+2b)} , \quad (6.14)$$

where  $\Gamma$  is the gamma function. Just below  $T_c$ , it is predicted that the amplitude of the non-ergodicity parameter  $f_q$  increases as

$$f_q(T) = \begin{cases} f_q^c & (T > T_c) \\ f_q^c + h_q \sigma^{1/2} & (T < T_c) \end{cases} , \quad (6.15)$$

where  $\sigma$  is the separation parameter defined in Eq. 6.12. This predicted square-root cusp in  $f_q(T)$  has been observed experimentally to be present in several fragile glass formers [Yang95a] but absent in others that are less fragile [Paolucci].

MCT also predicts scaling laws in both the  $\alpha$ - and  $\beta$ -relaxation regimes. In the  $\alpha$ -relaxation regime, the primary structural relaxation has been shown experimentally in many materials to obey the principle of time-temperature-superposition (TTS), at least over a limited temperature range. This is perhaps most easily described in the frequency domain – the  $\alpha$ -relaxation feature merely moves to a new position without changing shape as the temperature is changed. Even without a careful analysis, we can see that this is likely the case for the glycerol dielectric data in Fig. 6.2. In terms of the phenomenological fitting functions Eqs. 6.2 & 6.3, this means that while the relaxation time is temperature dependent, if TTS is obeyed the shape/stretching parameters will be constant with temperature and all the data

could be scaled in time to overlap. In terms of MCT, this relation is given mathematically using the characteristic relaxation time  $\tau$  to scale the data with a temperature independent master function  $F_q$

$$\Phi(q, t) = F_q(t/\tau). \quad (6.16)$$

Although an analytical form for  $F_q$  is not available, numerical solutions to the MCT equations show that it fits well to the KWW relaxation function Eq. 6.6. Again we note that this prediction is expected to hold only close to  $T_c$ . As  $T_c$  is approached from above, MCT predicts that the relaxation time  $\tau$  diverges according to

$$\tau(T) = \tau_0(T - T_c)^{-\gamma}. \quad (6.17)$$

Here,  $\tau_0$  is a microscopic relaxation time and again an MCT connection exists between fast and slow dynamics given by the relation  $\gamma = 1/2a + 1/2b$ . Of all the MCT predictions, this is the most difficult to ascertain the value of  $T_c$  because such a divergence doesn't exist in real systems.

While density fluctuations, which constitute the longitudinal waves, are the natural variable of the theory, MCT suggests relationships between the various relaxing variables (e.g., density fluctuations, transverse current fluctuations, orientational fluctuations, etc.) through the so-called  $\alpha$ -scale coupling [Götze99]. This prediction states that if two variables, A and B, couple to the density fluctuations, their associated relaxation times,  $\tau_A(T) = C_A\tau(T)$  and  $\tau_B(T) = C_B\tau(T)$ , are equivalent, up to a temperature independent factor, to a universal relaxation time  $\tau(T)$ . The relationship between these relaxation times can break down and decoupling may then occur at  $T_c$ . In order to test this prediction, characteristic relaxation times associated with different correlation functions need to be compared.

As flow includes both changes in density and shearing motions, additional MCT predictions have been presented concerning the transverse current fluctuations. One such prediction is a power-law divergence of an upper bound length scale for shear wave propagation derived using MCT calculations with the static structure factor for hard spheres in a Percus-Yevick approximation [Ahluwalia]. While such an upper bound has been established in the literature [Balucani] in terms of a

wavelength at which the corresponding shear acoustic frequency goes to zero (indeed one distinction between liquids and solids is that a solid can support transverse acoustic waves at arbitrarily long wavelengths while liquids cannot), this particular temperature dependence is unique to MCT and, to our knowledge, has not been investigated experimentally.

To review further predictions surrounding the density correlation function, in the  $\beta$ -relaxation regime the so-called  $\beta$ -correlator  $G(t)$  obeys the scaling laws

$$G(t) = \begin{cases} \sqrt{|\sigma|} g_{-}(t/t_{\sigma}) & \text{for } \sigma < 0 \\ \sqrt{|\sigma|} g_{+}(t/t_{\sigma}) & \text{for } \sigma > 0 \end{cases} . \quad (6.18)$$

The scaling time  $t_{\sigma}$  is given by

$$t_{\sigma} = t_0 / \sqrt{|\sigma|^a} , \quad (6.19)$$

where  $t_0$  is the microscopic time scale  $t_0 = \Omega_0^{-1}$ . Both master functions  $g_{\pm}(t/t_{\sigma})$  follow the critical decay law ( $t^{-a}$ ) for short times,  $g_{-}(t/t_{\sigma})$  follows the von Schweidler law ( $-t^b$ ) for longer times, and  $g_{+}(t/t_{\sigma})$  for longer times has a constant value of  $(1-\lambda)^{-1/2}$  (with  $\lambda$  defined in Eq. 6.14).

#### 6.2.d The susceptibility spectrum

The predicted scaling laws have corresponding frequency domain forms that could as well be tested via measurements of the susceptibility spectrum. As we have already discussed  $\alpha$ -relaxation scaling, we will conclude with a discussion of scaling in the  $\beta$ -relaxation regime. The imaginary susceptibility  $\chi''(\omega)$  should scale as

$$\chi''(\omega) = h_q \sqrt{|\sigma|} X''(\omega t_{\sigma}) , \quad (6.20)$$

where  $X''$  is the susceptibility master function. The critical and von Schweidler decays mentioned above are expressed power laws predicted to be

$$\chi''(\omega) \propto \omega^a \quad (\omega_{\sigma} \ll \omega \ll \Omega_q) \quad (6.21)$$

on the low frequency side of the high frequency peak,

$$\chi''(\omega) \propto \omega^{-b} \quad (\omega_{\alpha} \ll \omega \ll \omega_{\sigma}) \quad (6.22)$$

on the high frequency side of the  $\alpha$ -relaxation peak, and

$$\chi''(\omega) \propto \omega \quad (0 \ll \omega \ll \omega_\alpha) \quad (6.23)$$

on the low frequency side of the  $\alpha$ -relaxation peak, where  $\omega_\alpha = 1/\tau$  and  $\omega_\sigma = 1/t_\sigma$  and the exponent  $a$  ranges from 0 to 0.5 and  $b$  ranges from 0 to 1. A depiction of the meaning of power law expressions Eq. 6.21 and Eq. 6.22 is given in Fig. 6.5.

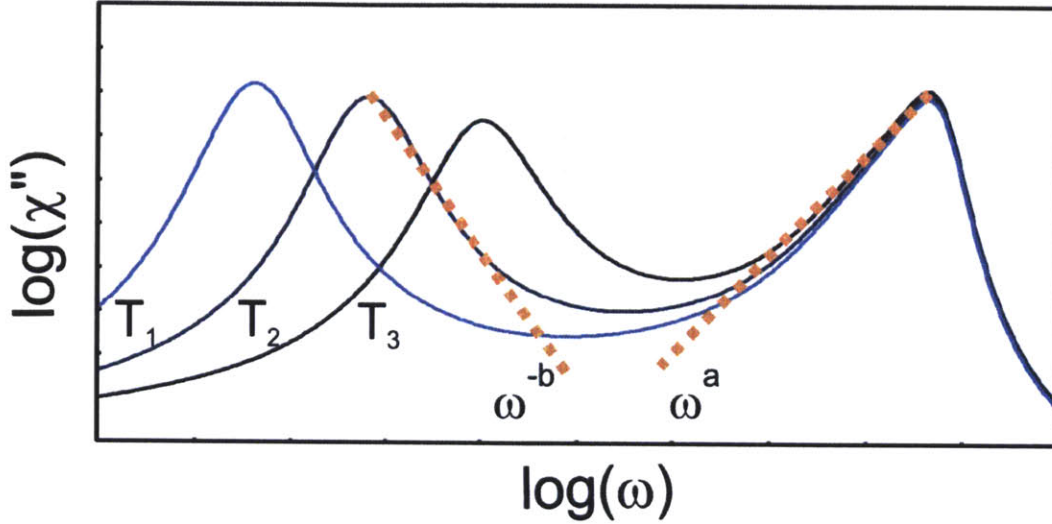


Fig. 6.5 Plot depicting imaginary susceptibility spectra at three temperatures illustrating power law MCT predictions according to Eqs. 6.21 and 6.22.

Above  $T_c$ , Eqs. 6.21 and 6.22 can be combined more explicitly to describe the behavior of the minimum in the imaginary part of the susceptibility between high and low frequency peaks, with an expression given by

$$\chi''(\omega) = \frac{\chi''_{\min}}{a+b} \left[ a \left( \frac{\omega}{\omega_{\min}} \right)^{-b} + b \left( \frac{\omega}{\omega_{\min}} \right)^a \right], \quad (6.24)$$

where  $a$  and  $b$  are the critical exponents given above,  $\chi''_{\min}$  is the magnitude of the minimum, and  $\omega_{\min}$  is the position of the minimum. Each of these latter two values also has predictions about the behavior approaching  $T_c$  from above, which are

$$\chi''_{\min}(\omega_{\min}) \propto |T - T_c|^{1/2} \quad \text{and} \quad \omega_{\min} \propto |T - T_c|^{1/2a} \quad (6.25)$$

In the following chapters we test these MCT predictions with measurements of mechanical material properties that couple directly to correlation functions related to structure and flow.



# Chapter 7

## Longitudinal & shear acoustic waves in supercooled liquids using ISS

As discussed in the previous chapter, fundamental to the study of supercooled liquids is a thorough characterization of the  $\alpha$ -relaxation across a broad range of frequencies. A survey of the literature quickly makes clear that this challenge of ultra-broadband spectroscopy has been tackled most often and completely with dielectric spectroscopy, with an unparalleled dynamic range in the study of glass forming liquids [Lunkenheimer00,Schneider,Lunkenheimer08]. But as discussed in the previous chapter, dielectric spectroscopy is most sensitive to orientational motion, while the dynamic nature of supercooling is more naturally understood in terms of density correlations that may be probed by longitudinal acoustic waves, and the transverse current, which couples to shear waves [Balucani,Boon]. Indeed, the Ideal and general MCT formulations and predictions are centered on the intermediate scattering function and higher order density correlation functions, as well as the shear waves in their own right [Wu,Mayar,Das86,Ahluwalia].

Even though an exceedingly broad frequency range is required for a complete characterization of the  $\alpha$ -relaxation as manifest in any degree of freedom, the acoustic frequency range made accessible using impulsive stimulated light scattering is often ideal for testing MCT predictions. In past ISS studies, this has allowed many MCT predictions to be tested in a variety of glass-formers [Halalay92,Yang95b,Yang96]. In the current chapter we will provide new tests of MCT predicted  $\alpha$ -scale coupling between shear and longitudinal modes, as well as the scaling law for shear wave propagation mentioned in Chapter 6. These tests were made possible by improvements in the ISBS generation and detection of shear waves spearheaded by Darius Torchinsky in the Nelson group

[Torchinsky,Torchinsky09]; much of the work and analysis presented here was carried out together with now Dr. Torchinsky. In this chapter, we discuss generally the equations of motion controlling ISS excited acoustic wave propagation in viscoelastic materials, and then present specific results and tests of the mode coupling theory.

## 7.1 ISS equations of motion

Derivations of ISS signal generation in supercooled liquids can be found with formulations in terms of viscosity or a complex modulus and different levels of detail in the literature [Yan88,Yang95a]. Here we present phenomenological versions of the isotropic linearized thermoviscoelastic equations of motion, including equations for displacement, temperature, and an orientational variable. The equation for the displacement dynamics is essentially a statement of Newton's equation given as [Christensen07]

$$\rho_0 \frac{\partial^2 \mathbf{u}}{\partial t^2} = M \nabla (\nabla \cdot \mathbf{u}) - G \nabla \times (\nabla \times \mathbf{u}) - \beta \nabla \delta T + \nabla \sigma_l, \quad (7.1)$$

where  $\mathbf{u}$  is the displacement vector,  $\rho_0$  is the equilibrium density,  $M$  is the longitudinal acoustic modulus,  $G$  is the shear acoustic modulus,  $\beta$  is the pressure coefficient (often given as a the product of the thermal expansion coefficient  $\alpha$  and bulk modulus  $K$  – see Eq. 2.3),  $\delta T$  is the deviation from equilibrium temperature, and  $\sigma_l$  is the impulsive, electrostrictive stress exerted by the laser (ISBS) given by Eq.

2.4. Given certain experimental conditions one could appropriately attach subscripts to the moduli and pressure coefficient indicating thermodynamic conditions such as  $T$  for isothermal,  $S$  for adiabatic, or  $V$  for isochoric, but it is not always straightforward in the ISS experiment; for simplicity we leave off the subscripts. The equation for the temperature dynamics is derived from the conservation of energy and given as

$$C \frac{\partial \delta T}{\partial t} + \beta T_0 \frac{\partial}{\partial t} (\nabla \cdot \mathbf{u}) = k \nabla^2 \delta T + Q_l, \quad (7.2)$$

where  $C$  is the heat capacity,  $T_0$  is a reference temperature (typically much less than the initial temperature),  $k$  is the thermal conductivity, and  $Q_l$  is the heat deposited



by the laser (ISTS; see Eq. 2.2). We see in Eqs. 7.1 and 7.2 that the pressure coefficient  $\beta$  gives the coupling between temperature and displacement (and the equations governing each). Solutions to these equations given real modulus values result in propagating waves in Eq. 7.1; the ISBS driving force drives acoustic waves directly while the ISTS driving force is manifest through the  $\beta$  term in Eq. 7.1. Next we will give simplified equations for the case of longitudinal wave generation using VV polarized pump beams (ISBS and ISTS) and shear wave generation using VH polarized pump beams (ISBS). The third equation of motion regarding orientational dynamics needs to be accounted for due to rotational-translational coupling. Although this may be important for both shear and longitudinal wave propagation, it will be included in the more immediately relevant shear ISS derivation discussed here; treatments of rotational-translational coupling in the case of ISS generated longitudinal waves are given in [Glorieux02,Pick03,Azzimani].

## 7.2 Longitudinal acoustic waves

Appropriate one-dimensional simplifications to Eq. 7.1 and 7.2 for the case of longitudinal waves (VVVV ISS experiments) give the coupled equations

$$\begin{aligned} \rho_0 \frac{\partial^2 u_x}{\partial t^2} &= M \frac{\partial^2 u_x}{\partial x^2} - \beta \frac{\partial}{\partial x} \delta T + \frac{\partial}{\partial x} F_{x0} \cos(qx) \delta(t) \\ C \frac{\partial \delta T}{\partial t} &= k \frac{\partial^2 \delta T}{\partial x^2} + Q_0 \cos(qx) \delta(t) \end{aligned} \quad (7.3)$$

with  $F_{x0}$  and  $Q_0$  giving the amplitude of each laser induced source and  $q$  the transient grating wavevector magnitude (see Eq. 2.1).

Typically the coupling term in Eq. 7.2 is small, so we neglect it, and inserting the sinusoidal VV source terms in each equation allows us to drop the shear modulus term in Eq. 7.1. Assuming spatially periodic solutions according to the source terms

and performing a temporal Fourier transform according to  $\tilde{f}(\omega) = \int_{-\infty}^{\infty} f(t) e^{-i\omega t} dt$ ,

the differential equations can be expressed as coupled equations in matrix form

$$\begin{bmatrix} -\rho_0 \omega^2 + q^2 M & iq\beta \\ 0 & i\omega + q^2 k/C \end{bmatrix} \begin{bmatrix} u_x(q, \omega) \\ \delta T(q, \omega) \end{bmatrix} = \begin{bmatrix} iqF_{x0} \\ Q_0 \end{bmatrix}. \quad (7.4)$$

Taking the inverse of the matrix on the right of Eq. 7.4 and multiplying both sides on

the left by the inverse allows the determination the variables  $u_x$  and  $\delta T$ . As discussed in Chapter 6, viscoelastic behavior is given by frequency-dependent complex elastic moduli; this complex behavior is manifest not only in the longitudinal modulus, but also in the heat capacity and pressure coefficient with similar behavior, such as the manifestation of  $\alpha$ -relaxation, in real and imaginary parts. The correspondence principle allows the direct substitution of complex moduli in the frequency domain, and time domain solutions can be recovered by an inverse Fourier transform. With certain assumptions, an analytic Fourier transform is possible and given in [Berne,Boon,Yang], but for the full solution with frequency dependence in all relevant variables, only numerical solutions are currently available. Given Yang's simplifications, the time domain follows the form

$$S(t) = A\left(e^{-\Gamma_{th}t} - e^{-\Gamma_A t} \cos(\omega_A t)\right) + B\left(e^{-\Gamma_{th}t} - e^{-(t/\tau)^\beta}\right) + Ce^{-\Gamma_A t} \sin(\omega_A t), \quad (7.5)$$

where  $\omega_A$  is the acoustic frequency,  $\Gamma_A$  is the acoustic damping rate,  $\Gamma_{th}$  is the thermal decay rate from which the thermal diffusivity can be determined (see Chapter 3), and  $\tau$  is the structural relaxation time with  $\beta$  the KWW stretching parameter. This equation was derived in the Debye approximation and stretching was added to capture the supercooled dynamics. Further key approximations specified that the relaxation time must be much longer than the inverse acoustic period and much shorter than the inverse thermal decay rate ( $1/\omega_A \ll \tau \ll 1/\Gamma_{th}$ ). [Yang95a] connected this equation to a number of MCT predictions and [Torchinsky] showed that relaxation dynamics could be measured and linked with ISS acoustic measurements. As our emphasis is mainly on the acoustics in this chapter, we will forego further discussion of the complete longitudinal ISS signal, and focus on the damped longitudinal oscillations.

In Fig. 7.1.a we show three traces displaying 1.55  $\mu\text{m}$  acoustic waves in the glass former 5-phenyl 4-ether (5P4E) at different temperatures with the express interest in observing how the structural  $\alpha$ -relaxation couples to longitudinal waves. At low temperatures the material is in the solid-like glassy state. The frequency is high corresponding to a high speed of sound and the damping rate is low. As

temperature is increased the solid starts to soften and when the characteristic structural relaxation time is on the same time scale as the inverse acoustic frequency we see strong damping. As the temperature is raised higher and the structural relaxation time moves to shorter times scales, the acoustic damping rate decreases again, the frequency continues to go down, and we can recover the lower liquid speed of sound. We also note that the acoustic oscillations extend below the zero-baseline, indicative of a combination of ISTS and ISBS excitation. Fig. 7.1.b shows the measured speed of sound as a function of temperature for 1.0  $\mu\text{m}$ , 4.9  $\mu\text{m}$ , and 29  $\mu\text{m}$  acoustic wavelengths. Relaxation-induced dispersion is evident in the temperature range from 280-350 K and the dashed labeled lines show the limiting behavior of the speed of sound at high ( $v_\infty$ ) and low ( $v_0$ ) frequencies.

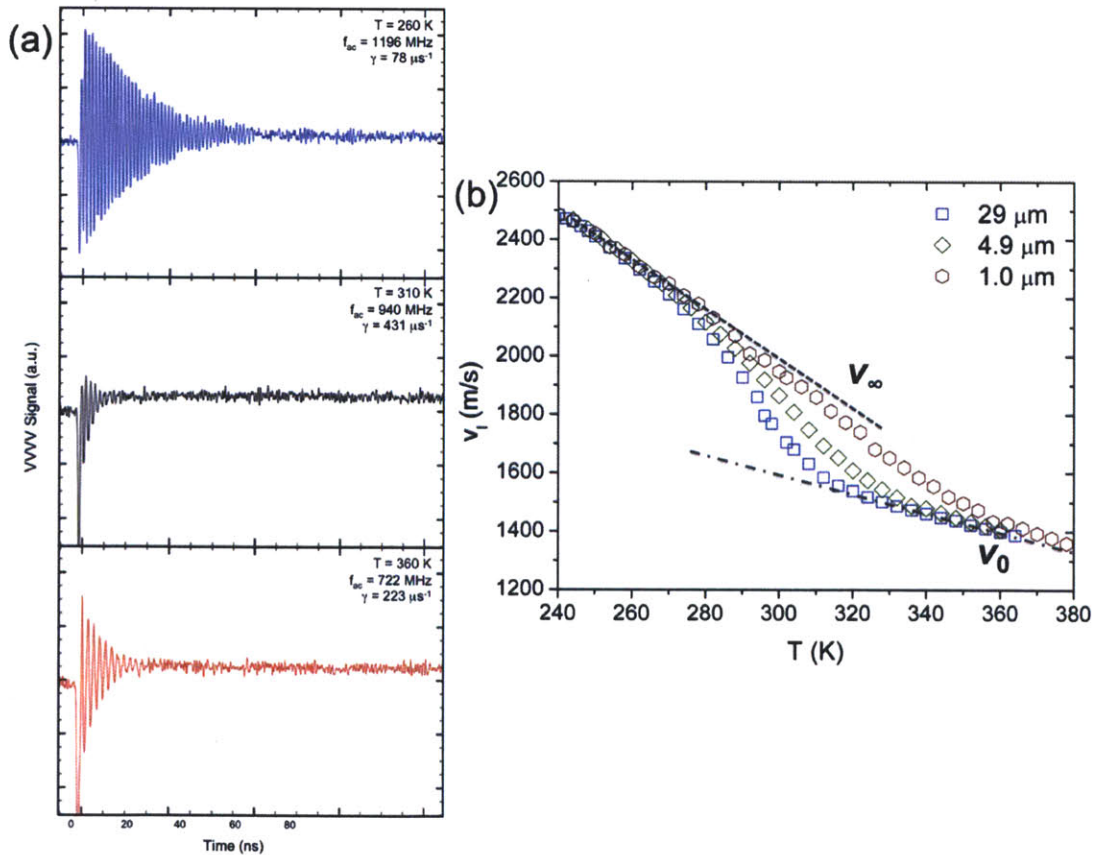


Fig. 7.1 (a) Longitudinal ISS traces in 5P4E with 1.55  $\mu\text{m}$  wavelength at three different temperatures showing behavior due to structural relaxation as described in the text. (b) Longitudinal speed of sound in 5P4E at measured at 3 wavelengths showing relaxation-induced dispersion from 280-350 K. The dashed labeled lines show limiting behavior of the sounds speed at high ( $v_\infty$ ) and low ( $v_0$ ) frequencies.

### 7.3 Shear acoustic waves

In a depolarized (VHVH) experiment, each of the pump arms carries a different polarization and the ensuing grating is described as an alternating polarization pattern, depicted in the Fig. 2.2.b. As described above and in Chapter 2, it is the regions of linear polarization that perform electrostrictive work, deforming the excited region in a fashion that generates counter-propagating shear acoustic waves. Shear acoustic waves only affect a change in the shape of a material volume element, with no density change and thus coupling to temperature is absent in isotropic materials. Therefore Eq. 7.2 can be omitted for shear waves, and with simplifications including the VH ISBS driving force and the addition of the orientational equation of motion [Frenkel,Glorieux02], the relevant coupled equations are given by

$$\begin{aligned} \rho_0 \frac{\partial^2 \mathbf{u}}{\partial t^2} &= \nabla \cdot (G \nabla \mathbf{u} + \sigma_l + \mu \Phi) \\ \frac{\partial \Phi_{ij}}{\partial t} &= -\Gamma_o \Phi_{ij} + \zeta \mu \frac{\partial}{\partial t} \left( \frac{\partial u_i}{\partial r_j} + \frac{\partial u_j}{\partial r_i} \right) + \Phi_l \end{aligned} \quad (7.6)$$

$G$  is the shear acoustic modulus,  $\sigma_l$  is the electrostrictive stress (see Eq. 2.4),  $\Phi_{ij}$  are matrix elements representing orientational motion,  $\mu$  is the rotational-translational coupling term,  $\Gamma_o$  is the orientational damping rate  $\zeta$  determines the strength of coupling from displacement to orientation, and  $\Phi_l$  is the torque exerted by the laser. Just as we did with the equations of motion for longitudinal waves, we assume spatially periodic solutions according to the source terms and perform a temporal Fourier transform to express the differential equations as coupled equations in matrix form

$$\begin{bmatrix} -\rho_0 \omega^2 + q^2 G & -iq\mu \\ q\omega\zeta\mu & i\omega + \Gamma_o \end{bmatrix} \begin{bmatrix} u_y(q, \omega) \\ \Phi(q, \omega) \end{bmatrix} = \begin{bmatrix} iqF_0 \\ \Phi_0 \end{bmatrix}. \quad (7.7)$$

Taking the inverse of the matrix on the right of Eq. 7.7 and multiplying both sides on the left by the inverse allows the determination the variables  $u_y$  and  $\Phi$ , which we give in Eq. 7.8:

$$\begin{aligned}
u_y(q, \omega) &= \frac{iq\mu\Phi_0 + iqF_0(\Gamma_o + i\omega)}{\Delta} \\
\Phi(q, \omega) &= \frac{\Phi_0(q^2G - \rho_0\omega^2) - i\omega q^2F_0\xi\mu}{\Delta} \\
\Delta &= q^2G(\Gamma_o + i\omega) + i\omega(\xi q^2\mu^2 + i\rho_0\omega(\Gamma_o + i\omega))
\end{aligned} \tag{7.8}$$

In order to arrive at a time-domain solution, we make the assumptions that the ISBS signal depends predominately the orientational variable (meaning the polarizability anisotropy couples strongly to orientation) and that  $\xi q^2\mu^2$  is a higher order coupling that can be ignored. For the orientational variable we arrive at, using  $s = i\omega$  to avoid confusion of variables in subsequent steps,

$$\Phi(q, s) = \frac{\Phi_0}{(\Gamma_o + s)} - \frac{sq^2\xi\mu F_0}{\rho_0(\Gamma_o + s)(s^2 + q^2G/\rho_0)} \tag{7.9}$$

To determine the effect of structural relaxation dynamics on the signal and to recover an analytical time-domain solution, we model the  $\alpha$ -peak by Debye relaxation (see Eq. 6.5). Eq. 7.9 can then be recast into the form

$$\Phi(q, s) = \frac{\Phi_0}{(\Gamma_o + s)} - \frac{q^2\xi\mu F_0}{\rho_0} \frac{s + 2\Gamma_s}{(\Gamma_o + s)(s + \Gamma_s + i\omega_s)(s + \Gamma_s - i\omega_s)} \tag{7.10}$$

where the shear acoustic damping rate  $\Gamma_s$  is given by

$$\Gamma_s = \frac{1}{2\tau_s} \tag{7.11}$$

and the frequency of oscillating shear waves  $\omega_s$  is

$$\omega_s = \sqrt{v_\infty^2 q^2 - \left(\frac{1}{2\tau_s}\right)^2} \tag{7.12}$$

The shear relaxation time is  $\tau_s$  and the infinite frequency speed of sound is  $v_\infty$ . One standard distinction between liquids and solids is that solids can support shear waves, whereas liquids cannot. We note that in the Debye relaxation approximation used here, whether the material behaves like a solid or liquid at a particular wavevector is determined by the relaxation time. The acoustic wavevector  $q_0$  for which propagation ceases is determined using Eq. 7.12 when  $\omega_s$  goes to zero:

$$q_0 = \frac{1}{2\tau_s v_\infty} \tag{7.13}$$

Shear waves will propagate for  $q > q_0$ , but diffusive motion will result for wavevectors  $q < q_0$ . Separation of 7.10 by partial fractions, and a subsequent inverse Fourier transform, yields the time-domain solution

$$\begin{aligned}\Phi(q, t) &= A \left[ \left( B \sin(\omega_s t) + C \cos(\omega_s t) \right) e^{-\Gamma_s t} - C e^{-\Gamma_o t} \right] + \Phi_0 e^{-\Gamma_o t} \\ A &= \frac{q^2 \xi \mu F_0}{\rho_0 \left( (\Gamma_s - \Gamma_o)^2 + \omega_s^2 \right)} \\ B &= \frac{\omega_s^2 + \Gamma_o \Gamma_s - \Gamma_s^2}{\omega_s} \\ C &= \Gamma_o - 2\Gamma_s\end{aligned}\tag{7.14}$$

Typically  $B$  is much larger than  $C$ , giving a simple equation of a damped oscillation for the shear waves and a single exponential for the orientational response.

Despite the importance of both longitudinal and shear degrees of freedom, due to the relatively limited means by which shear waves may be generated and probed, the majority of the supercooled liquid literature has centered on the study of the longitudinal modulus. As will be discussed in more detail in the next chapter, a variety of methods can continuously cover the longitudinal spectrum from mHz up to the mid-GHz regime. However, broadband shear wave generation is more accessible experimentally at lower frequencies and exhibits a gap in the range from the  $\sim 10$  MHz limit of transducer methods [Ferry, Rossiter] to the low GHz frequencies probed by depolarized (VH) Brillouin Scattering [Huang, Dreyfus, Tao]. The bulk of depolarized Brillouin Scattering studies are performed in a single scattering geometry, permitting observation of only one acoustic wavevector. Many attempts have been made to obtain relaxation information, but of necessity complex modeling is employed with imprecise multi-parameter fitting, incorporating contributions from the various channels that give rise to depolarized light scattering.

In this chapter, we utilize recent advancements in the ISBS generation and detection of coherent shear waves [Nelson, Torchinsky09] to provide tests of the MCT predicted  $\alpha$ -coupling [Götze99]. Earlier experimental studies that have examined  $\alpha$ -coupling have focused on, e.g., the coupling of dielectric to rheological variables

[Zorn], dielectric to shear mechanical relaxation [Jakobsen], and of translational to rotational diffusion [Lohfink]. However, there have been no studies that directly compare elastic degrees of freedom with each other. We will also examine the predicted, albeit untested power-law divergence of an upper bound length scale for shear wave propagation upon cooling [Ahluwalia].

#### **7.4 Experimental study of triphenyl phosphite**

Building upon prior work [Silence91,Silence92], we present an expanded study of the shear acoustic behavior of the fragile glass-former triphenylphosphite (TPP) ( $T_g = 202$  K [Mizukami]). Together, the experiments fill in the gap between 10 MHz and 1 GHz in the shear relaxation spectrum, and thus constitute the broadest bandwidth shear acoustic measurements performed optically on any glass forming system, enabling characterization of shear relaxation in glass-forming liquids in this frequency regime. Although supercooled liquid  $\alpha$ -relaxation spectra are typically broader than two decades at any temperature and, as  $T$  is varied, the spectra move across many decades, the 10-1000 MHz range is sufficient to permit comparison of relaxation spectra from shear and longitudinal wave measurements at similar frequencies.

We utilized the NIR setup where the pump laser wavelength was the fundamental of the Yb:KWP system lasing at 1030 nm and producing pulses of 500  $\mu$ J at a repetition rate of 1 kHz, although 150  $\mu$ J was routinely used to avoid cumulative degradation of the sample. The excitation beams were cylindrically focused to a spot that was 2.5 mm in the grating wavevector dimension and 100  $\mu$ m in the perpendicular dimension so that the acoustic waves would have many periods and the decay of signal would be due primarily to acoustic damping rather than propagation away from the excitation and probing region of the sample. The probe and reference beams were derived from the 150 mW 830 nm CW diode laser focused to a spot of 1 mm in the grating dimension by 50  $\mu$ m in the perpendicular dimension.

In order to generate crossed polarizations, we inserted  $\lambda/2$  waveplates into each of the beams between imaging lenses as depicted in Fig 2.1. The waveplates were held



in precision rotation mounts to provide accurate alignment of the relative polarizations of the V and H polarized beams. This set the upper limit on the grating spacing that could be achieved in our measurements; for longer wavelengths, the beams came close enough together to be clipped by the rotation mounts. Imaging with longer focal length optics allowed access to longer transient grating periods. The shear signals were weak and required 10,000 averages, resulting in data acquisition times of a few minutes for each temperature/wavevector trace.

TPP at 97% nominal purity was purchased from Alfa Aesar and had both water and volatile impurities removed by heating under vacuum with the drying agent  $\text{MgSO}_4$  immersed in the liquid. The sample was then transferred to a cell with movable windows [Halalay] via filtering through a millipore 0.22  $\mu\text{m}$  teflon filter. After loading, the cell was placed in the cryostat for temperature tuning.

The seventeen transient grating periods examined in this study ranged from 2.33 to 50.7  $\mu\text{m}$ , with additional data for 0.48  $\mu\text{m}$ , 1.52  $\mu\text{m}$ , 3.14  $\mu\text{m}$ , and 4.55  $\mu\text{m}$  periods taken from prior reported results [Silence91,Silence92]. The acoustic wavelengths were calibrated through ISS measurements in ethylene glycol, for which the speed of sound is known to a high degree of accuracy [Silence]. Data were recorded for each wavevector heating the sample every 2 K from 220 K to 250 K, which we found slowed crystallization relative to cooling. The tendency toward crystallization was particularly pronounced in the temperature range between 234 K and 242 K. Additionally, after a few days of use we replaced the sample with a new one due to a slightly cloudy yellowish hue developing; comparison of the signals obtained from the degraded samples and fresh ones yielded the same frequency and damping rate values, indicating that uncertainties in either of these quantities were due mainly to noise in the data.

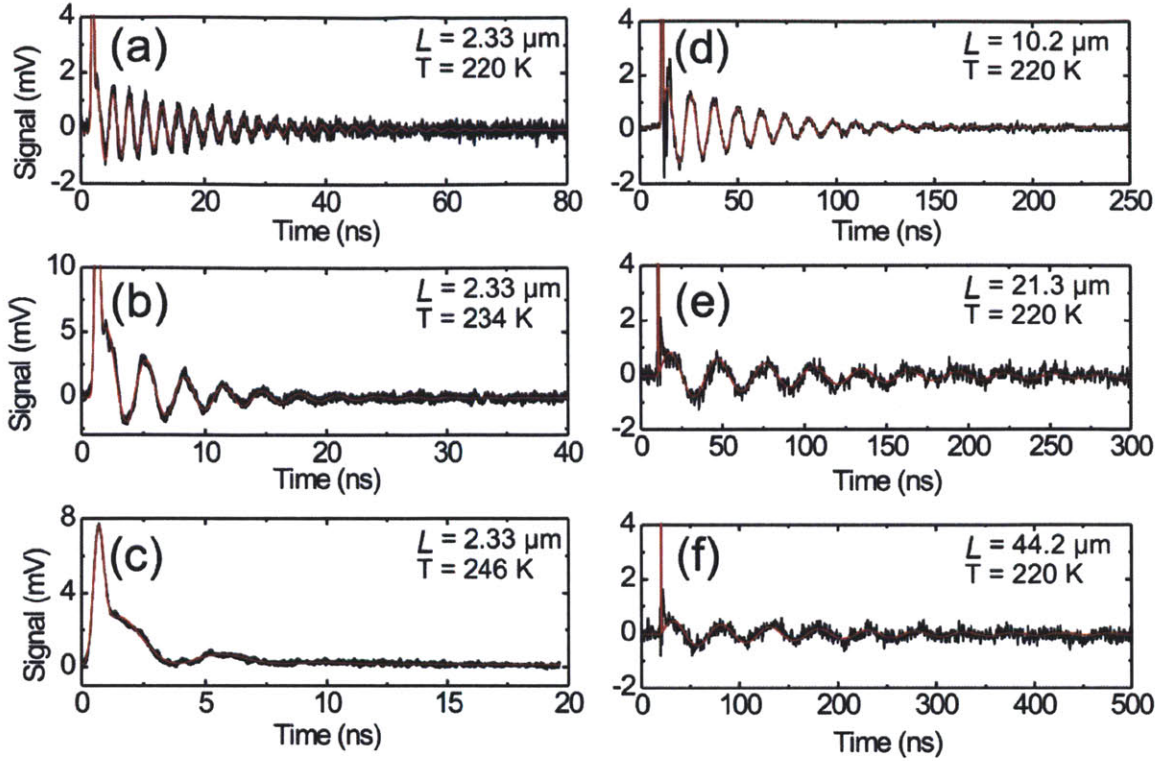


Fig. 7.3 (a-c) Shear waves in TPP with  $L = 2.33 \mu\text{m}$  at (a) 220 K, (b) 234 K, and (c) 246 K. The data are black and the fits are red. As temperature is increased, the acoustic wave becomes more heavily damped, until eventually it becomes over damped and oscillatory motion ceases. (d-f) Shear waves in TPP at  $T = 220 \text{ K}$  for (d)  $L = 10.2 \mu\text{m}$ , (e)  $21.3 \mu\text{m}$ , and (f)  $44.2 \mu\text{m}$ . Again the data are black and the fits are red. We observe that the acoustic damping increased for larger grating periods at the same temperature.

### 7.5 TPP results and discussion

Six shear acoustic signal traces recorded in TPP are shown in Fig. 7.3. Immediately following the initial hyperpolarizability spike, oscillations due to counter-propagating shear waves appear about the zero baseline. In 7.3.a for  $2.33 \mu\text{m}$  grating period, the shear oscillations are seen to disappear at 220 K on the scale of tens of nanoseconds due to acoustic damping. As the sample was warmed in 7.3.b and 7.3.c, the frequency was observed to decrease and the damping increased dramatically. At sufficiently high temperatures, eventually oscillatory motion ceased and the shear wave became over damped. Additionally at higher temperatures, the signature of orientational relaxation was observed as a non-oscillatory decay component in the signal (e.g. in 7.3.c). In 7.3.d-f we provide another illustration of the influence of relaxation dynamics on the signal by examining data from a

collection of wavevectors at a common temperature: data recorded with (d) 10.2  $\mu\text{m}$ , (e) 21.3  $\mu\text{m}$ , and (f) 44.2  $\mu\text{m}$  periods at 220 K. Data with a fourth wavelength, 2.33  $\mu\text{m}$ , are shown in (a). As the wavevector and the frequency are reduced, the acoustic oscillation period increases toward the characteristic relaxation timescale  $\tau_s$  and the shear wave is more heavily damped.

Based on the analysis of section 7.3, time-domain signals were fit to the function

$$S(t) = A' \exp(-\Gamma_s t) \sin(\omega_s t + \phi) + B' \exp(-\Gamma_R t) + C \delta(t) , \quad (7.15)$$

which was convolved with the instrument response function, modeled here by a Gaussian with duration 0.262 ns. The convolution was necessary to determine the true  $t = 0$  for the experiment.  $A'$  is the acoustic amplitude,  $\Gamma_s$  is the shear damping rate and  $\omega_s$  is the shear frequency, and  $\phi$  is a phase which accounts for the cosine term in Eq. 7.14, which only becomes important when the damping is strong. In the next term,  $B'$  is the optical Kerr effect signal amplitude and  $\Gamma_R$  is the orientational relaxation rate, and  $C$  in the last term is the strength of the hyperpolarizability spike. As discussed above, to model the orientational behavior by a single decaying exponential is a simplification [Hinze]; however, since the orientational signal contributions are weak, we were able to obtain excellent fits using a single exponential form.

The obtained values of the shear acoustic velocity  $v_s = \omega_s/q$  at a collection of wavevectors are shown in Fig. 7.4.a and in Fig. 7.4.b the scaled damping rates are shown. Both figures incorporate the data from [Silence91,Silence92] as unfilled symbols and data at other wavevectors, although consistent with those shown here, were omitted for clarity. In 7.4.a we observe significant acoustic dispersion in the shear sound speed for all temperatures below about 220 K. We also note that at each temperature above 240 K, there is an acoustic wavelength above which we are unable to observe the shear wave in our measurements due to the increased damping and reduced signal strength. This wavelength is observed to decrease as temperature increases.

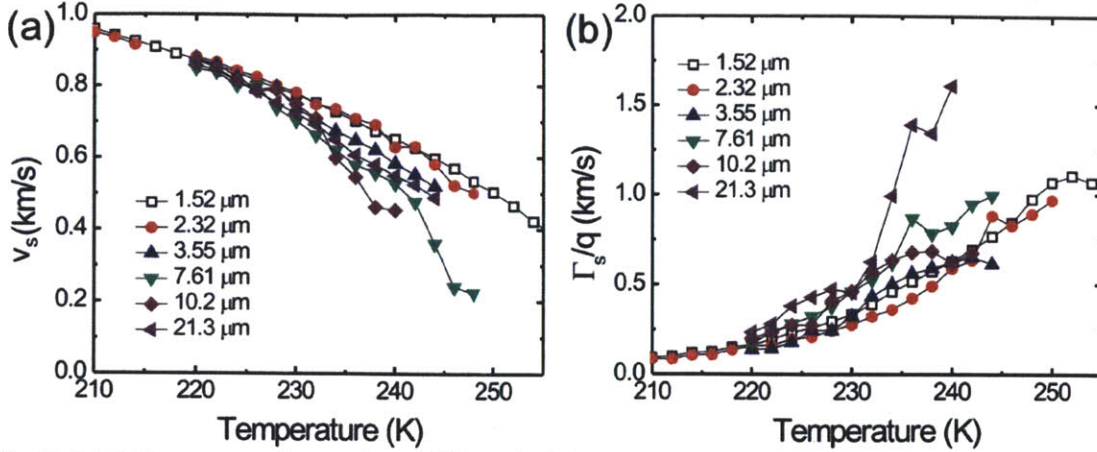


Fig. 7.4 (a) Shear sound speed and (b) scaled damping rate in TPP as a function of temperature for six grating periods. Significant dispersion and damping is observed at higher temperatures. The open squares for  $L = 1.52 \mu\text{m}$  are from [Silence91, Silence92].

From the fitted values for the shear frequency  $\omega_s$  and the damping rate  $\Gamma_s$ , we may compute the real and imaginary parts of the shear modulus according to

$$\begin{aligned} G'(\omega) &= \rho_0 \frac{\omega_s^2 - \Gamma_s^2}{q^2} \\ G''(\omega) &= \rho_0 \frac{2\omega_s \Gamma_s}{q^2} \end{aligned} \quad (7.16)$$

Identical equations allow the determination of the complex longitudinal modulus using measured longitudinal frequencies and damping rates. The density values for TPP we obtained from data in [Ferrer] that fit to a quadratic function as

$$\rho_0(T) = 1.507 [g/cm^3] - 1.3 \times 10^{-3} T[K] + 6.8 \times 10^{-7} T^2[K^2]. \quad (7.17)$$

Fig. 7.5 shows plots of the real (a) and imaginary (b) parts of the shear modulus, as functions of temperature. These plots are for the same collection of wavevectors plotted in Fig. 7.4. As in the plot of the velocity, we see the softening of the modulus at higher temperatures. The imaginary part shows generally monotonic behavior as a function of temperature as well.



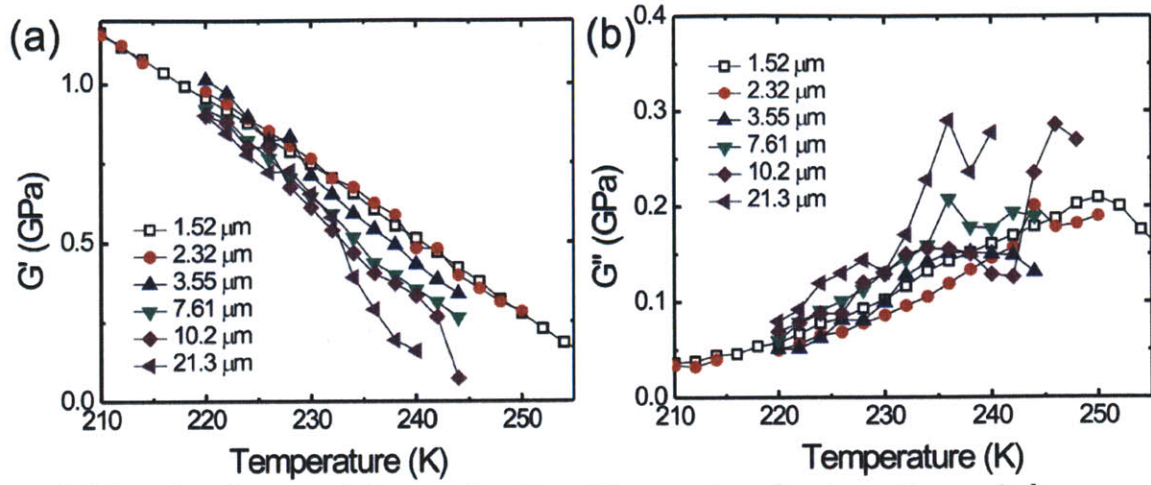


Fig. 7.5 Complex shear modulus as a function of temperature for six grating periods. Significant dispersion in the real part (a) and damping in the imaginary part (b) are observed at higher temperatures, following the speed and damping rate trends. The open squares for  $L = 1.52 \mu\text{m}$  are again from [31,32].

In order to extract the shear relaxation time  $\tau_s$  at each temperature, we plotted the modulus as a function of frequency and then fit it to the Havriliak-Negami relaxation function [Havriliak]

$$G^*(\omega) = G_\infty \left[ 1 - \left( 1 + (i\omega\tau_s)^\alpha \right)^{-\beta} \right]. \quad (7.18)$$

Note in comparison to Eq. 6.5 that by definition,  $G_0 = 0$  for all temperatures. Time-temperature superposition has been observed to hold for  $\alpha$ -relaxation in many liquids including TPP [Olsen], so we fit all spectra simultaneously to obtain  $\tau_s(T)$  with the spectral parameters  $\alpha$  and  $\beta$  acting as temperature-independent global variables. The value for the temperature-dependent infinite frequency shear modulus  $G_\infty = \rho v_\infty^2$  was taken from our low temperature data combined with depolarized Brillouin scattering results performed by [Chappell]. A linear fit to the combined data set gives

$$v_\infty = 2620.4[m/s] - 7.93T[K]. \quad (7.19)$$

To obtain the above expression, we needed to derive a temperature-dependent refractive index using (VV) Brillouin scattering data from longitudinal acoustic waves [Ferrer], which we could then use to recover the shear sound speed in [Chappell].

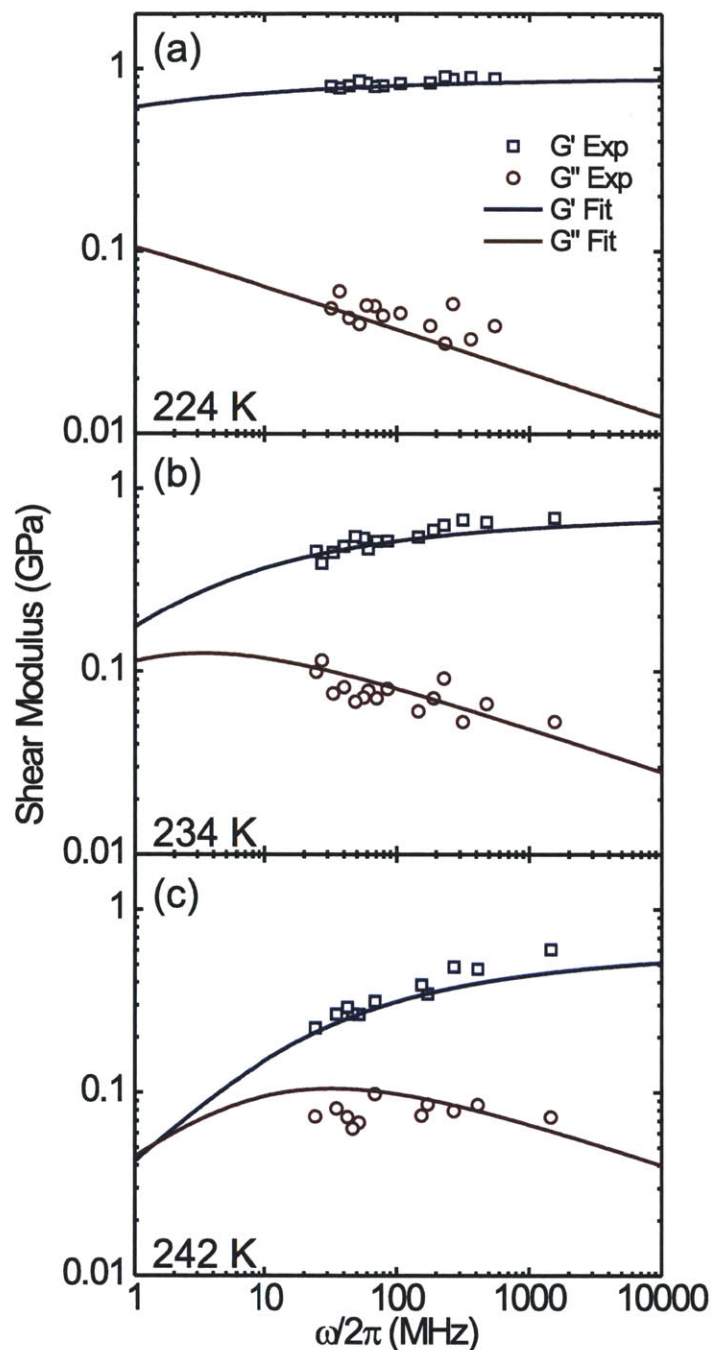


Fig. 7.6 Plots of the real ( $G'$ ) and imaginary ( $G''$ ) shear moduli of TPP at (a) 224 K, (b) 234 K, and (c) 242 K. The shear relaxation spectrum shifts with temperature and we observe a different portion in our experimental frequency window at each temperature.

Three representative plots of the complex shear modulus with corresponding fits are shown in Fig. 7.6. As the temperature is increased, the shear relaxation spectrum moves to higher frequencies in the probed region. The fits produced spectral parameters  $\alpha = 0.61$  and  $\beta = 0.39$ . Although not shown here, the longitudinal data

from [Silence91,Silence92] were refit using the same procedure for consistency and comparison of  $\tau_s$  and  $\tau_l$ , yielding spectral parameters  $\alpha = 0.69$  and  $\beta = 0.30$ , which given the accuracy of the fits, are comparable to the shear spectral parameters.

The fitted values of  $\tau_s$  and  $\tau_l$  as a function of temperature along with respective VFT fits are presented in Fig. 7.7. There is excellent agreement between the two timescales up to the temperature  $T = 231$  K, where the characteristic relaxation times clearly separate. At the lower sample temperatures measured, we conclude that the shear acoustic wave dynamics differ significantly from those obtained from the earlier longitudinal ISS data [Silence91,Silence92]. Based on a larger data set taken with a broader range of acoustic wavevectors, this conclusion supersedes the results of the previously published work.

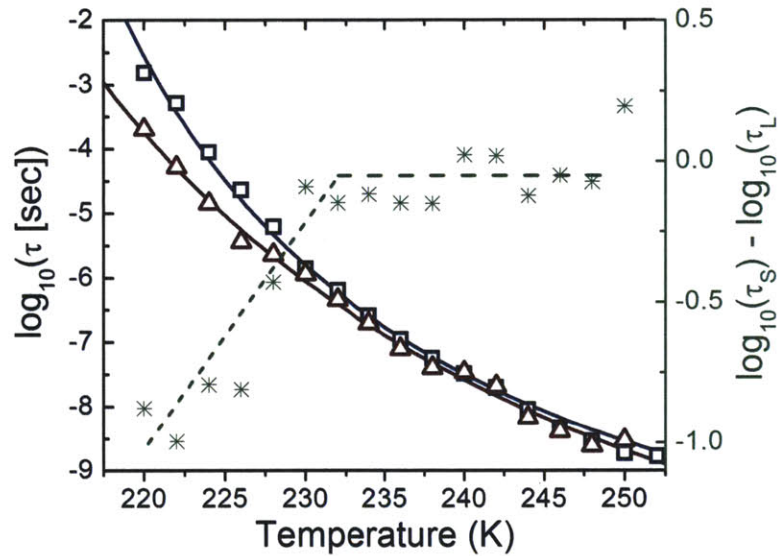


Fig. 7.7 Characteristic shear ( $\tau_s$ ) and longitudinal ( $\tau_l$ ) relaxation times plotted versus temperature (left ordinate) with associated VFT fits (solid lines). Also shown is the decoupling parameter  $\log \tau_s - \log \tau_l$  as a function of temperature (right ordinate). The dashed line is to guide the eye and indicates the decoupling at 231 K.

We can now use our data to examine the MCT predicted  $\alpha$ -coupling described briefly in section 6.2.3. Using the determined values of  $\tau_s$  and  $\tau_l$  as a function of temperature, the decoupling parameter defined as  $\log \tau_s - \log \tau_l$  is plotted alongside the relaxation times in Fig. 7.7. The decoupling parameter is constant and essentially zero until it begins to decrease with decreasing temperature, reflecting the shear



relaxation becoming faster than the longitudinal relaxation. MCT predicts that variables that couple to structural relaxation will have a decoupling parameter that doesn't vary with temperature above  $T_c$ , thus this decoupling provides an estimate of the MCT crossover temperature  $T_c = 231$  K.

We may attempt to further understand our results in the mode-coupling framework of [Ahluwalia]. Briefly, when MCT calculations are performed using the static structure factor of a collection of hard spheres in the Percus-Yevick approximation, the critical length scale  $L_0 = 2\pi/q_0$  above which propagation of shear waves becomes over damped obeys a power law approaching the critical temperature according to

$$L_0 = \frac{A}{(\Delta_c - \Delta)^\delta}, \quad (7.20)$$

where  $A = 1$ ,  $\delta = 1.2$ ,  $\Delta$  is the packing fraction, and  $\Delta_c$  is the Ideal MCT critical packing fraction beyond which shear wave propagation is allowed for all length scales. Using Eq. 7.13, we attempt to deduce a limiting length scale for shear wave propagation as a function of temperature by considering at which wavevector shear wave propagation becomes over damped. For this analysis, we chose the temperature  $T$  to be the independent parameter, yielding a similar power law  $L_0 = A(T - T')^{-\delta}$ , where  $T'$  represents a critical temperature. Here we consider two significant temperatures for the liquid, i.e., the glass transition temperature  $T_g = 202$  K [Mizukami] and the crossover temperature  $T_c$  as determined from the MCT decoupling analysis above.

Figure 7.8 shows a plot of the derived upper bound, as deduced from Eq. 7.13 as a function of the variable  $\Theta = (T - T')$ . The results of [Ahluwalia] are also shown as a function of packing fraction  $\Theta = (\Delta_c - \Delta)$  for comparison. A power law fit is shown to the four points approaching the relevant temperatures (open symbols). Picking  $T' = T_c$  as the relevant temperature yields a fitted value of  $\delta = 1.2$ , which is in excellent agreement with the theoretical result. A similar fit to the data using the literature value of  $T' = T_g$  produces a significantly higher value of  $\delta = 13.4$ . We remark that the wavelength scales  $L_0$  reached as this temperature is approached from above are several orders of magnitude larger than those corresponding to any diverging

structural correlation length scale.

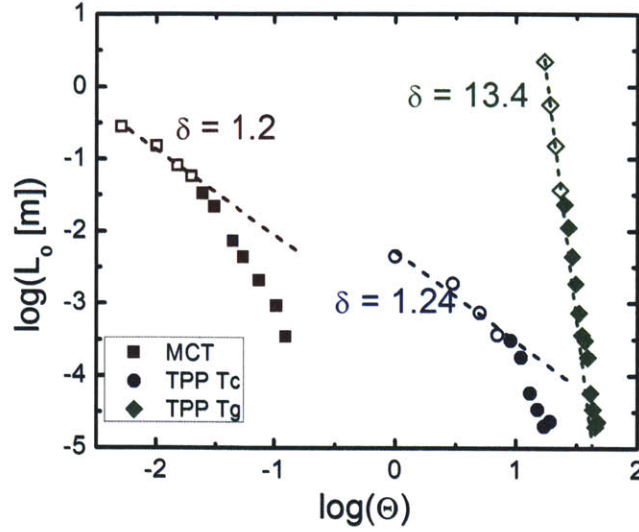


Fig. 7.8 Determined value of the critical length scale for shear wave propagation as a function of temperature  $\Theta = T - T^*$  using the decoupling temperature  $T^* = T_c$  (blue circles) and the glass transition temperature  $T^* = T_g$  (green diamonds). For comparison, the calculations of [Ahluwalia] are also shown as a function of packing fraction  $\Theta = \Delta_c - \Delta$  (red squares). The exponents come from fits to the open symbols approaching  $\Theta = 0$ .

## 7.6 Summary

We have used depolarized impulsive stimulated Brillouin scattering to measure shear acoustic waves in supercooled TPP from 220 K to 250 K. Combined with previous results [Silence91,Silence92], we are able to examine a frequency regime from  $\sim 10$  MHz to almost 1 GHz. We observed decoupling of the longitudinal and shear degrees of freedom, yielding an estimate of the mode-coupling  $T_c = 231$  K. Using the decoupling temperature, we verified a power law for the diverging lengthscale of shear wave propagation as  $\delta = 1.2$ . A similar test using the literature value of  $T_g$  was not in agreement with the theoretical model, as should be expected since  $T_g$  is not a mode-coupling theory parameter. One clear disadvantage to the Ideal MCT, is the prediction of a divergence in the relaxation time as given in Eq. 6.17. The analysis given in this chapter has the advantage of determining the MCT  $T_c$  when no divergence exists in reality (see Fig. 7.7).

Further work in the study of shear relaxation in supercooled liquids will center on

expanding the dynamic range of the measurements. We note that recent measurements comparing the relaxation spectrum of different degrees of freedom of the glass formers DC704 and 5P4E, including shear and longitudinal moduli, at lower temperatures and frequencies indicate a constant decoupling parameter with temperature ( $\log \tau_s - \log \tau_l = \text{constant}$ ) [Hecksher], just as we see at high temperature in TPP. If this behavior is universal in many glass formers, including TPP, then we would expect a step in decoupling parameter from high to low temperatures, indicating some change in dynamics at the MCT  $T_C$ . For a complete analysis of this idea, broadband spectra over many orders of magnitude in frequency would need to be collected and compared. In the next chapter, we outline some major steps in this direction where we present the most comprehensive to date, broadband longitudinal acoustic spectrum.



# Chapter 8

## Broadband longitudinal acoustic spectroscopy of DC704

Due to the many order of magnitude change in the  $\alpha$ -relaxation time with temperature, an enormous experimental dynamic range is required for a complete characterization of supercooled liquid dynamics. For many years it has been a goal in the Nelson group to produce broadband mechanical spectra of a glass forming liquid that rivals the frequency content possible with dielectric spectroscopy. ISS experiments performed to examine longitudinal wave dynamics at MHz to low GHz frequencies have been carried out in the group since the earliest days [Nelson,Yan87,Silence91,Halalay92, Yang95b,Torchinsky]. But as discussed in Chapter 2, ISS experiments are fundamentally limited by the smallest and largest acoustic wavelengths that can efficiently be generated. Fortunately we have collaborators in Jeppe Dyre's group at Roskilde Universitet in Denmark, including Tina Hecksher who worked in our group for a time, who were able to directly measure the complex shear and bulk moduli at low frequencies (mHz to kHz) using piezo-transducer methods [Christensen,Hecksher]. More recent progress in the Nelson group led by Christoph Klieber has also advanced our capabilities in generating and detecting higher frequency GHz acoustic waves in liquids utilizing picosecond ultrasonics. Recently we have been able to combine temperature-dependent data collected using the three techniques for the glass forming liquid liquid tetramethyl tetraphenyl trisiloxane (DC704), a diffusion pump oil originally produced by the Dow Corning company. The cohesive force between DC704 molecules in the liquid is predominately due to weak van der Waals interactions. The molecule is depicted in Fig. 8.1 Tina Hecksher used the piezo-transducer technique to measure the shear ( $G$ ) and bulk ( $K$ ) moduli, which can be combined to give the longitudinal modulus ( $M = K + 4/3G$ ). Darius Torchinsky collected much of

the longitudinal ISS data, and I added some additional points at higher wavevectors. Christoph Klieber collected the vast majority of picosecond ultrasonic data. In-depth details on each of these techniques and measurements can be found in their respective theses [Hecksher,Torchinsky,Klieber] and will not be reproduced here.

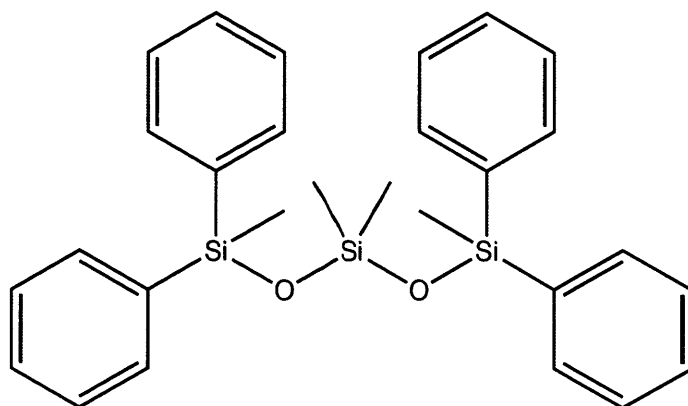


Fig. 8.1 The chemical structure of tetramethyl tetraphenyl trisiloxane. Van der Waals interactions provide the attractive force in the liquid.

Together, these techniques cover acoustic frequencies from mHz to hundreds of GHz, but there is a large gap in frequency between the low-frequency measurements (up to  $\sim 10$  kHz) and the ISS measurements (down to  $\sim 30$  MHz). To help close this gap we developed the nanosecond acoustic interferometry (NAI) technique introduced in Chapter 2. In this chapter, we will give a brief overview of NAI and discuss the analysis in regards to viscoelastic materials, namely DC704. We will then present the combined broadband spectra and several tests of MCT. It is important to note that even though the analysis shown here has been performed carefully, it is still a work in progress as more careful analysis from all the data sets may provide modifications to the broadband spectra.

### 8.1 Nanosecond acoustic interferometry of DC704

As outlined in Chapter 2, in an NAI experiment a single, round pump laser spot is focused through a dichroic mirror into the liquid sample cell ( $\sim 250 \mu\text{m}$   $1/e$  beam radius) containing DC704. The precise laser spot size is not important to the

analysis, but it does determine the wavevector and therefore frequency content of the wavepacket (see Eq. 2.16) radiating outward from the pump beam. As depicted in Fig. 2.10, the wavepacket with  $\sim 1$ -10 MHz frequency components will pass first through one probe arm of the grating interferometer and subsequently the second. Acoustic wave-induced changes in refractive index vary the phase of each interferometer probe arm in turn, translating to time-dependent changes in intensity at the optical detector. In Fig. 8.2 we show NAI traces collected in DC704 at a number of different temperatures.

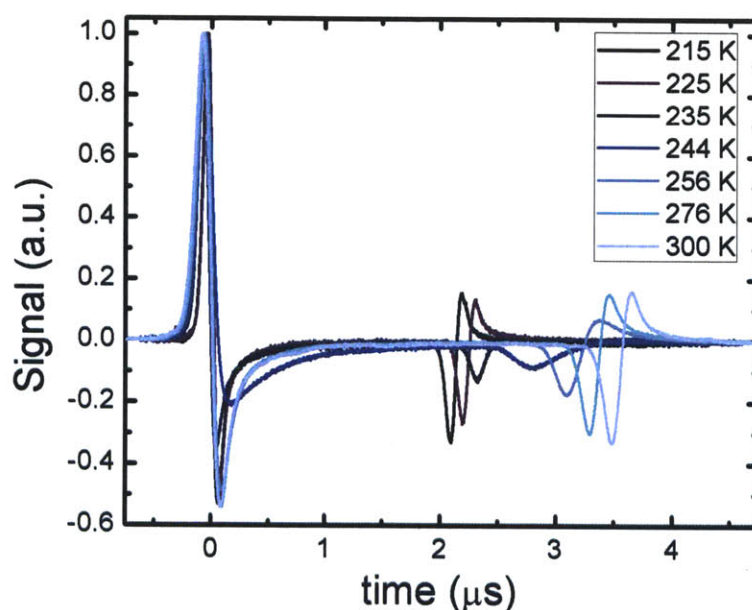


Fig. 8.2 NAI traces recorded in DC704 at a number of different temperatures showing the effects of structural relaxation. The probe beams were spaced about 5 mm apart.

The effects of the coupling of structural relaxation to the acoustic waves are apparent. Firstly, we observe that as temperature is decreased, the wavepacket arrives at the second probe point more quickly, corresponding to the speed of sound increasing at lower temperatures. Secondly, we see that the amplitude of the wavepacket has strong temperature dependence. Acoustic damping is relatively low at high temperatures in the liquid state, but as temperature is reduced and the  $\alpha$ -relaxation peak shifts to lower frequencies, eventually it overlaps with the frequency content of the wavepacket and strong damping is evident. As temperature is decreased further, the  $\alpha$ -relaxation shifts to lower frequencies and



we see the damping is reduced in the low-temperature glass state. We also note that even in the absence of acoustic damping, the amplitude of the pulse at the second probe point will decrease solely due the divergent nature of the cylindrical wavepacket. In principle it would be possible to conduct such NAI experiments with a line-focused pump pulse, but in practice the acoustic damping is weak enough for these low-MHz frequencies that relatively long propagation distances are necessary – so long that divergence effects would be significant even for a line-focused pump beam (with adequate laser fluence to generate a response). To avoid such complications, we used the round spot excitation to generate cylindrical acoustic waves with a well-defined  $r^{-1/2}$  reduction in amplitude.

Using Fourier analysis, we can determine the velocity and attenuation for the excited frequency components, and therefore determine the complex acoustic modulus and compliance. The Fourier shift theorem states that for a function shifted in the time domain, the Fourier transform acquires a phase factor as

$$\underset{\substack{\text{Fourier} \\ \text{Transform}}}{f(t-a)} \Rightarrow e^{-ia\omega} F(\omega), \quad (8.1)$$

where  $f(t)$  and  $F(\omega)$  are Fourier transform pairs. Using this property and the distance  $d$  between interferometer probe arms, we can recover the speed of sound for the excited frequency components. In Eq. 8.1, the acquired phase ( $\varphi$ ) of the Fourier transform is  $a\omega$ , and thus by taking the derivative of the phase ( $\partial_\omega \varphi$ ) with respect to frequency, we recover the frequency-dependent shift in time  $a(\omega)$ . Using the Fourier transforms of the wavepacket individually at the first probe point and second probe point, we can determine the frequency-dependent sound speed  $v(\omega)$

$$v(\omega)[m/s] = \frac{d}{\partial_\omega \varphi_1(\omega) - \partial_\omega \varphi_2(\omega)} = \frac{d}{\Delta t(\omega)}. \quad (8.2)$$

In practice, the amplitude of the phase recovered from a numerical Fourier transform may depend on the number of time points in the time-domain trace, and so we needed to multiply Eq. 8.2 by a constant calibration factor. All recorded traces contained an identical number of time points, and therefore a single calibration factor for all analysis was sufficient. The calibration factor was picked to recover

the solid sound speed determined at low temperatures from piezo and ISS data; this calibration factor also recovered the liquid sound speed at high temperatures (in comparison to ISS data), and so we confidently use it for all temperatures. All points presented here were also collected with the same probe distance  $d$ , which can be determined using the grating period and the lens focal distance, according to

$$d = 2f \tan\left(\sin^{-1}\left(\frac{\lambda_p}{2g}\right)\right), \quad (8.3)$$

where  $f$  is the lens focal length,  $\lambda_p$  is the probe wavelength, and  $g$  is the grating period. With 532 nm probe wavelength, 85 mm lens focal length, and 8.5  $\mu$ m grating period, this translated to  $\sim 5$  mm between probe beams which agreed with a physical measurement of the distance.

The frequency-dependent acoustic attenuation  $\gamma(\omega)$  can be determined by the amplitude of the Fourier transform of the acoustic pulse at each probe point according to the Beer-Lambert law which we give as

$$\gamma(\omega)[m^{-1}] = -\frac{1}{d} \ln\left(A|F_2(\omega)|/|F_1(\omega)|\right). \quad (8.4)$$

We note that attenuation here is given in units of inverse distance, whereas the damping rate in the previous chapter is given in inverse time units; conversion between the two can be performed using the speed of sound. Correction due to the acoustic wave divergence is accomplished by simply adding the constant factor  $A$  that appears in Eq. 8.3.  $A$  depends on  $d$  and the distance from the pump spot to the first probe spot ( $d_p$ ) and is given by

$$A = \frac{\sqrt{d_p + d}}{\sqrt{d_p}} \quad (8.5)$$

For the density of DC704 we use an expression that includes the thermal expansion coefficient and density at a reference temperature [Hecksher] given by

$$\rho_0(T) = 1.07 / (1 + 0.00072 (T[K] - 298)). \quad (8.6)$$

Using the density and determined frequency-dependent velocities and attenuation, we can construct the complex longitudinal modulus, with real and imaginary parts

given by [Herzfeld]

$$M'(\omega) = \rho_0 v_\omega^2 \frac{1 - (\gamma_\omega v_\omega / \omega)^2}{\left(1 + (\gamma_\omega v_\omega / \omega)^2\right)^2}$$

$$M''(\omega) = 2\rho_0 v_\omega^2 \frac{\gamma_\omega v_\omega / \omega}{\left(1 + (\gamma_\omega v_\omega / \omega)^2\right)^2} . \quad (8.7)$$

In the following section, we combine the NAI-determined modulus values with the piezo, ISS, and picosecond ultrasonics data for broadband analysis and tests of MCT.

## 8.2 Broadband spectra of DC704

As briefly discussed in Chapter 6, even though the relationship between the complex acoustic compliance  $J^*(\omega)$  and the complex modulus  $M^*(\omega)$  is simply

$$J^*(\omega) = J'(\omega) - iJ''(\omega) = \frac{1}{M^*(\omega)} , \quad (8.8)$$

it is in fact the compliance, not the modulus, that is directly related to the density correlation function [Wang] which MCT predictions are based on. Certain MCT predictions, like the behavior of the relaxation time close to  $T_c$  or the  $\alpha$ -coupling discussed in the previous chapter, may be analyzed in terms of modulus or compliance because the information content is essentially the same (the relaxation time recovered from the modulus is merely shifted by about a factor of 2 from the compliance value). But the predicted scaling laws, particularly those relating fast and slow relaxation given by power law behavior in the susceptibility spectrum (see Eqs. 6.20-6.25), should only be tested using the complex compliance. In Fig. 8.3 we present, for selected temperatures to avoid an overly crowded figure, the broadband longitudinal compliance for DC704 as a function of real frequency ( $\omega/2\pi$ ) with the real part in the top panel and the imaginary part in the bottom panel. Features similar to what was seen in dielectric spectra (see Fig. 6.2) are observed, most notably the  $\alpha$ -relaxation peak in the imaginary part and corresponding step in the real part.

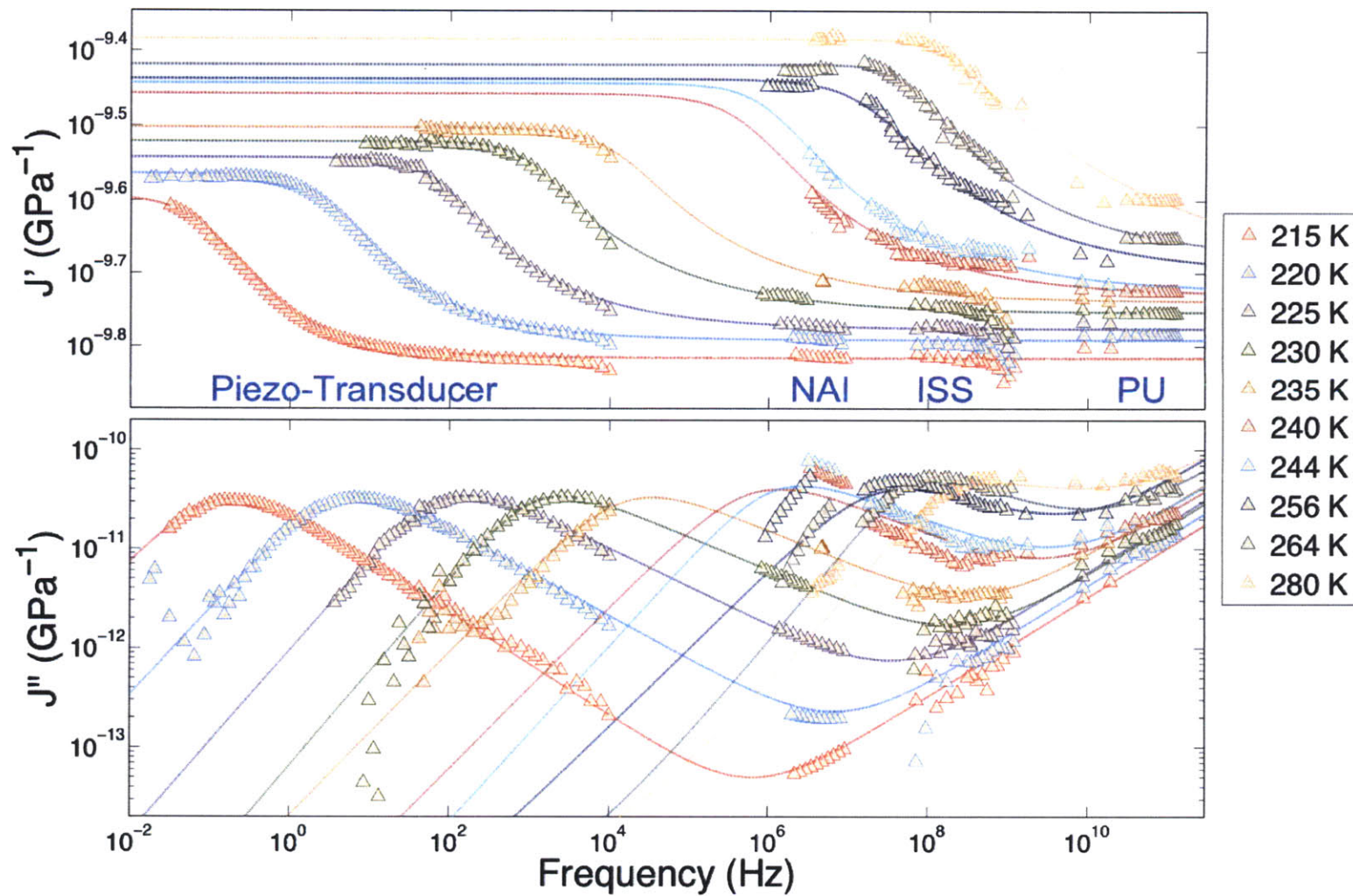


Fig. 8.3 Broadband Longitudinal Compliance for the glass former DC704 from combined from piezo-transducer [Hecksher], NAI, ISS [Torchinsky], and picosecond ultrasonic (PU) [Klieber] data. The top panel shows the real (reactive) part and the bottom panel shows the imaginary (dissipative) part. The solid lines are calculated from fits to the Havriliak- Negami function.

Labels, as well as small gaps between groups of points, mark data collected via the various techniques. Even with the addition of the NAI data, there still exists a moderately sized gap between 10 kHz and 1 MHz. Work is currently underway to improve the data analysis of the piezo-transducer measurements to extend the range to 100 kHz, and to additionally add data points using transducer resonances between 100 kHz and 1 MHz. Even with the current gap in frequency content, the  $\alpha$ -relaxation features are very broad and smooth; we don't anticipate any out-of-the-ordinary-behavior happening at the missing frequencies. Interestingly, the dielectric data showed another corresponding step to go along with the high frequency peak in the imaginary part, but here we observe not even the beginnings of a corresponding change in the real part of the acoustic compliance. To extract a temperature-dependent relaxation time we have fit the spectra to the HN function, but we have added a power law  $\omega^a$  to the imaginary part to account for the high frequency loss.

In Fig. 8.4 we present a number of plots showing the results from the fits. The main panel (8.4.a) shows the temperature dependence of the relaxation time, changing over 10 orders of magnitude from low temperature to high temperature. The higher sensitivity of relaxation time to temperature at low temperatures characteristic of all "fragile" liquids is apparent. In (b) we show how the fit values of the infinite and zero frequency speeds of sound compare with those measured at the highest and lowest frequencies [Klieber]. We see significant departure at higher temperatures that could indicate the presence of dispersion due to a high frequency relaxation process even at room temperature, or it likely illustrates a shortcoming of the phenomenological Havriliak-Negami fitting function. In (c) we plot the fit HN spectral parameters  $\alpha$  and  $\beta$  as a function of temperature. Neither displays much sensitivity to temperature with relatively small changes as temperature increases. This lack of temperature dependence of the spectral parameters is what accounts for the small spread in data in the TTS plot (d). This plot, obtained by shifting the frequency axis by the inverse relaxation time and dividing the real and imaginary parts by the infinite frequency modulus, we observe that time-temperature

superposition is generally obeyed .

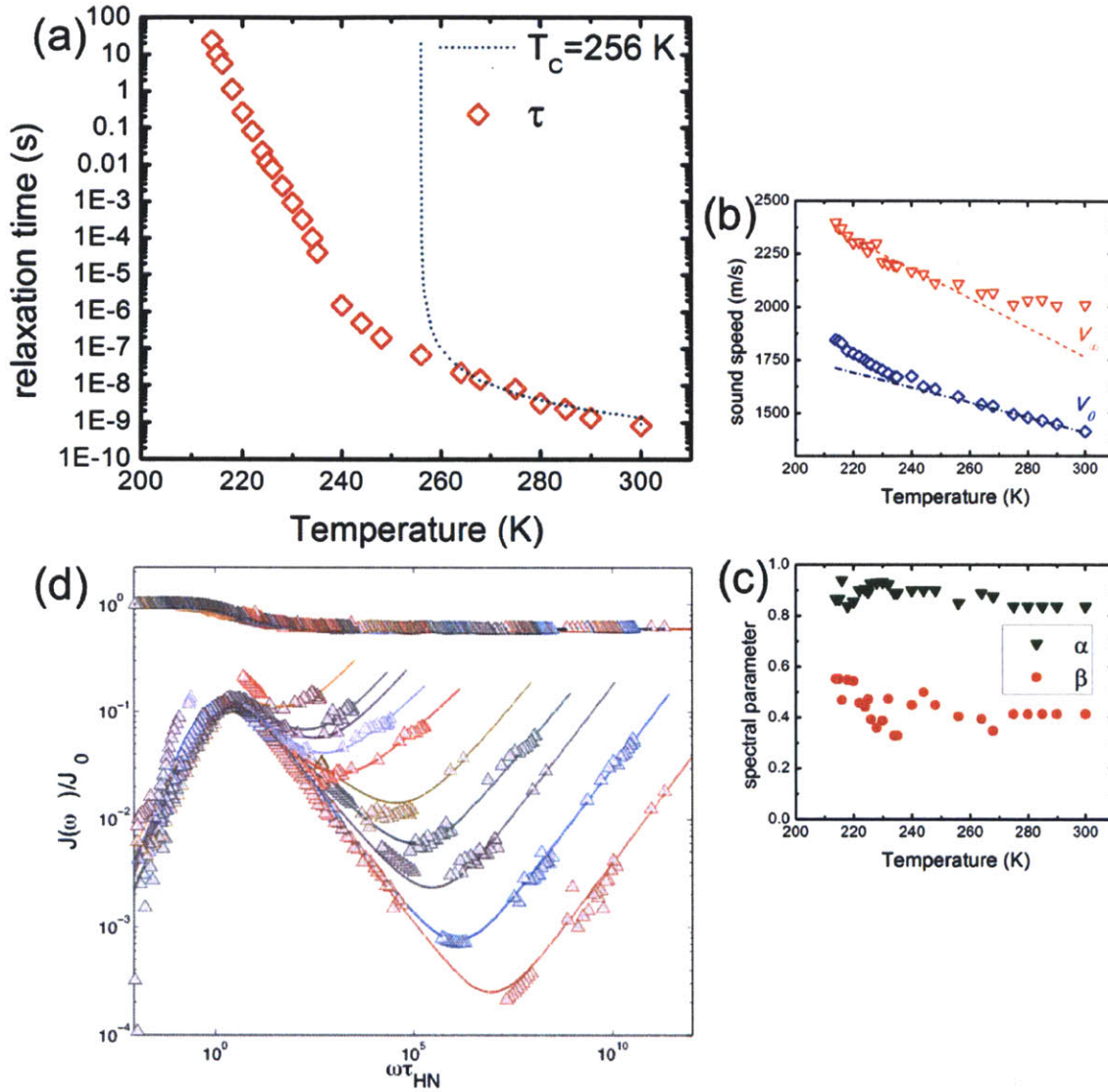


Fig. 8.4 (a) Relaxation time extracted from HN fits. The dashed and dotted lines show fits to Eq. 8.10 with a  $T_c$  value of 256 K respectively. (b) Values of  $v_\infty$  and  $v_0$  recovered from the fits. The dashed lines show a linear fit from values measured at the highest and lowest frequencies [Klieber]. (c) Temperature dependence of HN spectral parameters  $\alpha$  and  $\beta$ . (d) TTS compliance plot obtained by frequency shifting each temperature trace by the inverse relaxation time, and dividing by  $J_0$ .

### 8.3 Tests of MCT predictions

In the remainder of the chapter we will focus on testing a number of the Ideal MCT predictions introduced in Chapter 6. A few of the equations will be repeated here in identical or similar form to aid the discussion. We will begin by examining the



functional form given in Eq. 6.25 that is predicted to describe the behavior of the minimum between high and low frequency peaks in the imaginary part of the susceptibility (compliance). Essentially this is a mathematical statement that a version of TTS should apply to the susceptibility minimum separate from the  $\alpha$ -relaxation TTS. We fit each trace using Eq. 6.25 to determine the minimum  $J''_{\min}$  and the position of the minimum  $\omega_{\min}$ , as well as critical exponents  $a$  and  $b$ . Using the values recovered from the fits, we plot in Fig. 8.5.a the values of  $a$  and  $b$  as a function of temperature. Close to  $T_C$ ,  $J''_{\min}$  and  $\omega_{\min}$  are predicted to follow the power laws

$$J''_{\min} (\omega_{\min})^2 \propto |T - T_C| \quad \text{and} \quad \omega_{\min}^{2a} \propto |T - T_C|. \quad (8.9)$$

In order to determine the MCT  $T_C$ , in Fig. 8.5.b we plot  $J''_{\min}^2$  and  $\omega_{\min}^{2a}$ . The resulting plots should be linear and the intercepts with the temperature axis give  $T_C$ . We see that the behavior is not linear over all temperatures, but we extrapolate from the linear region at higher temperatures (assuming this is the region just above  $T_C$ ) to recover  $T_C = 257$  K using  $\omega_{\min}$  and a slightly lower value of  $T_C = 255$  K using  $J''_{\min}$  for an average value of 256 K, which is higher than  $T_g = 210$  K [Hecksher]. The agreement in recovered  $T_C$  from both of these power law fits is exceptional.

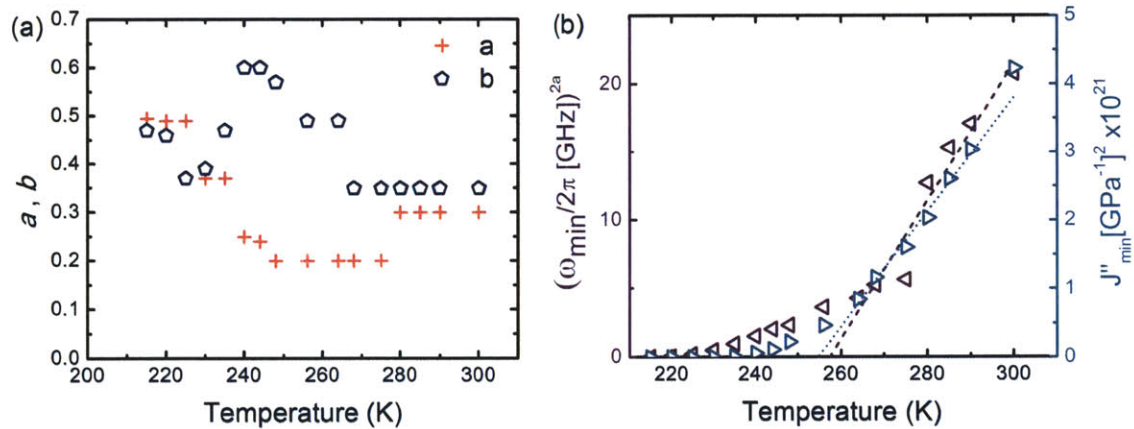


Fig. 8.5 (a) Critical exponents  $a$  and  $b$  from fits of the imaginary compliance minimum to Eq. 6.25. (b) Plots of  $J''_{\min}^2$  and  $\omega_{\min}^{2a}$  in order to recover  $T_C$  from the intercept of a linear fit with the temperature axis. We determine  $T_C = 257$  K using  $\omega_{\min}$  and a slightly lower value of  $T_C = 255$  K using  $J''_{\min}$ .

MCT predicts that close to  $T_C$  the relaxation time will obey a power law

$$\tau(T) \propto |T - T_C|^{-\gamma}, \quad (8.10)$$



where  $\gamma = 1/2a + 1/2b$ . With the fit high temperature  $a$  and  $b$  values and determined  $T_c$  values, we can see if this form offers good agreement with the data over a limited range at high temperatures. Above, in Fig. 8.4.a, the dotted line is calculated using  $\gamma = 1.8$  with  $T_c = 256$  K.

Using the fitted values for  $\omega_{\min}$  and  $J''_{\min}$  we can construct a TTS plot for the compliance minimum to visually see how well TTS is obeyed. We take  $J''$  and shift the frequency by  $\omega_{\min}$  and divide by  $J''_{\min}$ ; the results are shown in Fig. 8.6 where the solid lines are calculated from the values of the fits to Eq. 6.25. Here we clearly see that the data confirm the slightly changing values of the power law exponents with temperature.

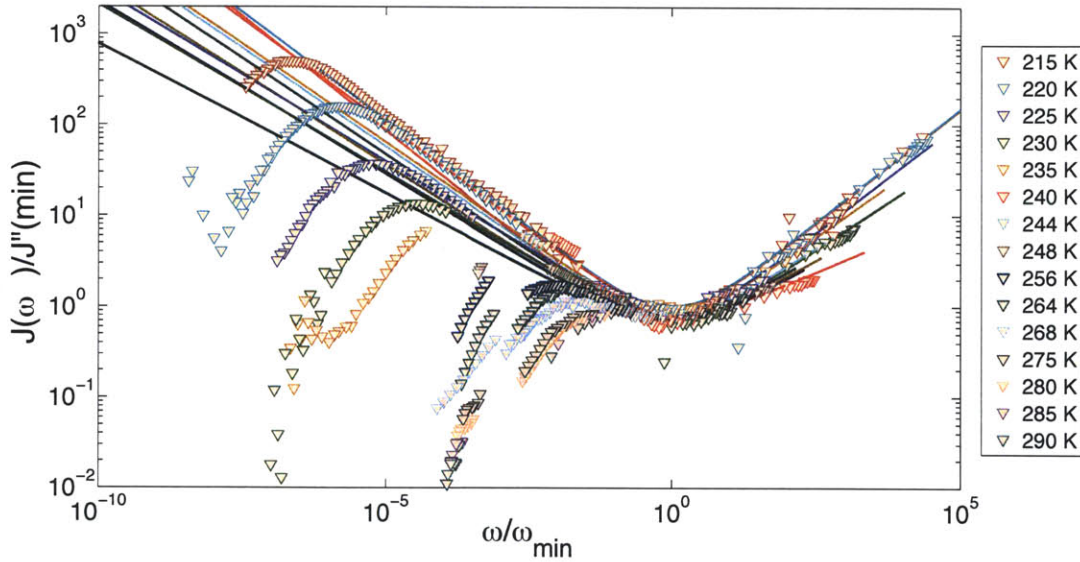


Fig. 8.6. TTS plot of the compliance minimum showing good overlap for all temperatures. The solid lines are calculated from fits to Eq. 6.25.

Finally, we will conclude with an investigation of perhaps the most prominent of MCT predictions: the connection between the fast and slow relaxation given by

$$\lambda = \frac{\Gamma^2(1-a)}{\Gamma(1-2a)} = \frac{\Gamma^2(1+b)}{\Gamma(1+2a)}. \quad (8.11)$$

Using the fit  $a$  and  $b$  exponent values shown in Fig. 8.5.a, we calculate  $\lambda_i$ , where  $i$  indicates  $a$  or  $b$ . The results are shown in Fig. 8.7 and even though they are somewhat noisy, we see that there is relatively good agreement at all temperatures

above 240 K (the difference is  $\sim 0.1$  or less from 240 K to 300 K). The predicted connection between fast and slow relaxation appears to be present in DC704 at temperatures close to and above the determined value of  $T_c$ , which connection previously had remain untested by probes of the mechanical degrees of freedom in any supercooled liquid.

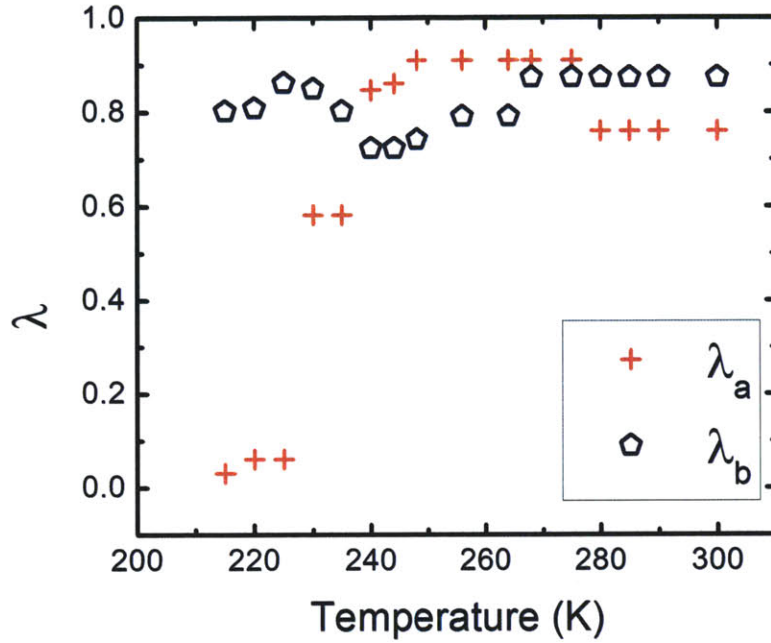


Fig. 8.7 The MCT parameter  $\lambda$  calculated according to Eq. 8.11 using  $a$  and  $b$  exponents from the fits to the compliance minimum. MCT predicts that  $\lambda$  calculated with  $a$  or  $b$  should be equivalent in close to  $T_c$ .

## 8.4 Conclusions

In this chapter we have presented the first ultra-broadband mechanical spectra of a glass forming liquid. We utilized NAI to measure the complex acoustic compliance in the 1-10 MHz frequency range to fill in an important gap in the broadband spectra, and we analyzed the behavior of the  $\alpha$ -relaxation by fitting to the phenomenological HN function. We saw that TTS of the primary  $\alpha$ -relaxation holds, as well as TTS of the compliance minimum as predicted by MCT. Fitting the compliance minimum as a function of temperature produced results confirming the validity of the predicted MCT relationships, most notably the connection between the fast and slow relaxation critical exponents.





# Chapter 9

## High frequency speed of sound in RDX

In this final chapter, we change themes to show more of the versatility ISS offers. We report photoacoustic measurements of the quasi-longitudinal speed of sound along different crystallographic directions in the energetic molecular crystal cyclotrimethylene trinitramine (RDX). Measurements in (100)-oriented RDX were made using two complementary techniques, ISS and picosecond acoustic interferometry (PAI) [Lin], to probe acoustic frequencies in the 0.5 to 15 GHz range in order to resolve large discrepancies in reported sound speed values measured using different techniques and frequency ranges. We will present a short comparison of the ISS and PAI measurements, and to facilitate the discussion, a few equations given in earlier chapters will be repeated.

### 9.1 Background

The mechanisms through which energetic materials undergo initiation of detonation have been the subject of much experimental and theoretical effort [Bdzil, Walley, Zeman]. Mechanical shock induces detonation in many energetic materials, posing challenging questions as to how high-energy, microscopic bond breaking can be triggered by low-energy, long-wavelength acoustic modes, associated more with macroscopic material properties rather than microscopic chemical dynamics. Coupling between acoustic modes and other lattice and molecular degrees of freedom clearly plays a crucial role. This can be revealed in part through frequency-dependent dispersion in the elastic properties, which arises close to acoustic frequencies that coincide with energy relaxation rates of coupled higher-frequency modes. Many energetic materials are molecular crystals with low crystal symmetry and anisotropic mechanical properties. Determination of their frequency-dependent elastic constants is important for modeling of their dynamical responses and may

indicate the extent of interactions between acoustic modes and other degrees of freedom.

A number of methods have been employed to measure the elastic constants in anisotropic crystals in different acoustic frequency ranges from kHz to GHz [Leisure,Brown,Vacher,Every,Maznev99]. Often there is no practical difference between the resulting elastic constants regardless of the experimental frequency range or measurement technique, but recent studies of energetic materials by Brillouin light scattering (BLS) at  $\sim 10\text{-}20$  GHz acoustic frequencies [Haycraft,Stevens10] have yielded intriguing discrepancies with ultrasonic measurements performed at kHz frequencies [Haussühl,Schwarz]. In particular, the longitudinal elastic modulus  $C_{11}$  of RDX measured by BLS [Haycraft] was reported to be 40% higher, whereas  $C_{42}$  was 6 times lower compared to the ultrasonic data [Haussühl,Schwarz].

Some of the reported discrepancies point to a possible relaxation mechanism that would result in dispersion and thus frequency-dependent elastic constants. When relaxation that couples to acoustic modes, for example vibrational relaxation in molecular gases [Herzfeld] and liquids [Rubio] or structural relaxation in supercooled liquids (see previous chapters), is on a time scale much faster than the acoustic period, the acoustic wave will propagate as if there is no coupling of modes. But when the relaxation time becomes coincident with or slower than the acoustic period, coupling will result in acoustic dispersion. The speed of sound at high frequencies ( $\omega\tau \gg 1$ ) will be different than the speed of sound at low frequencies ( $\omega\tau \ll 1$ ). For the simplest case of a single exponential (Debye) relaxation, the dispersive region will span more than one decade in frequency.

The discrepancies in RDX elastic constants led Sun *et al.* [Sun] to address the issue of potential relaxation-induced acoustic dispersion by determining the elastic constants at an intermediate frequency of  $\sim 450$  MHz using ISS [Nelson82]. The ISS-determined elastic constant values were essentially identical to the ultrasound results and significantly different from the BLS results. However, the acoustic

frequency of the ISS measurements was too low to conclusively rule out the possibility of relaxation coupling to GHz frequency acoustic waves in RDX. The confirmation of such dispersion in energetic materials could lead to deeper understanding of energy transfer pathways involved in the initiation of detonation, thus emphasizing the need for a number of experimental methods that together continuously cover a broad range of frequencies from the kHz to THz ranges, essentially across the entire Brillouin zone. In this work, we take steps in this direction by utilizing ISS and PAI to measure the quasi-longitudinal speed of sound in single crystal RDX at acoustic frequencies spanning the frequency gap between previous ISS [Sun] and BLS [Haycraft] measurements.

In BLS, ISS, and PAI, the detection mechanism results from inelastic light scattering off of acoustic modes. In contrast to BLS that probes incoherent thermally populated acoustic phonons, both ISS and PAI rely on the generation of coherent acoustic waves. In ISS, coherent acoustic phonons of a well-defined wavevector with typical frequency range from MHz to low GHz are generated by crossing laser beams inside a sample. In PAI, a laser beam is focused onto a thin metal film coated on the sample surface that acts as an acoustic transducer, launching an acoustic wavepacket with frequency components potentially up to hundreds of GHz into the sample. The specific details of each of our current measurements are described below.

## **9.2 Experimental methods**

### **9.2.a Sample preparation**

RDX crystals have an orthorhombic structure (*Pbca* space group, nine independent elastic constants), with lattice parameters  $a = 1.3182$  nm,  $b = 1.1574$  nm, and  $c = 1.0709$  nm, and a density of  $1.806$  g/cm<sup>3</sup> [Choi]. Single crystal samples were prepared at the Los Alamos National Laboratory Energetic Materials Crystal Laboratory, as previously described in detail [Hooks]. Briefly, the RDX crystals were grown by evaporation using an acetone solution reflux technique. The crystals were oriented to 1.85 degrees from (100) normal using X-ray diffraction and were cut



into thin ( $\sim 1$  mm) slabs with a diamond wire saw. The slabs were polished to an optical finish using aluminum oxide slurry ( $1\text{ }\mu\text{m}$  final grit size) in aqueous detergent. For PAI measurements, a thin ( $\sim 100$  nm) gold film was deposited by thermal evaporation on the surface of the RDX crystal.

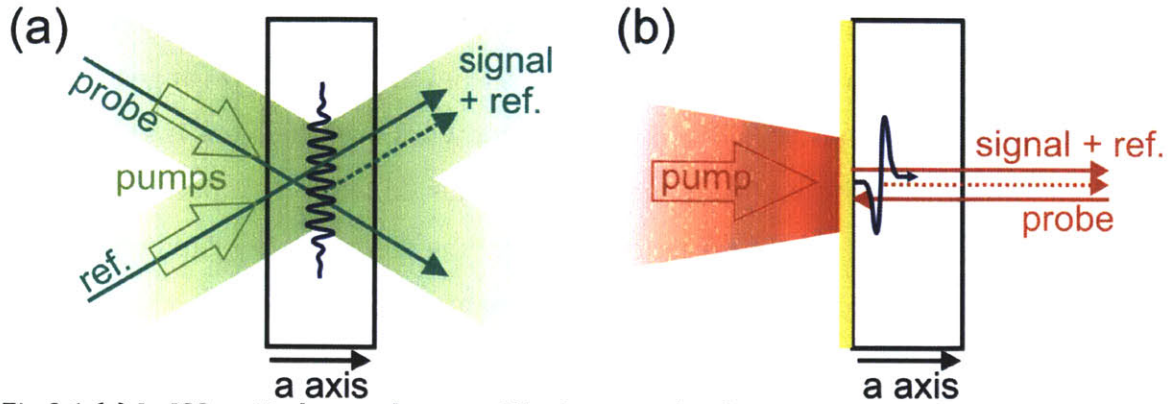


Fig 9.1 (a) In ISS, optical pump beams with picosecond pulses were crossed to create a spatially periodic, temporally impulsive driving force that launches acoustic waves in the RDX bc-plane. CW probe light diffracted from the acoustic waves was combined with a reference beam and directed to a detector. (b) In PAI, a short pump pulse was focused onto a thin gold transducer. Heating and thermal expansion launched a broadband acoustic strain pulse into the RDX along the a axis. A variably delayed femtosecond probe pulse was partially reflected off the acoustic strain pulse and directed to a detector along with light reflected from the gold film that served as a reference beam.

### 9.2.b ISS technique

Impulsive stimulated light scattering has been described in more detail previously [Nelson,Sun]. In the present ISS experiments, a short-pulsed excitation laser beam ( $\lambda_e = 515$  nm, 60 ps pulse width), derived through second harmonic generation of the amplified Yb:KGW laser system, was split with a diffractive optic into two beams, which passed through a two-lens telescope and were focused to a  $300\text{ }\mu\text{m}$   $1/e$  beam radius and crossed with external angle  $\theta$  in the sample as depicted in Fig. 9.1.a. Interference between the two beams created a spatially periodic intensity and absorption pattern with the interference fringe spacing

$$L = 2\pi/q = \lambda_e/(2\sin(\theta_e/2)). \quad (9.1)$$

Laser-induced electrostriction (i.e. impulsive stimulated Brillouin scattering [Yan]) as well as periodic absorption, heating, and rapid thermal expansion (impulsive stimulated thermal scattering [Rogers]) generated coherent, counter-propagating

acoustic waves with the wavelength  $L$  and wavevector magnitude  $q$ . The thermal expansion-induced driving force depends on the absorption at the pump wavelength, while the electrostrictive driving force depends on the relevant photoelastic constants and scales with wavevector [Nelson]. For the highest wavevectors in our current measurements, the electrostrictive force dominates, while at lower wavevectors it accounts for less than half of acoustic wave generation. Strain-induced changes in the refractive index due to the acoustic waves gave rise to time-dependent diffraction (i.e. coherent scattering) of an incident continuous wave probe beam ( $\lambda_p = 532$  nm, 150  $\mu$ m beam radius). The probe beam was split into two parts (probe and reference) which were recombined at the sample (focused to 150  $\mu$ m beam radius) by the same diffractive optic and two-lens telescope used for the excitation beams, ensuring that the probe beam was incident on the spatially periodic acoustic wave “grating” at the Bragg angle for diffraction and that the diffracted signal was superposed with the reference beam for heterodyne detection [Maznev1998]. Thus Eq. 9.1 holds for excitation parameters as well as the probe and reference wavelength  $\lambda_p$  and angle of intersection  $\theta_p$  (i.e. scattering angle). The signal and reference beams were directed to a fast detector and the time-dependent acoustic oscillations were recorded on an oscilloscope.

### 9.2.c PAI technique

The sound velocity at  $\sim 15$  GHz was obtained using picosecond acoustic interferometry (PAI) [Lin] as depicted in Fig. 9.1.b. A  $\sim 100$ -nm gold film was deposited onto one face of a (100) RDX crystal. Laser light from an amplified Ti:Sapphire system (Coherent RegA,  $\lambda = 790$  nm, 300 fs pulse duration, 250 kHz repetition rate) was split into excitation and variably delayed probe beams. The excitation beam was attenuated to 6 mW to reduce sample heating and focused to a 45  $\mu$ m beam radius on the free surface of the gold film, which due to rapid heating and thermal expansion acted as a transducer launching an acoustic wavepacket with broadband frequency components that propagated into the RDX along the  $a$ -axis.

The probe beam, attenuated to 3 mW, entered the crystal at normal incidence and was focused to the back surface of the gold film to a 25  $\mu\text{m}$  beam radius. The probe reflection from the gold film (reference beam) interfered with coherent backscattering signal light from the acoustic wave as it propagated through the sample, creating a time-dependent oscillation in the intensity of the reflected beam at the detected acoustic frequency. The signal and reference light were directed to a photodetector and the signal was collected with a lock-in amplifier at the frequency of an acousto-optic chopper in the excitation beam. The probe wavelength and scattering angle selected a well defined acoustic wavelength given by

$$L = 2\pi/q = \lambda_p / (2n \sin(\theta_p/2)) , \quad (9.2)$$

where  $\lambda_p$  is the probe wavelength,  $\theta_p$  is the internal scattering angle, and  $n$  is the refractive index. We note that Eq. 9.2, which determines the acoustic wavelength probed in PAI, is similar to Eq. 9.1, which determines the acoustic wavelength in ISS. The only difference is that in PAI the probe beam enters and leaves the crystal from the same face so the refractive index must be accounted for in relating the acoustic wavelength in the crystal to the optical wavelength in air. In ISS this is not necessary because refraction of the incident beams as they enter the crystal compensates for the shorter light wavelengths in the crystal, yielding the same interference fringe-spacing in the crystal as would be produced in the air. The acoustic wavelength probed in PAI through coherent backscattering could be generated through ISS measurements with counter-propagating excitation beams entering the crystal from opposite faces, but it is more convenient to conduct ISS measurements with all the beams entering the same crystal face (yielding a minimum acoustic wavelength of about 1  $\mu\text{m}$  in practice). We thus conduct PAI measurements to probe the smallest PAI wavelength (highest frequency) of  $L = \lambda_p / 2n$ . PAI measurements can be conducted with smaller probe scattering angles to select longer wavelengths and lower frequency components of the photo-induced broadband acoustic wavepacket, but experimental difficulties arise at small internal angles. Due to these details, PAI and ISS are complementary techniques for

accessing acoustic wavelength ranges of 250-350 nm and 1-100  $\mu\text{m}$  respectively with our current pump and probe wavelengths.

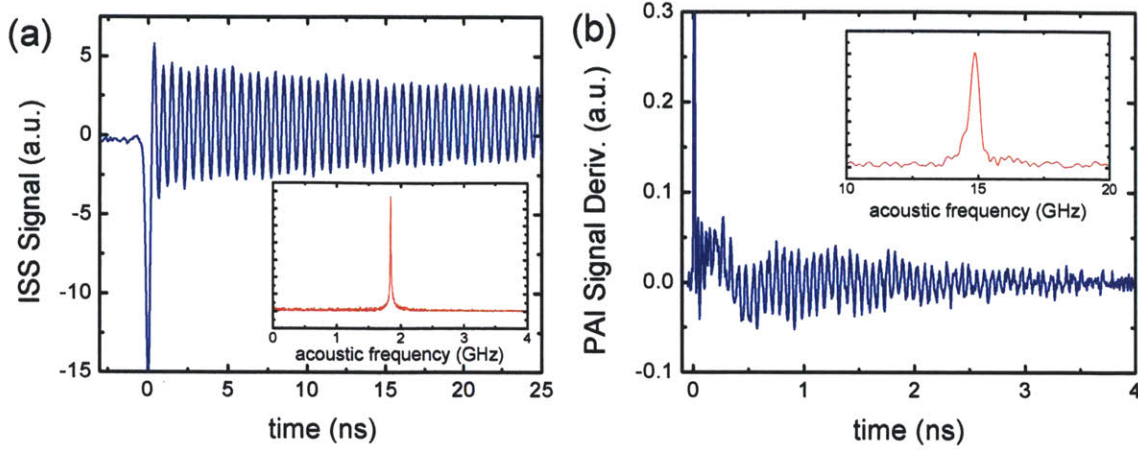


Fig. 9.2 (a) Example of ISS signal. At  $t=0$  pump beams crossed in the sample generating 1.8  $\mu\text{m}$  wavelength acoustic waves. The inset shows the Fourier transform of the data displaying a sharp peak 1.85 GHz. (b) Time derivative of PAI signal. The signal derivative minimizes the large thermoreflectance background so acoustic oscillations are apparent. The inset shows a peak in the Fourier domain at 14.9 GHz.

### 9.3 Results and discussion

Fig. 9.2.a shows ISS data recorded with an acoustic wavelength of 1.8  $\mu\text{m}$ . At  $t = 0$ , the pump pulses were crossed in the sample, generating a spike due to instantaneous non-resonant electronic responses, followed by damped acoustic oscillations. The inset shows the Fourier transform of the data giving a very sharp peak just below 2 GHz. For quantitative analysis, the data were fit in the time domain to a damped sinusoid to recover the acoustic frequency  $\nu$ , and the quasi-longitudinal speed of sound  $V = \nu L$  was determined using the experimentally set acoustic wavelength  $L$  given in Eq. 9.1. In practice the acoustic wavelength was ascertained from the binary phase mask period and the two-lens telescope imaging. The previous ISS measurements were all conducted with an imposed wavelength of 7.2  $\mu\text{m}$  corresponding roughly (depending on the speed of sound along a particular direction in the anisotropic crystal) to a longitudinal frequency of 450 MHz. To achieve higher acoustic frequencies, we collected data with ten acoustic wavelengths ranging from 6.6  $\mu\text{m}$  down to 1.0  $\mu\text{m}$  corresponding to acoustic frequencies from 490 MHz to 3.4 GHz. Data were collected with a number of



different wavevectors corresponding to acoustic waves traveling along different directions in the bc plane.

Fig. 9.2.b shows the time-derivative of the PAI signal. Laser heating-induced changes in reflectivity of the transducer lead to a large thermal background that can be minimized by taking the derivative of the signal. The inset shows a strong peak at 14.9 GHz in the Fourier transform. The speed of sound  $V$  was determined by  $V = \nu L$  using the acoustic wavelength given in Eq. 9.2 with  $\theta_p = 180$  degrees and  $n(790 \text{ nm}) = 1.56$ . Linear extrapolation of refractive index data in the visible region (450–670 nm) [McCrone] was used to estimate  $n$  at the probe wavelength. The lack of absorption bands in the visible [Whitley] and the small index variation observed in this wavelength range validate this procedure.

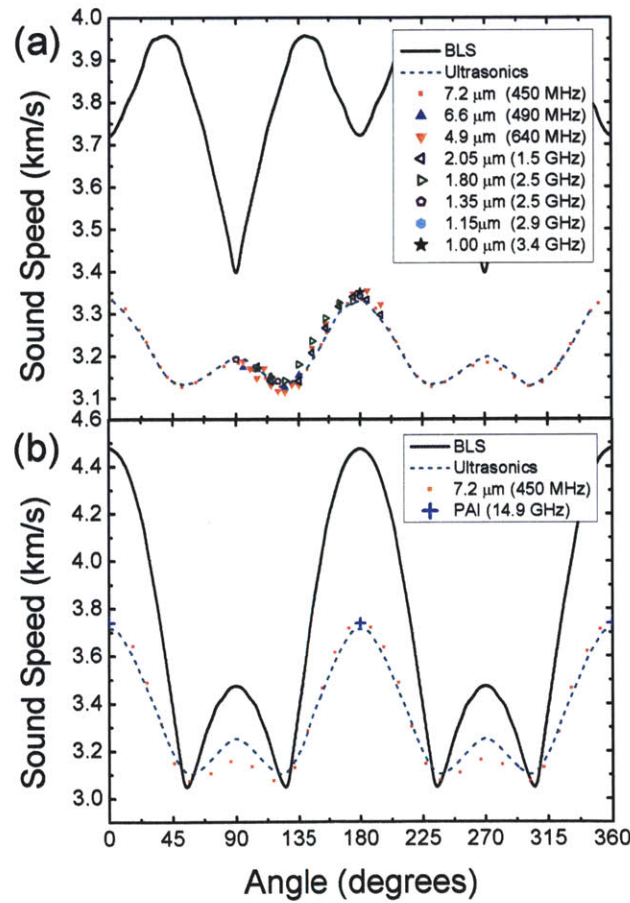


Fig. 9.3 (a) ISS and (b) PAI measured quasi-longitudinal speed of sound along different crystal axes of RDX together with previously published ISS (small squares) [Sun],

ultrasonics (dashed line), and BLS data (solid line) [Haycraft]. Degrees are counted from the b-axis in (a) and from the a-axis in (b).

In Fig. 9.3 we present digitized data from [Sun] and [Haycraft] alongside our new ISS and PAI results. We see that for all acoustic wavelengths and frequencies there is good agreement with previously measured speeds of sound from ISS and ultrasonic [Schwarz] techniques. For example, using ISS we measure an acoustic frequency of 2.91 GHz at acoustic wavelength  $1.15\text{ }\mu\text{m}$  along the b-axis (180 degrees in Fig. 9.3.a), corresponding to a speed of sound of 3350 m/s, which is very close to 3340 m/s from [Sun] and [Schwarz]. PAI along the a-axis (180 degrees in Fig. 9.3.b) determines the speed of sound to be 3790 m/s at 14.9 GHz, also in good agreement with 3750 m/s from [Sun] and 3700 m/s from [Schwarz]. Our data do not suffice for the determination of the full set of elastic constants of RDX at any given frequency; however, close agreement with previous ISS and ultrasonic data at all frequencies and directions measured suggests that other crystal orientations and directions should also yield similar results and elastic constant values. In contrast, we see significant disagreement between our ISS and PAI data and the reported BLS results. For example, [Haycraft] reports much higher values of the speed of sound: 3750 m/s for the b-axis and 4500 m/s for the a-axis.

Altogether, we observe good agreement between previously measured anisotropic speeds of sound [Haussühl, Schwarz, Sun] from acoustic frequencies of 100 kHz up to 450 MHz and our new ISS and PAI results from 490 MHz up to 14.9 GHz. The lack of acoustic dispersion is strong evidence against any kind of relaxation process coupling significantly to acoustic waves in this frequency range. We are not certain of the reason for the disagreement between these results and the reported BLS results [Haycraft].

## 9.4 Conclusions

Discrepancies in the reported speeds of sound in RDX from BLS and other techniques have prompted the discussion of possible relaxation processes coupling

to acoustic waves at high frequencies. We report new measurements made using ISS and PAI spanning acoustic frequencies from 490 MHz up to 14.9 GHz. These results are in agreement with previous ultrasonics and ISS measurements [Haussühl,Schwarz,Sun] at lower frequencies. The lack of acoustic dispersion is persuasive evidence that there is no relaxation process that couples significantly to linear acoustic waves in RDX at acoustic frequencies from 100 kHz up to 15 GHz.

Although we have extended measurements of the speed of sound in RDX to cover acoustic frequencies over six orders of magnitude, these results do not rule out the possibility of an internal molecular relaxation process coupling to acoustic waves at higher frequencies. Nor do they shed light on potential coupling of large amplitude non-linear acoustic and shock waves to molecular modes that would be involved in detonation. Extending acoustic measurements of energetic materials to higher frequencies (up to THz) as well into the non-linear acoustic and shock domains presents exciting challenges for future research.







## Bibliography

- [Adams] J. H. Adams, G. Gibbs. On the temperature dependence of cooperative relaxation properties in glass-forming liquids. *J. Chem. Phys.* **43**, 139 (1965).
- [Ahluwalia] R. Ahluwalia, S. P. Das. *Phys. Rev. E* **57**, 5771 (1998).
- [Angell85] C. A. Angell. *Relaxation in Complex Systems*, eds. K. L. Ngai, G. B. Wright (US Dept. Commerce, Springfield, 1985).
- [Angell95] C. A. Angell. Formation of glasses from liquids and biopolymers. *Science* **267**, 1924 (1995).
- [Angell00] C. A. Angell, K. L. Ngai, G. B. McKenna, P. F. McMillan, S. W. Martin. Relaxation in glassforming liquids and amorphous solids. *J. Appl. Phys.* **88**, 3113 (2000).
- [Ashcroft] N. W. Ashcroft, N. D. Mermin. *Solid State Physics*. (Saunders College Publishing, Orlando, 1976).
- [Azzimani] A. Azzimani, C. Dreyfus, R. M. Pick, P. Bartolini, A. Taschin, R. Torre. Analysis of a heterodyne-detected transient-grating experiment on a molecular supercooled liquid. II Application to *m*-toluidine. *Phys. Rev. E* **76**, 011510 (2007).
- [Balucani] U. Balucani, M. Zoppi. *Dynamics of the Liquid State*. (Oxford University Press, 1995).
- [Bdzil] J. B. Bdzil, D. S. Stewart. The dynamics of detonation in explosive systems. *Annu. Rev. Fluid Mech.* **39**, 263 (2007).
- [Bengtzelius] U. Bengtzelius, W. Götze, A. Sjölander. Dynamics of supercooled liquids of the glass transition. *J. Phys. C: Sol. State Phys.* **17**, 5915 (1984).
- [Berne] B. J. Berne, R. Pecora. *Dynamic Light Scattering with Applications to Chemistry, Biology, and Physics*. (Dover Publications, Mineola, NY, 2000).
- [Blakemore] J.S. Blakemore, *Solid State Physics* (Cambridge University Press, Cambridge, 1985).
- [Blanshard] J. M. V. Blanshard, P. Lilford, eds. *The Glassy State in Foods*. (Nottingham Univ. Press, Nottingham, 1993).
- [Bloembergen] N. Bloembergen. *Nonlinear Optics* (Benjamin, New York, 1965).
- [Boon] J. P. Boon, S. Yip. *Molecular Hydrodynamics*. (Dover Publications, New York, 1980).

- [Brodin] A. Brodin, E. A. Rössler. Depolarized light scattering versus optical Kerr effect spectroscopy of supercooled liquids: Comparative analysis. *J. Chem. Phys.* **125**, 114502 (2006).
- [Broido] D. A. Broido, M. Malorny, G. Birner, N. Mingo, and D. A. Stewart, *Appl. Phys. Lett.* **91**, 231922 (2007).
- [Brown] J. M. Brown, E. H. Abramson, R. J. Angel. Triclinic elastic constants for low albite. *Phys. Chem. Minerals* **33**, 256 (2006).
- [Brüesch] P. Brüesch. *Phonons: Theory and Experiment III*. (Springer, London, 1987).
- [Burns] G. Burns, *Solid State Physics* (Academic Press, Orlando, 1985).
- [Böhmer] R. Böhmer, G. Diesemann, G. Hinze, E. A. Rössler. Dynamics of supercooled liquids and glassy solids. *Prog. Nuc. Mag. Res. Spect.* **39**, 191 (2001).
- [Cahill90] D. G. Cahill. Thermal conductivity measurement from 30 to 750 K: the  $3\omega$  method. *Rev. Sci. Instrum.* **61**, 802 (1990).
- [Cahill03] D. G. Cahill, W. K. Ford, K. E. Goodson, G. D. Mahan, A. Majumdar, H. J. Maris, R. Merlin, S. R. Phillpot. Nanoscale thermal transport. *J. Appl. Phys.* **93**, 793 (2003).
- [Callaway] J. Callaway, *Phys. Rev.* **113**, 1046–1051 (1959).
- [Capinski] W. S. Capinski, H. J. Maris. Improved apparatus for picosecond pump-and-probe optical measurements. *Rev. Sci. Instrum.* **67**, 2720 (1996).
- [Carslaw] H. S. Carslaw, J. C. Jaeger. *Conduction of Heat in Solids*. (Oxford University Press, Oxford, 1986).
- [Chappell] P. J. Chappell, D. Kivelson. *J. Chem Phys.* **76**, 1742 (1982).
- [Chen98] G. Chen, *Phys. Rev. B* **57**, 14958 (1998).
- [Chen03] G. Chen, M. S. Dresselhaus, G. Dresselhaus, J. -P. Fleurial, T. Caillat. Recent developments in thermoelectric materials. *Inter. Mater. Rev.* **48**, 45 (2003).
- [Chen05] G. Chen, *Nanoscale Energy Transport and Conversion* (Oxford University Press, New York, 2005).
- [Chiao] R. Y. Chiao, C. H. Townes, B. P. Stoicheff. Stimulated Brillouin Scattering and Coherent Generation of Intense Hypersonic Waves. *Phys. Rev. Lett.* **12**, 592 (1964).
- [Choi] C. S. Choi, E. Prince. The crystal structure of cyclotrimethylene triamine. *Acta Cryst.* **B28**, 2857 (1972).

- [Christensen] T. Christensen, N. Olsen. Determination of the frequency-dependent bulk modulus of glycerol using a piezoelectric spherical shell. *Phys. Rev. B* **49**, 15396 (1994).
- [Christensen07] T. Christensen, N. B. Olsen, J. C. Dyre. Conventional methods fail to measure  $c_p(\omega)$  of glass-forming liquids. *Phys. Rev. E* **75**, 041502 (2007).
- [Cohen] M. H. Cohen, D. Turnbull. Molecular transport in liquids and glasses. *J. Chem. Phys.* **31**, 1164 (1959).
- [Collier] R. J. Collier, C. B. Burckhardt, L. H. Lin. *Optical Holography*. (Academic Press, 1971).
- [CRC] D. R. Lide, editor. *CRC Handbook of Chemistry and Physics, Internet Version 2011*. Taylor & Francis, Boca Raton, FL, 91<sup>st</sup> Edition, 2011.
- [Cucini ] R. Cucini, F. Bencivenga, and C. Masciovecchio. All-reflective femtosecond optical pump–probe setup for transient grating spectroscopy. *Opt. Lett.* **36**, 1032 (2010).
- [Das86] S. P. Das, G. F. Mazenko. Fluctuating nonlinear hydrodynamics and the liquid-glass transition. *Phys. Rev. A* **34**, 2265 (1986).
- [Das04] S. P. Das. Mode-coupling theory and the glass transition in supercooled liquids. *Rev. Mod. Phys.* **76**, 785 (2004).
- [Das09] S. P. Das, G. F. Mazenko. Fluctuating nonlinear hydrodynamics does not support an ergodic-nonergodic transition. *Phys. Rev. E* **79**, 021504 (2009).
- [Debenedetti] P. G. Debenedetti, F. H. Stillinger. Supercooled liquids and the glass transition. *Nature*. **410**, 259 (2001).
- [Dresselhaus] M. S. Dresselhaus, G. Chen, M. Y. Tang, R. Yang, H. Lee, D. Wang, Z. Ren, J. –P. Fleurial, P. Gogna. New Directions for Low-Dimensional Thermoelectric Materials. *Adv. Mater.* **19**, 1043 (2007).
- [Dreyfus] C. Dreyfus, A. Aouandi, R. M. Pick, T. Berger, A. Patkowski, W. Steffen. *Eur. Phys. J. B* **9**, 401 (1999).
- [Dyre96] J. C. Dyre, N. B. Olsen, T. Christensen. Local elastic expansion model for viscous-flow activation energies of glass-forming molecular liquids. *Phys. Rev. B* **53**, 2171 (1996).
- [Dyre06] J. C. Dyre, T. Christensen, N. B. Olsen. Elastic models for the non-Arrhenius viscosity of glass-forming liquids. *J. Non-Crystal. Solids* **352**, 4635 (2006).
- [Eichler] H.J. Eichler, P. Günter, and D. W. Pohl, *Laser-Induced Dynamic Gratings* (Springer, Berlin, Heidelberg, 1986).

- [Every] A. G. Every. Measurement of the near-surface elastic properties of solids and thin supported films. *Meas. Sci. Technol.* **13**, R21 (2002).
- [Ferrer] M. L. Ferrer, C. Lawrence, B. G. Demirjian, D. Kivelson, C. Alba-Simionesco, G. Tarjus. *J. Chem. Phys.* **109**, 8010 (1998).
- [Ferry] J. D. Ferry. *Viscoelastic Properties of Polymers*, 3<sup>rd</sup> ed. (Wiley, New York, 1980).
- [Fletcher] L. S. Fletcher. Recent Developments in Contact Conductance Heat Transfer. *J. Heat Transfer* **110**, 1059 (1988).
- [Fourkas] J. T. Fourkas, M. D. Fayer. The Transient Grating: A Holographic Window to Dynamic Processes. *Acc. Chem. Res.* **25**, 227 (1992).
- [Frenkel] J. Frenkel. *Kinetic Theory of Liquids*. (Dover Publications, New York, 1955).
- [Fuchs] K. Fuchs, Proc. Cambridge Philos. Soc. **34**, 100 (1938).
- [Gedik] N. Gedik and J. Orenstein. Absolute phase measurement in heterodyne detection of transient gratings, *Opt. Lett.* **29**, 2109 (2004).
- [Gibbs] E. A. Gibbs, J. H. DiMarzio. Nature of the glass transition and the glassy state. *J. Chem. Phys.* **28**, 373 (1958).
- [Glorieux02] C. Glorieux, K. A. Nelson, G. Hinze, M. D. Fayer. Thermal, structural, and orientational relaxation of supercooled liquids studied by polarization-dependent impulsive stimulated scattering. *J. Chem. Phys.* **116**, 3384 (2002).
- [Glorieux04] C. Glorieux, J.D. Beers, E. H. Bentefour, K. Van de Rostyne, K. A. Nelson. Phase mask based interferometer: Operation principle, performance, and application to thermoelastic phenomena. *Rev. Sci. Instr.* **75**, 2906 (2004).
- [Goldman] J. R. Goldman, J. A. Prybyla. *Phys. Rev. Lett.* **72**, 1364 (1994).
- [Goodno] G. D. Goodno, G. Dadusc, and R. J. D. Miller, *J. Opt. Soc. Am. B* **15**, 1791 (1998).
- [Gostein] M. Gostein, M. Banet, M. Joffe, A.A. Maznev, R. Sacco, J.A. Rogers, K.A. Nelson, "Thin film metrology using impulsive stimulated thermal scattering (ISTS)", in *Handbook of Silicon Semiconductor Metrology*, ed. A.C. Diebold (New York: Marcel Dekker. 2001).
- [Govorkov] S. Govorkov, W. Ruderman, M. W. Horn, R. B. Goodman, M. Rothschild. A new method for measuring thermal conductivity of thin films. *Rev. Sci. Instrum.* **68**, 3828 (1997).
- [Greer] A. L. Greer. Metallic Glasses. *Science* **267**, 1615 (1995).

- [Götze88] W. Götze, L. Sjögren. Scaling properties in supercooled liquids near the glass transition. *J. Phys. C: Sol. State Phys.* **21**, 3407 (1988).
- [Götze99] W. Götze. Recent tests of the mode-coupling theory for glassy dynamics. *J. Phys.-Cond. Matt.* **11**, A1 (1999).
- [Halalay] I. C. Halalay, K. A. Nelson. Improved sample cell design for optical studies of glass-forming liquids in the 4-530 K range. *Rev. Sci. Instr.* **61**, 3623 (1990).
- [Halalay92] I. C. Halalay, K. A. Nelson. Time-resolved Spectroscopy and Scaling Behavior in LiCl/H<sub>2</sub>O near the Liquid-Glass Transition. *Phys. Rev. Lett.* **69**, 636 (1992).
- [Harata90] A. Harata, H. Nishimura, T. Sawada. Laser-induced surface acoustic waves and photothermal surface gratings generated by crossing two pulsed laser beams. *Appl. Phys. Lett.* **57**, 132 (1990).
- [Harata98] A. Harata, N. Adachi, T. Sawada. Subnanosecond transient-reflecting-grating measurements and depth-profiling analysis of mesoscopic subsurface properties of a nickel single crystal. *Phys. Rev. B* **58**, 7319 (1998).
- [Hatta] I. Hatta, Y. Sasuga, R. Kato, A. Maesono. Thermal diffusivity measurement of thin films by means of an ac calorimetric method. *Rev. Sci. Instrum.* **56**, 1643 (1985).
- [Haussühl] S. Haussühl. Elastic and thermoelastic properties of selected organic crystals. *Z. Kristallogr.* **216**, 339 (2001).
- [Havriliak] S. Havriliak, S. Negami. A complex plane representation of dielectric and mechanical relaxation processes in some polymers. *Polymer* **8**, 161 (1967).
- [Haycraft] J. J. Haycraft, L. L. Stevens, C. J. Eckhardt. The elastic constants and related properties of the energetic material cyclotrimethylene triamine (RDX) determined by Brillouin scattering. *J. Chem. Phys.* **124**, 024712 (2006).
- [Hecksher] T. Hecksher. PhD Thesis. (Roskilde University, 2010).
- [Henry] A. Henry and G. Chen, *J. Comp. Theor. Nanosci.* **5**, 1 (2008).
- [Hepplestone] S. P. Hepplestone, G. P. Srivastava. Theory of interface scattering of phonons in superlattices. *Phys. Rev. B* **82**, 144303 (2010).
- [Herzfeld] K. F. Herzfeld, T. A. Litovitz. *Absorption and Dispersion of Ultrasonic Waves*. (Academic Press, 1959).
- [Hess] P. Hess. Laser diagnostics of mechanical and elastic properties of silicon and carbon films. *App. Surf. Sci.* **106**, 429 (1996).
- [Highland] B.C. Gundrum, Y. K.Koh, R. S. Averback, D.G. Cahill, V. C. Elarde, J. J. Coleman, D. A. Walko, and E. C. Landahl, *Phys. Rev. B* **76**, 075337 (2007).



- [Hinze] G. Hinze, D. D. Brace, S. D. Gottke, M. D. Fayer. *J. Chem. Phys.* **113**, 3723 (2000).
- [Hoffnagle] J. A. Hoffnagle, W. D. Hinsberg, M. Sanchez, F. A. Houle. Liquid immersion deep-ultraviolet interferometric lithography. *J. Vac. Sci. Technol. B* **17**, 3306 (1999).
- [Holland] M.G. Holland, *Phys. Rev.* **132**, 2461–2471 (1963).
- [Hooks] D. E. Hooks, K. J. Ramos, A. R. Martinez. Elastic shock profiles in oriented single crystals of cyclotrimethylene triamine (RDX) at 2.25 GPa. *J. Appl. Phys.* **100**, 024908 (2006).
- [Huang] Y. Y. Huang, C. H. Wang. *J. Chem. Phys.* **62**, 120 (1975).
- [Hyldgaard] P. Hyldgaard, G. D. Mahan. Phonon superlattice transport. *Phys. Rev. B* **56**, 10754 (1997).
- [Jena] A. Jena, H. E. Lessing. Theory of laser-induced amplitude and phase gratings including photoselection, orientational relaxation and population kinetics. *Opt. Quant. Electron.* **11**, 419 (1979).
- [Jenniskens] P. Jenniskens, D. F. Blake. Structural transitions in amorphous water ice and astrophysical implications. *Science* **265**, 753 (1994).
- [Johari] G. P. Johari, M. Goldstein. Viscous liquids and the glass transition. II. Secondary relaxations in glasses of rigid molecules. *J. Chem. Phys.* **53**, 2372 (1970).
- [Jakobsen] B. Jakobsen, K. Niss, N. B. Olsen. *J. Chem. Phys.* **123**, 234511 (2005).
- [Joshi] A. A. Joshi and A. Majumdar, “Transient ballistic and diffusive phonon heat transport in thin films”, *J. Appl. Phys.* **74**, 31 (1993).
- [Ju] Y. S. Ju and K. E. Goodson, *Appl. Phys. Lett.* **74**, 3005 (1999).
- [Kanatzidis] M. G. Kanatzidis. Nanostructured Thermoelectrics: The New Paradigm? *Chem. Mater.* **22**, 648 (2010).
- [Kawasaki] K. Kawasaki. Correlation-Function approach to the transport coefficients near the critical point. *Phys. Rev.* **150**, 291 (1966).
- [Keyes] T. Keyes, I. Oppenheim. Bilinear Contributions to Equilibrium Correlation Functions. *Phys. Rev. A* **7**, 1384 (1973).
- [Khoklov] D. Khoklov, editor. *Lead Chalcogenides: Physics and Applications*. (Taylor & Francis, New York, 2003).
- [Klieber] C. Klieber. PhD Thesis. (Massachusetts Institute of Technology, Cambridge, MA 2010).

- [Koh] Y. K. Koh and D. G. Cahill, "Frequency dependence of the thermal conductivity of semiconductor alloys", *Phys. Rev. B* **76**, 075207 (2007).
- [Kohlrausch] F. Kohlrausch. *Prog. Ann. Phys.* **119**, 352 (1863).
- [Käding] O. W. Käding, H. Skurk, A. A. Maznev, E. Matthias. Transient thermal gratings at surfaces for thermal characterization of bulk materials and thin films. *Appl. Phys. A* **61**, 253 (1995).
- [Landau] L. D. Landau, E. M. Lifshitz. *Theory of Elasticity*. (Pergamon Press, New York, 1970).
- [Lee] S. M. Lee, D. G. Cahill, R. Venkatasubramanian. Thermal conductivity of Si-Ge superlattices. *Appl. Phys. Lett.* **70**, 2957 (1997).
- [Leisure] R. G. Leisure, F. A. Willis. Resonant ultrasound spectroscopy. *J. Phys.: Condens. Matter* **9**, 6001 (1997).
- [Leutheusser] E. Leutheusser. Dynamical model of the liquid-glass transition. *Phys. Rev. A* **29**, 2765 (1984).
- [Li] C-M. Li, T. Sjödin, H-L. Dai, *Phys. Rev. B* **56**, 15252 (1997).
- [Lin] H. N. Lin, R. J. Stoner, H. J. Maris, J. Tauc. Phonon attenuation and velocity measurements in transparent materials by picosecond acoustic interferometry. *J. Appl. Phys.* **69**, 3816 (1991).
- [Linnros] J. Linnros, V. Grivickas, *Phys. Rev. B* **50**, 16943 (1994).
- [Liu01] W. L. Liu, T. Borca-Tasciuc, G. Chen, J. L. Liu, K. L. Wang. Anisotropic Thermal Conductivity of Ge Quantum-Dot and Symmetrically Strained Si/Ge Superlattices. *J. Nansci. Nanotech.* **1**, 39 (2001).
- [Liu] W. Liu, K. Etessam-Yazdani, R. Hussin, and M. Asheghi, "Modeling and Data for Thermal Conductivity of Ultrathin Single-Crystal SOI Layers at High Temperature", *IEEE Trans. Electron Dev.* **53**, 1868 (2006).
- [Lohfink] M. Lohfink, H. Silescu, in *AIP Conf. Proc. No. 256*. (American Institute of Physics, New York, 1992).
- [Lubchenko] V. Lubchenko, P. G. Wolynes. The origin of the boson peak and thermal conductivity plateau in low temperature glasses. *Proc. Nat. Acad. Sci.* **4**, 1515 (2003).
- [Lunkenheimer00] P. Lunkenheimer, U. Schneider, R. Brand, A. Loidl. *Contemp. Phys.* **41**, 15 (2000).
- [Lunkenheimer02] P. Lunkenheimer, A. Loidl. Dielectric spectroscopy of glass-forming materials:  $\alpha$ -relaxation and excess wing. *Chem. Phys.* **284**, 205 (2002).

- [Lunkenheimer08] P. Lunkenheimer, L. C. Pardo, M. Koehler, A. Loidl. *Phys. Rev. E* **77**, 031506 (2008).
- [Lyeo] H-K. Lyeo, D. G. Cahill. Thermal conductance of interfaces between highly dissimilar materials. *Phys. Rev. B* **73**, 144301 (2006).
- [Majumdar] ASME J. Heat Transfer **115**, 7 (1993).
- [Mandanici] A. Mandanici, X. Shi, G. B. McKenna, M. Cutroni. Slow dynamics of supercooled *m*-toluidine investigated by mechanical spectroscopy. *J. Chem. Phys.* **122**, 114501 (2005).
- [Marion] J. B. Marion, S. T. Thornton. *Classical Dynamics of Particles & Systems*. (Harcourt Brace Jovanovich, Orlando, 1988).
- [Mayer] P. Mayer, K. Miyasaki, D. Reichman. Cooperativity beyond caging: Generalized Mode-Coupling theory. *Phys. Rev. Lett.* **97**, 095702 (2006).
- [Maznev96] A. A. Maznev, K. A. Nelson, T. Yagi. Surface Phonon Spectroscopy with Frequency-Domain Impulsive Stimulated Light Scattering. *Sol. State Com.* **100**, 807 (1996).
- [Maznev98] A. A. Maznev, J. A. Rogers, K. A. Nelson. Optical heterodyne detection of laser-induced gratings. *Optics Letters*, **23**, 1319 (1998).
- [Maznev99] A. A. Maznev, A. Akthakul, K. A. Nelson. Surface acoustic modes in thin films on anisotropic substrates. *J. Appl. Phys.* **86**, 2818 (1999).
- [Maznev03] A.A. Maznev, A. Mazurenko, L. Zhuoyun, M. Gostein. Laser-based surface acoustic wave spectrometer for industrial applications. *Rev. Sci. Instrum.* **74**, 667 (2003).
- [Maznev11] A. A. Maznev, J. A. Johnson, K. A. Nelson. Non-equilibrium transient thermal grating decay in metal. *J. Appl. Phys.* **109**, 073517 (2011).
- [Maznev11b] A. A. Maznev, J. A. Johnson, K. A. Nelson. Onset of non-diffusive phonon transport in transient thermal grating decay. *In preparation*.
- [McCrone] W. C. McCrone. RDX (Cyclotrimethylene trinitramine). *Anal. Chem.* **2**, 81 (1941).
- [Mittal] A. Mittal and S. Mazumder, "Monte Carlo Study of Phonon Heat Conduction in Silicon Thin Films Including Contributions of Optical Phonons", ASME J. Heat Transfer **132**, 052402 (2010).
- [Mizuno] S. Mizuno, S. Tamura. Theory of acoustic-phonon transmission in finite-size superlattice systems. *Phys. Rev. B* **45**, 734 (1992).
- [Mizukami] M. Mizukami, K. Kobashi, M. Hanaya, M. Ogumi. *J. Chem. Phys. B* **103**, 4078 (1999).

- [Narumanchi] S.V.J. Narumanchi, J.Y. Murthy, and C.H. Amon, "Submicron Heat Transport Model in Silicon Accounting for Phonon Dispersion and Polarization", *ASME J. Heat Transfer* **126**, 947 (2004).
- [Nelson] K. A. Nelson, R. Casalegno, R. J. D. Miller, M. D. Fayer. Laser-induced excited state and ultrasonic wave gratings: Amplitude and phase grating contributions to diffraction. *J. Chem. Phys.* **77**, 1144 (1982).
- [Nelson82] K. A. Nelson, R. J. D. Miller, D. R. Lutz, M. D. Fayer. Optical generation of tunable ultrasonic waves. *J. Appl. Phys.* **53**, 1144, 1982.
- [Neubrand] A. Neubrand, P. Hess. Laser generation and detection of surface acoustic waves: Elastic properties of surface layers. *J. Appl. Phys.* **71**, 227 (1992).
- [Novikov] V. N. Novikov, A. P. Sokolov. Poisson's ratio and the fragility of glass-forming liquids. *Nature* **431**, 961 (2004).
- [Nye] J. F. Nye. *Physical Properties of Crystals*. (Oxford University Press, London, 1964).
- [Olsen] N. B. Olsen, T. Christensen, J. C. Dyre. *Phys. Rev. Lett.* **86**, 1271 (2001).
- [Othonos] A. Othonos. Probing ultrafast carrier and phonon dynamics in semiconductors. *J. Appl. Phys.* **83**, 1789 (1998).
- [Paddock] C. A. Paddock, G. L. Eesley. Transient thermorefectance from metals films. *Optics Lett.* **11**, 273 (1986).
- [Paolucci] D. M. Paolucci, K. A. Nelson. Impulsive stimulated thermal scattering study of the structural relaxation in supercooled glycerol. *J. Chem. Phys.* **112**, 6725 (2000).
- [Parker] W. J. Parker, R. J. Jenkins, C. P. Butler, G. L. Abbott. Flash Method for Determining Thermal Diffusivity, Heat Capacity, and Thermal Conductivity. *J. Appl. Phys.* **32**, 1679 (1961).
- [Patel] C. K. N. Patel, A. C. Tam. Pulsed optoacoustic spectroscopy of condensed matter. *Rev. Mod. Phys.* **53**, 517 (1981).
- [Pennington] D. M. Pennington, C. B. Harris. Dynamics of Photothermal Surface Expansion and Diffusivity Using Laser-Induced Holographic Gratings. *IEEE J. Quantum Electron.* **28**, 2523 (1992).
- [Pick03] R. M. Pick, T. Franosch, A. Latz, C. Dreyfus. Light scattering by longitudinal acoustic modes in molecular supercooled liquids I: phenomenological approach. *Eur. Phys. J. B* **31**, 217 (2003).
- [Pop] E. Pop, "Energy Dissipation and Transport in Nanoscale Devices", *Nano Res.* **3**, 147 (2010).

- [Poudel] B. Poudel, Q. Hao, Y. Ma, Y. Lan, A. Minnich, B. Yu, X. Yan, D. Wang, A. Muto, D. Vashaee, X. Chen, J. Liu, M. S. Dresselhaus, G. Chen, Z. Ren. High-Thermoelectric Performance of Nanostructured Bismuth Antimony Telluride Bulk Alloys. *Science*, **320**, 634 (2008).
- [Rogers93] J.A. Rogers, A.R. Duggal, K.A. Nelson. Non-contact real-time evaluation of polyimide thin film thermoelastic properties through impulsive stimulated thermal scattering, in *Amorphous Insulating Thin Films*, ed. by J. Kanicki, R.A.B. Davine, W. L. Warren, and M. Matsumura (Mater. Res. Soc. Symp. Proc. 284, 1993), pp. 547-553.
- [Rogers94] J. A. Rogers, Y. Yang, K. A. Nelson. Elastic modulus and in-plane thermal diffusivity measurements in thin polyimide films using symmetry selective real-time impulsive stimulated thermal scattering. *Appl. Phys. A* **58**, 523 (1994).
- [Rogers00] J.A. Rogers, A.A. Maznev, M.J. Banet, and K.A. Nelson, *Annu. Rev. Mater. Sci.* **30**, 117 (2000).
- [Rossiter] *Physical Methods of Chemistry, Volume 7, Determination of Elastic and Mechanical Properties*, 2<sup>nd</sup> ed. B. W. Rossiter, R. C. Baetzold eds. (Wiley, New York, 1991)
- [Rubio] J. E. F. Rubio, M. Taravillo, V. G. Baonza, J. Núñez, M Cáceres. Light-scattering study of vibrational relaxation in liquid xylenes. *J. Chem. Phys.* **124**, 014503 (2006).
- [Saleh] B. E. A. Saleh, M. C. Teich. *Fundamentals of Photonics*. (Wiley, Hoboken, NJ 2007).
- [Santen] L. Santen, W. Krauth. Absence of thermodynamic phase transition in a model glass former. *Nature* **405**, 550 (2000).
- [Schirmacher] W. Schirmacher, G. Diezemann, C. Ganter. Harmonic Vibrational Excitation in Disordered Solids and the “Boson Peak”. *Phys. Rev. Lett.* **81**, 136 (1998).
- [Schmidt08a] A. J. Schmidt, X. Chen, G. Chen. Pulse accumulation, radial heat conduction, and anisotropic thermal conductivity in pump-probe transient thermorefectance. *Rev. Sci. Instrum.* **79**, 114902 (2008).
- [Schmidt08b] A. J. Schmidt, M. Chiesa, D. H. Torchinsky, J. A. Johnson, K. A. Nelson, G. Chen. Thermal conductivity of nanoparticle suspensions in insulating media measured with transient optical grating and a hotwire. *J. App. Phys.* **103**, 083529 (2008).
- [Schmotz] M. Schmotz, P. Bookjans, E. Scheer, and P. Leiderer, “Optical temperature measurements on thin freestanding silicon membranes”, *Rev. Sci. Instrum.* **81**, 114903 (2010).
- [Schneider] U. Schneider, P. Lunkenheimer, R. Brand, A. Loidl. Dielectric and far-infrared spectroscopy of glycerol. *J. Non-cryst. Sol.* **235**, 173 (1998).

- [Schwarz] R. B. Schwarz, D. E. Hooks, J. J. Dick, J. I. Archuleta, A. R. Martinez. Resonant ultrasound spectroscopy of the elastic constants of cyclotrimethylene trinitramine. *J. Appl. Phys.* **98**, 056106 (2005).
- [Siegal] Y. Siegal, E. N. Glezer, L. Huang, E. Mazur. Laser-induced phase transitions in semiconductors. *Annu. Rev. Mater. Sci.* **25**, 223 (1995).
- [Siemens09] M. E. Siemens, Q. Li, R. Yang, M. M. Murnane, H. C. Kapteyn, R. Yang, E. H. Anderson, K. A. Nelson. High-frequency surface acoustic wave propagation in nanostructures characterized by coherent extreme ultraviolet beams. *Appl. Phys. Lett.* **94**, 093103 (2009).
- [Siemens10] M. Siemens, Q. Li, R. Yang, K. A. Nelson, E. Anderson, M. Murnane, and H. Kapteyn, *Nature Materials* **9**, 26 (2010).
- [Silence] S. Silence. PhD Thesis, (Massachusetts Institute of Technology, Cambridge, 1991).
- [Silence91] S. M. Silence, S. R. Goates, K. A. Nelson. *J. Non-Cryst. Solids* **131**, 137 (1991).
- [Silence92] S. M. Silence, A. R. Duggal, L. Dhar, K. A. Nelson. *J. Chem. Phys.* **96**, 5448 (1992).
- [Snyder] G. J. Snyder, E. S. Toberer. Complex thermoelectric materials. *Nat. Mat.* **7**, 105 (2008).
- [Sondheimer] E. H. Sondheimer, "The mean free path of electrons in metals", *Phil. Mag.* **1**, 1 (1952).
- [Stevens] R. J. Stevens, A. N. Smith, P. M. Norris. Measurement of Thermal Boundary Conductance of a Series of metal-Dielectric Interfaces by the Transient Thermoreflectance Technique. *J. Heat Trans.* **127**, 315 (2005).
- [Stevens10] L. L. Stevens, D. E. Hooks, A. Migliori. A comparative evaluation of elasticity in pentaerythritol tetranitrate using Brillouin scattering and resonant ultrasound spectroscopy. *J. Appl. Phys.* **108**, 053512 (2010).
- [Sun] B. Sun, J. M. Winey, N. Hemmi, Z. A. Dreger, K. A. Zimmerman, Y. M. Gupta, D. H. Torchinsky, K. A. Nelson. Second-order elastic constants of pentaerythritol tetranitrate and cyclomethylene trinitramine using impulsive stimulated thermal scattering. *J. Appl. Phys.* **104**, 073517 (2008).
- [Sverdrup] P. G. Sverdrup, S. Sinha, M. Asheghi, S. Uma, and K. E. Goodson, *Appl. Phys. Lett.* **78**, 3331 (2001).
- [Swartz] E. T. Swartz, R. O. Pohl. Thermal boundary resistance. *Rev. Mod. Phys.* **61**, 605 (1989).

- [Tamura] S. Tamura, D. C. Hurley, J. P. Wolfe. Acoustic-phonon propagation in superlattices. *Phys. Rev. B* **38**, 1427 (1988).
- [Tao] N. J. Tao, G. Li, H. Z. Cummins. *Phys. Rev. B* **45**, 686 (1992).
- [Taraskin] S. N. Taraskin, Y. L. Loh, G. Natarajan, S. R. Elliott. Origin of the Boson Peak in Systems with Lattice Disorder. *Phys. Rev. Lett.* **86**, 1255 (2001).
- [Terazima] M. Terazima. Optical Heterodyne Detected Transient Grating for the Separations of Phase and Amplitude Gratings and of Different Chemical Species. *J. Phys. Chem. A* **103**, 7401 (1999).
- [Tokmakoff] A. Tokmakoff, M. D. Fayer, W. Banholtzer. Thermal diffusivity measurement of natural and isotopically enriched diamond by picosecond infrared transient grating experiments. *App. Phys. A* **56**, 87 (1993).
- [TorchinskyT] D. H. Torchinsky. PhD Thesis, (Massachusetts Institute of Technology, Cambridge, MA 2008).
- [Torchinsky09] D. H. Torchinsky, J. A. Johnson, K. A. Nelson. A direct test of the correlation between elastic parameters and fragility of ten glass formers and their relationship to elastic models of the glass transition. *J. Chem. Phys.* **130**, 064502 (2009).
- [Turney] J. E. Turney, A. J. H. McGaughey, and C. H. Amon, "In-plane phonon transport in thin films", *J. Appl. Phys.* **107**, 024317 (2010).
- [Vacher] R. Vacher, L. Boyer. Brillouin Scattering: A Tool for the measurement of Elastic and Photoelastic Constants. *Phys. Rev. B* **6**, 639 (1972).
- [Walley] S. M. Walley, J. E. Field, M. W. Greenaway. Crystal sensitivities of energetic materials. *Mat. Sci. Tech.* **22**, 402 (2006).
- [Wang85] C. H. Wang, E. W. Fischer. Density fluctuations, dynamic light scattering, longitudinal compliance, and stress modulus in a viscoelastic medium. *J. Chem. Phys.* **82**, 632 (1985).
- [Wang] J. Wang, J. Hu, X. Sun, A. M. Agarwal, L. C. Kimerling, D. R. Lim, R. A. Synowicki. Structural, electrical, and optical properties of thermally evaporated nanocrystalline PbTe films. *J. Appl. Phys.* **104**, 053707 (2008).
- [Ward] A. Ward and D. A. Broido, *Phys. Rev. B* **81**, 085205 (2010).
- [Weber] W. Weber. Adiabatic bond charge model for the phonons in diamond, Si, Ge, and  $\alpha$ -Sn. *Phys. Rev. B*, **15**, 4789 (1977).
- [Whitley] V. H. Whitley. Optical Absorption Measurements of RDX. *Shock Compression of Condensed Matter*. 2005, p. 1357.
- [Williams] G. Williams, D. C. Watts. *Trans. Faraday Soc.* **66**, 80 (1970).



- [Wolfe] J.P. Wolfe, *Imaging Phonons* (Cambridge University Press, Cambridge, England, 1998).
- [Wright] O. B. Wright, V. E. Gusev. Acoustic generation in crystalline silicon with femtosecond optical pulses. *Appl. Phys. Lett.* **66**, 1190 (1995).
- [Wu] J. Wu, J. Cao. High-Order Mode-Coupling Theory for the Colloidal Glass Transition. *Phys. Rev. Lett.* **95**, 078301 (2005).
- [Yan] Y. Yan, E. B. Gamble, K. A. Nelson. Impulsive stimulated scattering: General importance in femtosecond laser pulse interactions with matter, and spectroscopic applications. *J. Chem. Phys.* **83**, 5391 (1985).
- [Yan87] Y. Yan, K. A. Nelson. Impulsive stimulated light scattering. II. Comparison to frequency-domain light-scattering spectroscopy. *J. Chem. Phys.* **87**, 6257 (1987).
- [Yan88] Y. Yan, L. Cheng, K. A. Nelson. The temperature-dependent distribution of relaxation times in glycerol: Time-domain light scattering study of acoustic and Mountain-mode behavior in the 20 MHz-3 GHz frequency range. *J. Chem. Phys.* **88**, 6477 (1988).
- [Yang95a] Y. Yang, K. A. Nelson, Impulsive Stimulated light scattering from glass-forming liquids. I. Generalized hydrodynamics approach. *J. Chem. Phys.* **103**, 7722 (1995).
- [Yang95b] Y. Yang, K. A. Nelson. Impulsive stimulated light scattered from glass-forming liquids. II. Salol relaxation dynamics, nonergodicity parameter, and testing of mode coupling theory. *J. Chem. Phys.* **103**, 7732 (1995).
- [Yang96] Y. Yang, K. A. Nelson. Impulsive stimulated thermal scattering study of a relaxation dynamics and the Debye-Waller factor anomaly in CKN. *J. Chem. Phys.* **104**, 5429 (1996).
- [Yoon]. J. Yoon, S. Jo, I. S. Chun, I. Jung, H. Kim, M. Meitl, E. Menard, X. Li, J. J. Coleman, U. Paik, J. A. Rogers. GaAs photovoltaics and optoelectronics using releasable multilayer epitaxial assemblies. *Nat. Lett.* **465**, 329 (2010).
- [Zeman] S. Zeman. High energy density materials. *Struct. Bond.* **125**, 195, 2007.
- [Zhang] X. Zhang, B. Li, C. Gao, *App. Phys. Lett.* **89**, 112120 (2006).
- [Ziman] J.M. Ziman, *Electrons and Phonons* (Clarendon Press, Oxford, 1960).
- [Zorn] R. Zorn, F. I. Mopsik, G. B. McKenna, L. Millner, D. Richter. *J. Chem. Phys.* **107**, 3645 (1997).
- [Zwanzig] R. Zwanzig. Time-Correlation Functions and Transport Coefficients in Statistical Mechanics. *Ann. Rev.* **16**, 67 (1965).

